UTRECHT STUDIES IN EARTH SCIENCES
No. 68

3-D numerical modeling of subduction evolution of the western Mediterranean region

Maria Chertova

Members of the dissertation committee:

Dr. Hana Čížková
Department of Geophysics, Charles University
Prague, Czech Republic

Prof. Taras Gerya
Institut für Geophysik, Eidgenössische Technische Hochschule
Zürich, Switzerland

Prof. Ulli Hansen
Institut für Geophysik, Westfälische Wilhelms-Universität Münster
Münster, Germany

Prof. Greg Houseman,
School of Earth and Environment, University of Leeds
Leeds, United Kingdom

Prof. Rinus Wortel
Department of Earth Sciences, Universiteit Utrecht
Utrecht, the Netherlands

The research of this thesis was carried out at:

Mantle Dynamics group
Faculty of Geosciences
Utrecht University
Budapestlaan 4
3584 CD Utrecht
The Netherlands

ISBN: 9789062663774
Printed by Wöhrmann print Service, Zutphen

3-D numerical modeling of subduction evolution of the western Mediterranean region

---

3-D numerieke modellering van subductie evolutie in het westelijke Middellandse Zeegebied
(met een samenvatting in het Nederlands)

Proefschrift

ter verkrijging van de graad van doctor aan de Universiteit Utrecht op gezag van de rector magnificus, prof.dr. G.J. van der Zwaan, ingevolge het besluit van het college voor promoties in het openbaar te verdedigen op woensdag 29 oktober 2014 des ochtends te 10.30 uur

Door

Maria Vladimirovna Chertova

geboren op 23 September 1986
te Novosibirsk, Rusland

Promotor: Prof. Dr. W.Spakman

Copromotor: Dr. A.P. van den Berg

Contents

Chapter 1

Introduction

This thesis focuses on the subduction evolution of the western Mediterranean region (Figure 1.1) since the middle Cenozoic. Although a very well studied region, its subduction evolution is still unresolved. In the past 15 years, the structure of the present-day mantle has played an increasingly important role in developing tectonic reconstructions of the region. A positive P-wave anomaly under the Alboran region was detected in early seismic investigations of deep structure of the region (e.g. Blanco and Spakman [1993], Piromallo and Morelli [1997], Bijwaard et al. [1998]). The question whether this anomaly has a continental or oceanic origin, or constitutes a combination of both lithospheric types was topic of strong debate and led to 3 different propositions (Section 1.3): convective lithosphere removal or continental delamination [Platt and Vissers, 1989; Seber et al., 1996; Calvert et al., 2000], oceanic subduction [Royden, 1993; Lonergan and White, 1997; Gutscher et al., 2002] and a combination of subduction of oceanic and continental lithosphere [e.g. Faccenna et al., 2004].

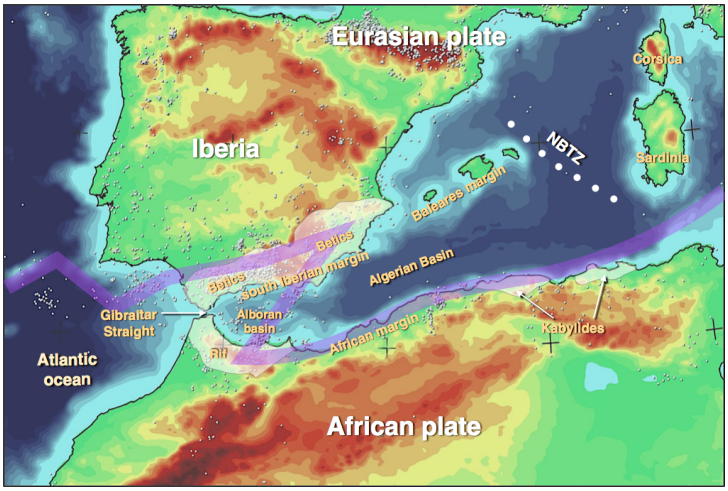

Figure 1.1. Map of the western Mediterranean region with the main geographic names and some tectonic features used in the paper. NBTZ- North Balearic Transform Fault zone. The transparent purple line depicts the diffuse plate boundary between the African and Eurasian plate in the region (after Gutscher 2012)

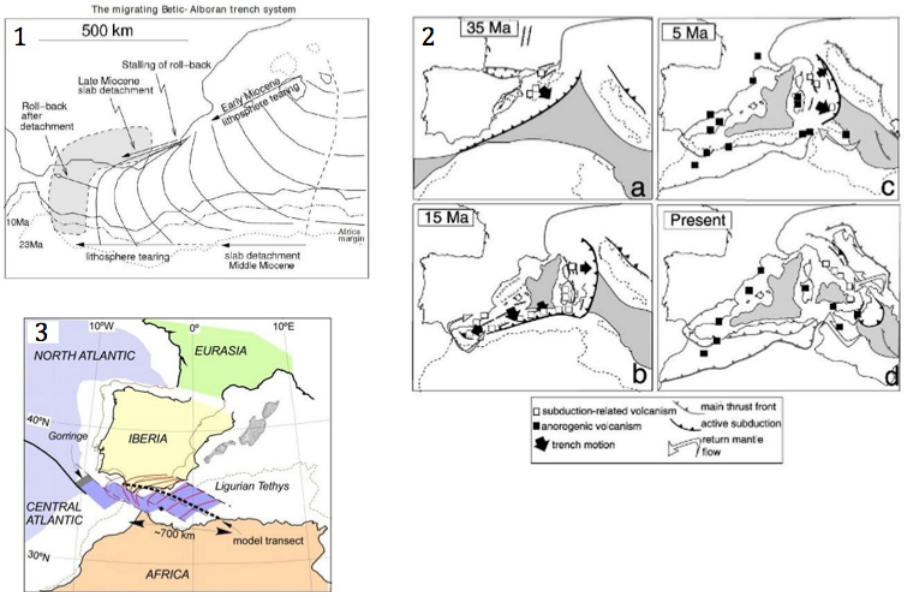

Figure 1.2 Three different reconstruction scenarios based on oceanic subduction or combination of oceanic subduction and continental delamination: 1) reconstruction of Spakman and Wortel (2004) showing trench evolution and highlighting the role of lithosphere tearing for subduction evolution. Grey shaded area gives the present day slab position at depth of 200km. The location of the Africa is shown in dashed/dotted lines. The dashed line on the right gives the proposed position of the fault, which divides the subducted slab into western (Alboran-Algerian basins) and eastern (Kabylides-Calabrian) parts. 2) Tectonic evolution of the western Mediterranean region of Faccenna et al. (2004). In Eurasia-fixed frame, the evolution is given in four stages from 35 Ma to present day. Deep basin domains are marked in grey. The location of the magmatic centers is marked with solid (anorogenic) and open (subduction-related) squares. 3) Geodynamic evolution of the western Mediterranean region of Verges and Fernandez, 2012. Dashed thick line shows the approximate trace of the central part of the slab segment. Brown solid and dashed lines show the present day position of the Iberia and Africa respectively.

The last two concepts on the origin of this anomaly formed the basis of a number of geodynamic reconstructions of the evolution of western Mediterranean region that compile a large amount of data from different

research fields. Although based on largely the same geological observations and on present-day observed mantle structure, these reconstructions propose completely different evolution scenarios [e.g. Gutscher et al. 2004; Faccenna et al., 2004; Spakman and Wortel, 2004; Handy et al., 2010; Verges and Fernandez, 2012; Figure 1.2].

In this thesis, starting from the proposed initial subduction configurations in the different tectonic scenarios, I develop dynamic models of the subduction evolution of the western Mediterranean region in 3-dimensional space and compare the end-stage of subduction with present-day mantle structure from seismic tomography models and with two key temporal constraints.

For 3-D thermo-mechanical modeling, I use a complex composite rheology for lithospheric plates and underlying mantle, which is depth and temperature dependent and includes a simple plasticity mechanism by means of limiting the viscosity or the maximum strength of materials. The numerical experiments test a wide range of settings of the rheology of continental lithosphere, margins, slab, and mantle. For such a wide range of experiments, both in terms of controlling parameters of numerical models and in research goals, extensive exploratory modeling is performed, which will be introduced in Chapters 3 and 4, on the dynamics of free subduction rollback, on initial and boundary conditions, rheological parameters, paleogeography, initial rheological structure and numerical settings, or parameters of solvers. This culminates into numerical modeling of the 3D subduction evolution of the western Mediterranean region that is successful in predicting present-day slab morphology and matches important temporal constraints on slab evolution (Chapters 4, 5).

1.1 Deep structure of the region.

Tomographic investigations of mantle structure of the Western Mediterranean started with Spakman [1986], followed in the 1990's by, e.g., Spakman et al. [1993], Blanco and Spakman [1993], Piromallo and Morelli [1997], Bijwaard et al. [1998], and later by Calvert et al. [2000], Piromallo and Morelli [2003], Spakman and Wortel [2004], and lately by Bezada et al. [2013] and Palomeras et al. [2014]. These studies detected a complex structure of the upper mantle beneath the Western Mediterranean, which consists of several positive anomalies of P-wave velocities. The following summarizes the main discovered mantle structures and their proposed origins:

- A positive anomaly located at the base of the upper mantle and the top of the lower mantle under the north Western Mediterranean, southern France and northern Italy, which is interpreted as remnants of the central Alpine-Tethys that subducted prior to collision in the Alps region [Spakman and Wortel, 2004],
-Positive anomaly patterns under the Apennines and Calabria, which are interpreted as the remnants of the west Alpine Tethys (Ligurian ocean) of which subduction started in the late Eocene – early Oligocene (e.g. Wortel and Spakman, [2000], Piromallo and Morelli [2003])
-A positive anomaly pattern under the Rif, Betic and west Alboran regions, of which the origin has been long debated but is now regarded to have a strong oceanic lithosphere signature (Section 1.2).
The area of our interest comprises the last positive anomaly of the Betic-Alboran region. Comparable first-order features of this anomaly are imaged in the models of Spakman and Wortel [2004] and Piromallo and Morelli [2003]. The mantle structure introduced in Piromallo and Morelli [2003] inspired the tectonic models of Faccenna et al. [2004] and Jolivet et al. [2009], which are significantly different from the scenario proposed by Spakman and Wortel [2004] that is more in line with the propositions of e.g. Lonergan and White [1997] and Rosenbaum et al. [2002] (Figure 1.2).
Recently, the mantle structure imaged in these earlier studies was confirmed and refined by Bezada et al. [2013] and Palomeras et al. [2014]. Figure 1.3a shows the 3D plot of the discovered cold anomaly under the Alboran Sea from Bezada et al. [2013] together with their cartoon interpretation (Figure 1.3b) and that of Spakman and Wortel [2004] (Figure 1.3c).

1.2 Origin of the Betic-Alboran anomaly

Up to now a number of competing hypotheses were introduced to explain the tectonic evolution of the Betic-Rif-Alboran region invoking different origins of the cold anomaly below this region. One hypothesis proposes an oceanic lithosphere origin resulting from subduction by slab rollback of the west Alpine Tethys (Ligurian Ocean) toward the north African margin and the present-day Betic-Rif region [e.g., Royden, 1993; Lonergan and White, 1997; Rosenbaum et al., 2002; Spakman and Wortel, 2004; Faccenna et al., 2004, Verges and Fernandez, 2012, van Hinsbergen et al., 2014].

Other hypotheses propose a continental lithosphere origin involving delamination or convective removal of lithospheric roots [Platt and Vissers, 1989; Seber et al. 1996; Houseman and Molnar 1997, Calvert et al. 2000]. This invokes an autochthonous origin for the lithosphere involved and may explain spatio-temporal patterns in geological observations (Platt and Vissers, 1989) or may explain the underlying cold anomaly as delaminated continental lithosphere (Seber et al. 1996; Calvert et al. 2000).
Recent seismological observations (e.g., Sallares et al., 2011; Bokelmann et al. 2011; Gutscher et al., 2012]), however, point strongly at an oceanic origin of the lithosphere of Gulf of Cadiz just west of the Gibraltar-Strait and point at a strong oceanic lithosphere nature of the slab-like upper mantle anomaly imaged under the Betic-Rif region [Gutscher et al. 2002]. This strongly supports the first hypothesis invoking oceanic subduction as the main mechanism for formation of the cold anomaly beneath Gibraltar that has been interpreted as a narrow east-dipping subduction zone just east of the Gibraltar Strait [Gutscher et al., 2002].

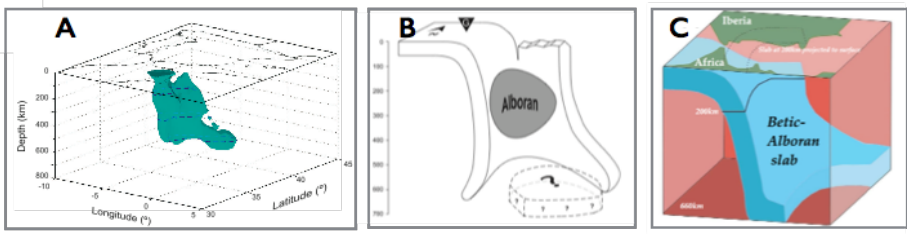

Figure 1.3. a) 3D view from the southeast of the +2% velocity anomaly isosurface. Dashed blue lines correspond to the +2% contour at depths of 195, 290 and 580km [from Bezada et al. 2013], b) the schematic representation of the discovered cold anomaly by Bezada et al. [2013], c) the cartoon interpretation of the cold anomaly under Gibraltar from Spakman and Wortel [2004].

1.3 Tectonic reconstructions of the region.

Tectonic reconstructions of the Western Mediterranean region of the last decade integrate the present-day mantle images of subduction remnants with surface evolution of the region describing its tectonic development from past to present. They can be divided into three distinctly different scenarios in

terms of the proposed direction of the rollback, the proposed initial subduction zone configuration, and slab length.

The first scenario (illustrated in Figure 1.2.1) was qualitatively depicted by Royden [1993] and Lonergan and White [1997], followed by more detailed analysis by, e.g., Rosenbaum et al. [2002], Gutscher et al. [2002], Spakman and Wortel [2004]. In its latest quantification, this scenario assumes a short initial trench of ~250-300 km southeast from Baleares measured from the North Balearic Transform fault (NBTZ; Figure 1.1) to the southwest and a short initial slab [van Hinsbergen et al., 2014]. The proposed direction of slab rollback is initially southward, growing radially outward until the slab reaches the African continent between 20-15 Ma. Then the trench rotates clockwise and the slab rolls back to the west associated with fast lithosphere tearing along the African margin. The last stage of rollback comprises westward rollback toward the Gibraltar Strait and northwest-directed slab rollback under the Betic region. Geological evidence of Iberia-Africa convergence dominating the tectonic evolution suggests that the slab has assumed a (nearly) stationary position since the late Tortonian (~8 Ma).

The second reconstruction scenario (Dercourt et al. [1986]; illustrated in Figure 1.2.2) portrays an overall south-to-east rollback system starting in the Oligocene. Faccenna et al. [2004] integrated this slab rollback scenario with imaged mantle structure of Piromallo and Morelli [2003] into a tectonic reconstruction of the Western Mediterranean. Recent reconstructions incorporating this rollback scenario are, e.g., Jolivet et al. [2009], Handy et al. [2010], and Carminati et al. [2012]. These reconstructions agree on an initial subduction zone stretching from Gibraltar to the Baleares margin at 35 Ma and suggest that the initial slab may have reached depths of 300-400 km depths [Faccenna et al., 2004]. The rollback process develops predominantly in a southward direction followed by rapid clockwise extrusion towards present-day Gibraltar after the middle Miocene time.

The third reconstruction scenario was proposed by Verges and Fernandez [2012] and is shown in Figure 1.2.3. The development of this region starts with an initial subduction zone at the African margin, instead of Iberian-Baleares margin. In this scenario the subduction process starts around 47-42 Ma with a trench lying along the African margin to the east of Gibraltar. The length of the trench is 400-500 km and slab depth is ~80-120 km measured from the lithosphere bottom; the initial direction of rollback is northwestward.

The direction of the slab rollback has been changed to westward during the late Oligocene - early Miocene with a slow westward retreat of the slab afterwards.

1.4 Numerical investigations of natural subduction evolution

In this thesis I investigate the subduction evolution of the western Mediterranean region using 3D thermo-mechanical numerical modeling. My focus is on modeling the evolution of a *natural* subduction process. This will be developed in this thesis and is more demanding than generic or process-oriented modeling of subduction because subduction evolution has to comply with observations of e.g. present-day mantle structure. One strategy developed to model natural subduction zones is by so-called adjoint modeling of mantle convection and subduction. This incorporates present-day mantle structure as imaged by seismic tomography to reconstruct past mantle flow and subduction (e.g. Liu and Gurnis [2008], Spasojevic et al. [2009]; Ismail-Zadeh et al. [2012]). In this thesis, I use a forward approach that starts from defining an initial condition of subduction in the geological past and aims to predict present-day mantle structure.

Most important for modeling of *natural* subduction when using a regional model, as in this thesis, is accounting for the effects of far-field forcing due to global plate tectonic dynamics and its interaction with the mantle. This implies performing 3-D subduction modeling with overriding and surrounding plates that has only recently seen developments in which far-field forces are accounted for by prescribed kinematic boundary conditions (e.g. Stegman et al. [2010], van Dinter et al. [2010], Butterworth et al. [2012], Yamato et al. [2009]). However, this concerns only generic settings using simple geometries involving trench-normal directions of applied boundary conditions, which is hardly applicable to natural subduction zones. In this thesis I will develop modeling of complex 3-D subduction of which the far-field forcing of the lithosphere plates involved is represented by absolute plate motion constraints.

One of the key geodynamic processes which has shaped the present-day Mediterranean region is lithosphere tearing [Wortel and Spakman 1992, 2000; Carminati et al. 1998; Spakman and Wortel 2004; Faccenna et al. 2004; Govers and Wortel, 2005; Wortel et al. 2009]. Detailed modeling of slab tearing using advanced visco-plastic rheology in 2-D and 3-D (e.g. Duretz et

al. [2014]) is still rather computationally intensive. A less demanding alternative is to simulate lithosphere tearing with a simplified approach of prescribed weakening of the material, for example, by implementing stress limiting on viscosity in terms of setting a maximum yield stress. Mason et al. [2010], van Hunen and Allen [2011] and Alisic et al. [2012] investigated this mechanism of material weakening in various applications and tested a range of values for maximum yield stress. In this thesis, I also implemented this approach to modeling lithosphere tearing.

1.5 Thesis outline

The main research goal of this thesis is investigating the subduction evolution of the western Mediterranean region during the past 35 My by employing 3-D thermo-mechanical modeling. This is basically unexplored territory and requires several major research questions to be addressed:

- What are suitable modeling domain parameters that allow for modeling dynamically self-consistent and internally driven subduction evolution?
- What are suitable initial conditions and what is the parameter range defining the composite rheology of different lithospheric types and of the mantle that allow for prediction of present-day slab morphology from 35 My of subduction evolution?
- To what extent can we simplify rheological and geometrical structure when modeling the evolution of *natural* subduction zone?
- Can 3-D slab evolution modeling of the western Mediterranean help in discriminating between the various tectonic reconstructions proposed in the past decade?
-Is it possible to simulate the different subduction scenarios as qualitatively portrayed in reconstructions?
- What is the influence of the absolute plate motions of the regional lithosphere involved in subduction on the evolution of subduction and on slab-mantle interaction?

To address these major questions, my research starts with exploratory modeling in 2-D of internally driven subduction subject to various boundary conditions. Next, building on the acquired expertise, the major part of my research addresses the 3-D numerical simulation of natural subduction in the region of interest, making links with tectonic reconstructions and with

absolute plate motions of continental lithosphere of northwest Africa and Iberia.

In Chapter 2 of this thesis I present an overview of the general physical equations, parameters settings, and numerical methods. This comprises the equations of conservation of mass, energy and momentum, and different choices for implementing rheology. The parameters involved and some complexities in tuning these parameters are discussed. In addition, computational attributes are briefly presented such as used solvers, finite element mesh, or the subdomain division for solving the governing equations by parallel computations. Lastly, in this chapter the initial and boundary conditions used in the various 2-D and 3-D experiments presented in this thesis, particularly for modeling of western Mediterranean subduction evolution, will be discussed briefly.

Chapter 3 is devoted to the investigation of basic modeling domain, initial temperature and rheological settings that lead to a self-consistent internally driven model of slab rollback in 2-D. In addition, the influence of boundary conditions on model flow development, particularly of free-slip and open boundary conditions imposed on the vertical side of the model, is investigated. These models demonstrate a great impact of the prescribed side boundary conditions on subduction evolution. We infer that open side boundaries allow for a significant reduction of domain size, which also reduces computational costs. The initial tests on the rheology, which I use for 3-D modeling, are also discussed in this chapter, which was published as Chertova et al., [2012].

Chapter 4 presents the development, numerical experiments, and results of 3-D thermo-mechanical modeling for simulating the evolution of subduction in the western Mediterranean region since ~35 Ma [Chertova et al., 2014]. A number of different geodynamic reconstructions were proposed for this region (Section 1.3) and in this chapter I attempt to model the subduction evolution as portrayed for each reconstruction scenarios. I demonstrate that only for one of reconstruction scenario, the one with an initial short subduction zone under Baleares margin, a 3-D slab evolution could be obtained that successfully predicts observed present-day upper mantle structure and fits several first-order temporal constraints. For the other two scenarios we could not find a combination of initial subduction geometries and rheological settings that led to a good prediction of present-day slab structure. For the most successful slab evolution model, I conducted various tests to investigate the sensitivity of slab

evolution to small variations in initial geometry and rheological parameters. For all models in Chapter 4, I imposed absolute plate motions of the northern African and Iberian continental regions, determined from Doubrovine et al. [2012].

In Chapter 5, I investigate the effect of using different absolute plate motion frames on subduction evolution of western Mediterranean region. I adopted the initial conditions and rheology settings from one of the successful slab models from Chapter 4 and tested the slab evolution under the kinematic constraints of different absolute plate motion frames. These absolute plate motion frames are: the global moving hotspot reference frame (GMHRF; Doubrovine et al., [2012]); a mantle-fixed African continent with Iberia moving in SE direction; a mantle-fixed Iberia continent with prescribed NW motion of Africa; and a frame using the GMHRF direction of Africa but taking two-times its speed. The first motion frame is data-based, while the other frames are invented. I demonstrate that each motion frame leads to a significantly different slab evolution as compared to the other frames even for small changes in plate velocity.

Lastly, in Chapter 6, I present a brief overview of main conclusions and an outlook on future research.

References

1. Alisic, L., M. Gurnis, G. Stadler, C. Burstedde, and O. Ghattas (2012), Multi-scale dynamics and rheology of mantle flow with plates, J. Geophys. Res., 117, B10402, doi:10.1029/2012JB009234.
2. Bezada M.J., and E.D. Humphreys (2012), Contrasting rupture processes during the April 11, 2010 deep-focus earthquake beneath Granada, Spain, Earth and Planetary Science Letters, 353–354, 38-46, doi: 10.1016/j.epsl.2012.08.001.
3. Bijwaard, H., W. Spakman, and E.R. Engdahl (1998), Closing the gap between regional and global travel time tomography. Journal of Geophysical Research, 103, 30, 055-78, doi: 0.1029/98JB02467.
4. Billi, A., C. Faccenna, O. Bellier, L. Minelli, G. Neri, C. Piromallo, D. Presti, D. Scrocca, and E. Serpelloni (2011), Recent tectonic reorganization of the Nubia-Eurasia convergent boundary heading for the closure of the western Mediterranean. Bulletin de la Société Géologique de France, 182, 279-303.
5. Blanco, M.J., W. Spakman (1993), The P-wave velocity structure of the

mantle below the Iberian Peninsula: evidence for subducted lithosphere below southern Spain. Tectonophysics 221, 13–34.

6. Bokelmann, G., E. Maufroy, L. Buontempo, J. Morales, G. Barruol (2011), Testing oceanic subduction and convective removal models for the Gibraltar arc: Seismological constraints from dispersion and anisotropy. Tectonophysics, 502, 28-37, doi: 10.1016/j.tecto.2010.08.004
7. Calvert, A., E. Sandvol, D, Seber, M. Barazangi S. Roecker, T. Mourabit, F. Vidal, G. Alguacil, and N. Jabour (2000), Geodynamic evolution of the lithosphere and upper mantle beneath the Alboran region of the western Mediterranean: constraints from travel time tomography, Journal of Geophysical Research, 105, B5, 10,871-10,898.
8. Carminati, E., M.J.R. Wortel, P.T. Meijer, R. Sabadini (1998), The two stage opening of the western-central Mediterranean basins: a forward modeling test to a new evolutionary model. Earth and Planetary Science Letters, 160, 667-679.
9. Carminati, E., M. Lustrino, and C. Doglioni (2012), Geodynamic evolution of the central and western Mediterranean: Tectonics vs. igneous petrology constraints, Tectonophysics, 579, 173-192, doi: 10.1016/j.tecto.2012.01.026
10. Chertova, M., T. Geenen, A.P. van den Berg, and W. Spakman (2012), Using open sidewalls for modelling self-consistent lithosphere subduction dynamics, Solid Earth Discuss. 4, 707-744, doi: 10.5194/se-3-313-2012.
11. Dercourt J., L.P. Zonenshain, L.-E. Ricou, V.G. Kazmin, X. LE Pichon, A.L. Knipper, C. Grandjacquet, I.M. Sbortshikov, J. Geyssant, C. Lepvrier, D.H. Pechersky, J. Boulin, J.-C. Sibuet, L.A. Savostin, 0. Sorokhtin, M. Westphal, M.L. Bazhenov, J.P. Lauer and B. Biju-Duval (1986), Geological evolution of the Tethys belt from the Atlantic to the Pamir since the Lias, Tectonophysics, 123, 241-315.
12. Doubrovine, P. V., B. Steinberger, and T.H. Torsvik (2012), Absolute plate motions in a reference frame defined by moving hotspots in the Pacific, Atlantic and Indian oceans. Journal of Geophysical Research, 117, B09101, doi: 10.1029/2011JB009072.
13. Duretz, T., T. Gerya, and W. Spakman (2014), Slab detachment in laterally varying subduction zones: 3D numerical modeling. Geophys. Res. Lett., accepted.
14. Faccenna C., C. Piromallo, A. Crespo-Blanc, L. Jolivet, and F. Rossetti (2004), Lateral slab deformation and the origin of the western Mediterranean

arcs. Tectonics;23:TC1012. doi:10.1029/2002TC001488.
15. Govers, R. and M.J.R. Wortel (2005), Lithosphere tearing at STEP faults: Response to edges of subduction zones, Earth and Planetary Science Letters, 236 (1-2), pp. 505-523.
16. Gutscher M.A., J. Malod, J.P. Rehault, I. Contrucci, F. Klingelhoefer, L. Mendes-Victor, and W. Spakman (2002), Evidence for active subduction beneath Gibraltar. Geology;30:1071-1074.
17. Handy, M.R., S.M. Schmid, R. Bousquet, E. Kissling, and D. Bernoulli (2010), Reconciling plate-tectonic reconstructions of Alpine Tethys with the geological–geophysical record of spreading and subduction in the Alps, Earth-Science Reviews, 102, 3–4, 121-158, doi: 10.1016/j.earscirev.2010.06.002.
18. Houseman, G.A., Molnar, P., 1997. Gravitational (Rayleigh–Taylor) instability of a layer with nonlinear viscosity and convective thinning of continental lithosphere. Geophys. J. Int. 128, 125–150.
19. Jolivet, L., C. Faccenna, and C. Piromallo (2009), From mantle to crust: Stretching the Mediterranean, Earth and Planetary Science Letters, 285,1–2, Pages 198-209, doi: 10.1016/j.epsl.2009.06.017.
20. Lonergan, L., and N. White (1997), Origin of the Betic-Rif mountain belt, Tectonics, 16(3), 504–522, doi:10.1029/96TC03937.
21. Palomeras, I., S. Thurner, A. Levander, K. Liu, A. Villasenor, R. Carbonell, and M. Harnafi (2014), Finite-frequency Rayleigh wave tomography of the western Mediterranean: Mapping its lithospheric structure, Geochem. Geophys. Geosyst., 15, doi:10.1002/2013GC004861.
22. Piromallo, C., A. Morelli (1997), Imaging the Mediterranean upper mantle by P-wave travel time tomography. Ann. Geofis. 40, 963–979.
23. Piromallo, C., and A. Morelli (2003), *P* wave tomography of the mantle under the Alpine-Mediterranean area, J. Geophys. Res., 108, 2065, doi: 10.1029/2002JB001757, B2.
24. Platt, J., Vissers, R., 1989. Extensional collapse of thickened continental lithosphere: a working hypothesis for the Alboran Sea and Gibraltar arc. Geology 17, 540-543.
25. Rosenbaum, G., G.S. Lister, and C. Duboz (2002), Reconstruction of the tectonic evolution of the western Mediterranean since the Oligocene. Journal of the Virtual Explorer, 8, 107–130.
26. Royden, L.H. (1993), Evolution of retreating subduction boundaries formed during continental collision. Tectonics 12, doi:10.1029/92TC02641.

27. Seber, D., M. Barazangi, A. Ibenbrahim, A., Demnati (1996), Geophysical evidence for lithospheric delamination beneath the Alboran Sea and Rif – Betic mountains. Nature, 379.
28. Spakman, W. (1986), Subduction beneath Eurasia in connection with the Mesozoic Tethys. Geologic en Mijnbouw 65: 145-153
29. Spakman W., S. Van der Lee, and R.D. van der Hilst (1993), Travel-time tomography of the European-Mediterranean mantle down to 1400km. Phys. Earth. Planet. Inter, 79:3-7
30. Spakman W., and M.J.R. Wortel (2004), A tomographic view on western Mediterranean geodynamics. In: Ziegler P., editor. The TRANSMED Atlas-The Mediterranean Region From Crust to Mantle. Berlin: Springer, pp. 31-52.
31. Stegman, D.R., W.P. Schellart, and J. Freeman (2010), Competing influences of plate width and far-field boundary conditions on trench migration and morphology of subducted slabs in the upper mantle, Tectonophysics, 483, 1–2, 46-57, doi:10.1016/j.tecto.2009.08.026.
32. van Dinter, Y., G. Morra, F. Funiciello, and C. Faccenna (2010), Role of overriding plate in the subduction process: Insights from numerical models. Tectonophysics, 484, 74-86, doi: 10.1016/j.tecto.2009.08.038
33. van Hinsbergen, D.J.J., R.L.M. Vissers, and W. Spakman (2014), Origin and consequences of western Mediterranean subduction, rollback, and slab segmentation, *Tectonics*
34. van Hunen, J., and M.B. Allen (2011), Continental collision and slab break-off: a comparison of 3-D numerical models with observations. Earth and Planetary Science Letters 302(1-2), 27-37, doi: 10.1016/j.epsl.2010.11.035
35. Vergés, J., and M. Fernàndez (2012), Tethys–Atlantic interaction along the Iberia–Africa plate boundary: The Betic–Rif orogenic system, Tectonophysics, 579, 144-172, doi:10.1016/j.tecto.2012.08.032.
36. Wortel, R., R. Govers, and W. Spakman (2009), Continental collision and the STEP-wise evolution of convergent plate boundaries: From structure to dynamics, *in:* S. Lallemand and F. Funiciello (Eds.), Subduction Zone Geodynamics, pp. 47-59, Springer Berlin Heidelberg, doi: 10.1007/978-3-540-87974-9.
37. Wortel, M.J.R. and W. Spakman (1992), Structure and dynamics of subducted lithosphere in the Mediterranean region. *Proc. Kon. Ned. Akad. v. Wetensch.*,95, 325-347.
38. Wortel, M.J.R. and W. Spakman (2000), Subduction and slab detachment in

the Mediterranean-Carpathian region. Science, 290; doi:10.1126/science.290.5498.1910

39. Yamato, P., L. Husson, J. Braun, C. Loiselet, and C. Thieulot (2009), Influence of surrounding plates on 3D subduction dynamics. Geophysical research letters, 36, L07303, doi:10.1029/2008GL036942.

Chapter 2

Model description

2.1 Introduction

This thesis deals with a quantitative study of geodynamic processes involving lithospheric subduction. The method of investigation is numerical modeling of the main physical processes modeled as convective-diffuse heat transport in 2D and 3D media. In the following sections the governing model equations are presented for thermal convection in a viscous medium allowing for compositional heterogeneity implemented through Lagrangian particles and subject to solid-state phase transitions around depths of 410 km and 660 km in the mantle. The discretization of these coupled equations with the finite element method and the numerical solution of the resulting discrete equations is briefly described. Finally an overview is presented of various model setups, and definition of initial and boundary conditions used for generic 2D slab evolution modeling (Chapter 3) and for 3D modeling applied to western Mediterranean subduction evolution since ~35 Ma (Chapters 4 and 5).

2.2 Governing equations

To obtain a velocity field and temperature distribution in our model three coupled equations are solved, namely: mass conservation, momentum, and energy in the extended Boussinesq approximation [Christensen and Yuen 1985]. The general dimensional form of these equations is given in the following (symbols are defined in Table 2.1):

$$\partial_j v_j = 0 \,, \tag{2.1a}$$

$$\partial_j \tau_{ij} - \Delta\rho g_i = \partial_i \Delta P, \tag{2.1b}$$

$$\rho C_p \frac{DT}{Dt} = \partial_j k \partial_j T + T\alpha \frac{dP}{dt} + \tau_{ij}\partial_j v_i + \sum_k \rho_0 T \Delta S_k \frac{d\Gamma_k}{dt}, \tag{2.1c}$$

where $\Delta\rho = \rho - \rho_0$, and $\partial_i \Delta P = \partial_i P - \rho_0 g_i$. Temperature and phase dependence of density is described by the following equation of state:

$$\rho(T, \Gamma_k) = \rho_0 (1 + \sum_k \frac{\Delta\rho_k}{\rho_0}\Gamma_k - \alpha(T - T_s)), \tag{2.2}$$

where $\Delta\rho_k = \rho_k - \rho_0$.

Non-dimensional equations are obtained using the following relationships [e.g. Schubert et al. 2001]:

$\vec{x} = \vec{x}'h,\ t = \frac{t\prime h^2}{\kappa},\ \vec{v} = \vec{v}'\frac{\kappa}{h},\ \eta = \eta'\eta_{0,}$

$\tau = \tau'\frac{\eta_0\kappa}{h^2},\ T - T_s = \Delta TT',\ \Delta P = \Delta P'\frac{\eta_0\kappa}{h^2}$ (2.3)

The non-dimensional equations are written as:

mass conservation of an incompressible viscous fluid:

$\partial_j v_j = 0$, (2.4a)

the Stokes equation describing conservation of momentum:

$-\partial_i \Delta P + \partial_j \tau_{ij} = (RaT - \sum_k Rb_k\,\Gamma_k)\hat{g}_i,$ (2.4b)

and the heat transport equation assuming uniform conductivity and excluding radiogenic heating:

$\frac{\partial T}{\partial t} + v_j\partial_j T - \partial_j\partial_j T - Di(T + T_0)\hat{g}_i v_i -$

$\sum_k \gamma_k \frac{Rb_k}{Ra} Di(T + T_0)\frac{d\Gamma_k}{dt} = \frac{Di}{Ra}\Phi.$ (2.4c)

Our models include two mineral phase transitions near the depths of 410 km and 660 km in the unperturbed mantle. The exact position of the phase transitions depends on ambient mantle temperature in the region. The 410 km phase change contributes to the negative buoyancy force on cold material and increases slab pull. The phase change at 660 km has a positive buoyancy effect on cold material resisting slab penetration to the deeper mantle [Karato et al. 2001, Billen et al. 2010] associated with a local depression of the phase boundary. Values for the Clapeyron slopes are given in Table 2.1. Phase transitions are parameterized in the model with the phase parameter function:

$\Gamma_k = \frac{1}{2}(1 + \sin\left(\frac{\pi z_{diff}}{w}\right))$, (2.5)

where $z_{diff} = z - z_{tr} - \gamma k \cdot (T - T_{tr})$, in which w is the half-width of kth transition zone, z_{tr} and T_{tr} are the reference depth and temperature of the phase transition, respectively, γ_k is the Clapeyron slope, T is the temperature.

2.3 Rheology

We use a composite rheology both for mantle and lithosphere and we allow that the parameters for the different viscosity components are different for these parts. We do not account for the elasticity in our modeling and the composite rheology includes contributions from diffusion and dislocation creep and includes a viscosity limiting mechanism:

$\frac{1}{\eta_{\text{eff}}} = \frac{1}{\eta_{diff}} + \frac{1}{\eta_{disl}} + \frac{1}{\eta_l}$ (2.6a)

To determine the viscosity due to diffusion and dislocation creep the following expressions are used [Turcotte and Schubert, 2002]:

$$\eta_{diff} = \mu A_{diff}^{-1} \left(\frac{b}{d}\right)^{-m} \exp\left(\frac{E_{diff}+PV_{diff}}{RT}\right), \quad (2.6b)$$

$$\eta_{disl} = \mu A_{disl}^{-\frac{1}{n}} \dot{\varepsilon}^{\frac{1-n}{n}} \exp\left(\frac{E_{disl}+PV_{disl}}{nRT}\right), \quad (2.6c)$$

where $\dot{\varepsilon}$ is the second invariant of the strain-rate tensor, P is the lithostatic pressure and T –temperature. Other parameters and their values used for components of the composite rheology are listed in Table 2.2.

The representation of the first part of the equations, the pre-exponential component, varies between applications to subduction modeling [van Hunen and Allen, 2011; Billen and Hirth, 2007]. However, this pre-exponential factor basically serves as a scaling factor and how the prefactor is represented is not crucial for the results of numerical modeling. The depth and temperature dependent parts of the dislocation and diffusion creep are similar in most investigations. Exceptions are the cases when authors do not include the depth/pressure dependent component, like in van Hunen and Allen [2011], where different values for E_{diff}, E_{disl} are used representing the activation energy for the lithosphere and upper mantle. Parameters $E_{diff}, E_{disl}, V_{diff}, V_{disl}$ were presented by Karato and Jung [2003], Karato and Wu [1993], Hirth and Kohlstedt [2003], Karato and Ogawa [1982]. These parameters are varied within a wide range and in this thesis a range of these values for activation energy and volume was tested for both diffusion and dislocation components. We found that, for our purposes, values for these material properties should be within the range for the wet olivine rheology [Karato et al., 2001; Hirth and Kohlstedt, 2003] (Chapters 3, 4).

The third component of the composite rheology is represented by the limiting viscosity η_l. Different representations of this component were used in our experiments for two- and three-dimensional geometry. In our initial experiments in 2D (Chapter 3) we prescribe this limiting viscosity to have a constant value η_{max}. This value is normally 3-4 orders of magnitude higher than the reference viscosity value η_0 defined in Table 2.1.

However, for the subsequent 3D experiments (Chapters 4 and 5) this representation was improved by introducing a stress limiting mechanism instead of the viscosity-limiter. Rock under high stresses demonstrates plastic behavior, which leads to decreasing of the lithospheric viscosity in zones of high stresses. For the fast rollback and lithosphere tearing in narrow 3D

subduction zone settings the weakening in the bending zone due to plastic deformation is a major factor controlling the evolution of the subduction process [Burov, 2011; Alisic et al., 2012].

Symbol	Meaning	Value	Dim.
α	Thermal expansivity coefficient	3×10^{-5}	K^{-1}
$\boldsymbol{g_0}$	Gravitational acceleration	9.8	$m\ s^{-2}$
$\boldsymbol{c_p}$	Specific heat	1250	$J\ kg^{-1}K^{-1}$
$\boldsymbol{k}$	Thermal conductivity	4.27	$W\ m^{-1}K^{-1}$
κ	Thermal diffusivity, $k/\rho c_p$	10^{-6}	$m^2\ s^{-1}$
$\boldsymbol{\rho_0}$	Reference density	3413	$Kg\ m^{-3}$
h	Height of the domain	1000	km
$\boldsymbol{Ra}$	Thermal Rayleigh number, $\rho_0 g\alpha\Delta T h^3/\eta_0\kappa$	1.7×10^6	-
$\boldsymbol{Rb_k}$	Phase Rayleigh number, $\Delta\rho g h^3/\eta_0\kappa$	-	-
$\boldsymbol{\hat{g}_i}$	Unit vector in the direction of gravity	-	-
$\boldsymbol{\eta_0}$	Reference viscosity	10^{21}	Pa s
γ_1	Clapeyron slope (410 km)	4.1	$MPaK^{-1}$
$\Delta\boldsymbol{\rho_1}$	Density contrast (410 km)	273	$Kg\ m^{-3}$
γ_2	Clapeyron slope (660 km)	-1.9	$MPaK^{-1}$
$\Delta\boldsymbol{\rho_2}$	Density contrast (660 km)	342	$Kg\ m^{-3}$
w	Half-width of phase transitions	50	km
$\boldsymbol{\Gamma_k}$	Phase function for k-*th* mantle phase transitions	-	-
$\boldsymbol{v_j}$	i-th component of the velocity	-	-
$\boldsymbol{P}$	Hydrostatic pressure	-	-
$\boldsymbol{\partial_i}\Delta P$	Dynamic pressure gradient, $\partial_i P - \rho_0 g_i$	-	-
$\boldsymbol{\tau_{ij}}$	ij-th component of the deviatoric stress tensor, $\eta\dot{\varepsilon}_{ij}$	-	-
$\boldsymbol{T}$	Temperature	-	-
$\boldsymbol{T_s}$	Surface temperature	273	K
$\boldsymbol{T_0}$	Normalized surface temperature, $T_s/\Delta T$	0.1605	-
$\boldsymbol{Di}$	Dissipation number, $\alpha g h/c_p$	0.24	-
$\boldsymbol{\Phi}$	Viscous dissipation, $\eta\dot{\varepsilon}^2$	-	$W\ m^{-3}$
R	Gas constant	8.314	$J\ mol^{-1}K^{-1}$
$\boldsymbol{\dot{\varepsilon}_{ij}}$	Strainrate tensor, $\partial_j v_i + \partial_i v_j$	-	s^{-1}
$\boldsymbol{\dot{\varepsilon}}$	Second invariant of the strain rate $(1/2\Sigma_{ij}\dot{\varepsilon}_{ij}{}^2)^{1/2}$	-	s^{-1}

Table 2.1. Definition of symbols.

In our 3D models this weakening of the lithospheric material due to plastic rock behavior was implemented in terms of a yield stress, τ_y. When the stress exceeds the prescribed value of τ_y the material weakens and deformation develops faster. A corresponding viscosity η_y replaces the limiting viscosity η_l in equation 2.1a and is defined as:

$$\eta_y = \frac{\tau_y}{2\dot{\varepsilon}}, \quad (2.7a)$$

[Schott and Schmeling, 1998; Enns et al., 2005; OzBench et al., 2008; Mason et al., 2010; Magni et al., 2012], where

$$\tau_y = \min(\tau_0 + \gamma P, \tau_{max}); \quad (2.7b)$$

In (2.2.b) τ_0 is the yield stress value at the top surface, τ_{max} is the maximum yield stress value and γ is a yield stress gradient, which is increasing with depth. Parameter values are given in Table 2.2. The first component for τ_y defines the depth dependent strength of the material. Due to this component the top part of the subducted lithosphere is typically weak in rheological models, for example, to implement a weak top-boundary decoupling layer, as in Schellart and Moresi [2013], or OzBench et al. [2008]. With depth the strength of the material increases until it reaches τ_{max}. This parameter controls the strength of the deeper part of the lithospheric material in the bending zone, which affects the speed of the rollback process in subduction modeling. In stagnating regions, characterized by low values of the strain rate $\dot{\varepsilon}$, we do not allow the viscosity to become larger than a given limit, which is varied between $10^{24} - 10^{25}$ Pa s.

The strength of the material defined in terms of τ_{max} varies between different authors [Alisic et al., 2012; van Hunen and Allen, 2011; OzBench et al., 2008; Cizkova et al., 2007; Billen et al., 2010, Burov, 2011] in the range of 50-1200 MPa. The values for γ also vary between 0.05 and 0.9. When using γ = 0.05, material at depth 100 km will still be very weak and its strength will be lower than 100 MPa, while using a value of 0.9, material at depths of 30-50 km will instead be quite strong (400-500 MPa). For the modeling of the subduction evolution of western Mediterranean we vary these values from 0.055 to 0.6. The large range in values used for the strength of the lithosphere also relates to its use in either time-dependent or instantaneous dynamics modeling. We refer to Alisic et al. (2012) for the discussion on difference between these two approaches in terms of implemented maximum yield stress value.

In our 3D subduction models the rheology discussed above is applied to different lithologies with contrasting properties specified in Table 2.2. This allowed the following regions with contrasting rheological parameter values to be defined (Figure 2.2):

1) material corresponding to continental lithosphere domains with a depth extension of approximately 150 km;

2) material corresponding to continental margins with an initial width of 70-110 km and thickness of 120-150 km, bordering continental regions;

3) oceanic material, located between continental regions;

4) weak material representing weak crust, which is placed on top of oceanic lithosphere and between slab and overriding plate, which is oceanic for the 2D modeling of Chapter 3 and continental for 3D experiments of Chapters 4 and 5;

5) material corresponding to a decoupling zone simulating a transform fault.

We define material types in the rheological model by means of tracer particles, which are advected by the flow field. The material type corresponds to the value of the single degree of freedom carried by each particle. These tracer values are projected on the nodal points of a structured spatial grid using a particle-in-cell (PIC) method [Hockney and Eastwood, 1988]. In the model calculations the local material type is then determined by interpolation of the structured grid values.

In our 3D experiments we distribute tracers randomly over the whole modeling domain except for some models where we have used uniform rheology parameters for the sub-lithospheric mantle. In these models the initial tracer locations are restricted to a depth < 200 km. The total number of tracers varied between 20 and 40 million. For all our 2D experiments tracers initially were distributed over the top 200 km. Initial number of tracers for these experiments was 800000 with allowed tracers inflow and outflow. In the computations for the tracer advection we apply a fourth-order Runge-Kutta scheme [Gerya, 2010].

A_{diff}	Diffusion prefactor	5.3-9×$\mathbf{10^{15}}$	s^{-1}
A_{disl}	Dislocation prefactor	2-6×10^{18}	s^{-1}
b	Burgers vector	5×10^{-10}	m
d	Grain size	10^{-6}	m
m	Grain size exponent	2.5	-
n	Stress exponent dislocation creep	3	-
μ	Shear modulus	80×1e9	Pa
V_{diff}	Activation volume for the diffusion creep	2-6	cm^3mol^{-1}
V_{disl}	Activation volume for the dislocation creep	6-16	cm^3mol^{-1}
E_{diff}	Activation energy for the diffusion creep	240-320	KJ mol^{-1}
E_{disl}	Activation energy for the dislocation creep	420-490	KJ mol^{-1}
η_{LM}	Viscosity of the lower mantle	$0.1-2\times10^{22}$	Pa s
η_{sed}	Viscosity of the weak sedimentary layer	$1-9\times10^{19}$	Pa s
γ	Yield stress gradient	0.055-0.6	-
η_{max}	Maximum viscosity	10^{24}-10^{25}	Pa s
τ_0	Yield stress at the earth surface	40	MPa
$\tau_{\max}$	Reference value for maximum yield stress	800	MPa
$\tau_{\max\_oc}$	Maximum yield stress, oceanic lithosphere	300-1200	MPa
$\tau_{\max\_c}$	Maximum yield stress, continental lithosphere	200-800	MPa
$\tau_{\max\_Af}$	Maximum yield stress, continental margin	50-800	MPa
$\tau_{\max\_f}$	Maximum yield stress, decoupling zone simulating transform fault	200	MPa

Table 2.2. Rheological parameters.

2.4 Numerical methods

To solve the governing equations 1.4a-1.4c we use the finite element package SEPRAN [Segal and Praagman, 2005]. This package is designed for a broad range of applications for various classes of problems [van den Berg et al.

2014]. Several applications built with the SEPRAN package were tested for a range of mantle convection models [van Summeren, 2008; de Vries et al., 2010; Jacobs and van den Berg, 2011] and for modeling of the subduction process [van Hunen, 2001; Cizkova et al., 2012]. For the present work an extended SEPRAN code was developed and applied in 2D and 3D domains.

In our 2D experiments we use quadratic triangular Taylor-Hood elements for the velocity field and pressure in the Stokes equation 1.4a. The number of nodal points varies between 40000 and 60000. The spatial resolution varies from 1-2 km near the initial subduction fault zone and near the top surface to 25 km at depth of 1000 km.

For 3D experiments we use linear tetrahedral Taylor-Hood elements with four nodal points per element. The resolution in our 3D models is also spatially variable and is varied from 5-7 km near the initial subduction zone to 12 km on the topsides and 25 km on the bottom boundary. The solution vector contains three velocity components and one pressure unknown in each nodal point: v_1, v_2, v_3, P.

The total number of elements in our models varies between 4 and 7 million. The number of nodal points varies between 0.7 and 1.1 million and total number of degrees of freedom is around 3-4 million. For the modeling of subduction evolution in 3D we adapt the code for parallel computations using a domain decomposition approach. To this end, the model domain was subdivided into 32 to 96 subdomains. The number of parallel processes used corresponds to the number of subdomains. An example of a 3-D model domain and its domain subdivision with superimposed a schematic map of the study region, the western Mediterranean, is shown in Figure 2.1. This figure also illustrates the difference between element sizes on the top and bottom boundaries.

We solve three coupled finite element equations corresponding to eq. 2.1a-c, which are given in matrix form with following relations [Cuvelier et al., 1988]:

$\mathbf{L}\mathrm{U} = 0$ - mass conservation, (2.8a)

$\mathbf{D}\mathrm{U} - \mathbf{L}^T\mathrm{P} = \mathbf{F}$ - momentum conservation, (2.8b)

$\mathbf{M}\dot{\mathrm{T}} + \boldsymbol{S}\mathrm{T} = \boldsymbol{R}$ - energy conservation, (2.8c)

where U, P, T are the vectors of unknown nodal point values of flow velocity, dynamic pressure and temperature respectively; the $\mathbf{L}^T\mathrm{P}$ term is derived from the $\partial_i \Delta P$ term in eq. 2.1b, **D** is the stress related stiffness matrix**,** **M** is the

mass matrix, **S** is the stiffness matrix and **F** and **R** are right-hand side vectors. The coupled equations 6.1a,b were solved with an iterative GMRES solver with ILU preconditioner. The number of iterations varies in a wide range, mainly from 1600 to 3500; the average number of iterations per time step for different model runs varies in the range of 2000-2400. As stopping criterion for the iterative solver we use a relative accuracy $\epsilon = 10^{-6}$. We use the Euler-implicit time integration scheme for the energy conservation equation. The time step is non-uniform and determined each time-iteration using the CFL (Courant-Frederichs-Levy) criterion. Average duration of one time–step is 3-7 minutes and the total computational time varied between 7 and 14 days per model run. The total number of time steps varied between 1500-2200.

2.5 Boundary conditions and domain geometry

We perform experiments in Cartesian geometry both in 2 and 3 dimensions. The first set of experiments in a 2D domain, which will be presented in Chapter 3, was performed to investigate the impact of domain size and boundary conditions on flow dynamics. In all our experiments the depth of the domain is 1000 km. The width for 2D experiments was varied from 3000 to 6000 km and for 3D experiments (Chapters 4 and 5) domain horizontal dimensions were varied from 1300/1650 to 1650/2200 km.

Different boundary conditions were tested and implemented in our model: no-slip, free slip and open boundaries respectively formulated as:

$$\mathbf{v}=\mathbf{0}, \tag{2.9}$$

$$v_n = 0,\ \tau_t = 0, \tag{2.10}$$

$$\sigma_{nn} = -P,\ v_t = 0, \tag{2.11}$$

where "t" and "n" denote the tangential and normal directions to a particular model boundary. The first and second types of boundary conditions (eq. 2.9, 2.10) were tested for the bottom boundary. For most of our experiments we use no-slip boundary conditions for the bottom boundary, as completely open side boundaries in a combination with free slip for the top and bottom result in a model with homogeneous natural boundary conditions in horizontal direction on the complete boundary and this problem does not have a unique solution.

Free slip boundary conditions are implemented for the top boundary in all 2D and 3D models. To allow lithosphere decoupling from the top surface and the overriding plate, a weak top layer simulating the crust is implemented in our

models [Chertova et al., 2012; van Hunen and Allen, 2011] (Chapters 4 and 5; Section 2.2, 2.5, 2.6, Table 2).

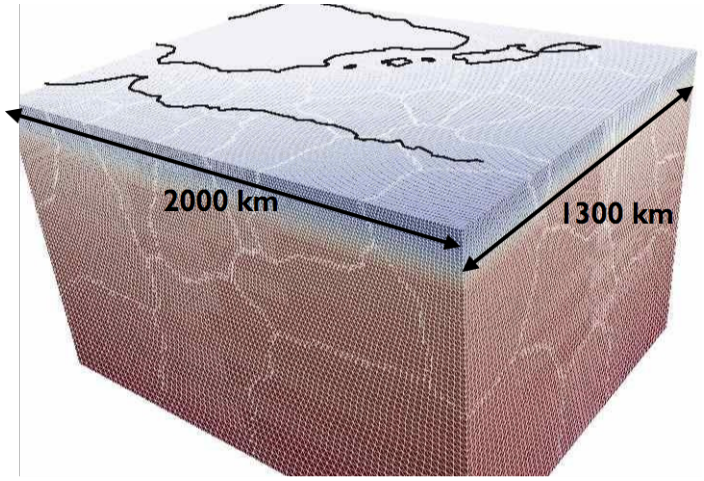

Figure 2.1. An example of a finite element mesh with the temperature field plotted in color, showing temperature increasing with depth from cold (blue) lithosphere to hot (red) mantle, with superimposed the map of the region. Irregular white lines denote the subdomain boundaries.

Free slip side boundary conditions are also used for some experiments on the vertical side boundaries in our 2D models of subduction evolution, while in other 2D experiments in Chapter 3 we have tested open side boundary conditions and show their efficiency for reducing the overall domain sizes. Free slip conditions prove to strongly affect model flow evolution while this is much less so when using open sidewalls (Chapter 3). As a consequence, open sidewalls allow for using smaller modeling domains reducing computational cost. Our open boundary conditions also allow experiments in which normal stress at the top of the sidewalls is imposed for the overriding and subducting plates (Chapter 3).

For the 3D numerical experiments of Chapters 4 and 5 only open side boundary conditions are used. These were combined with prescribed kinematic boundary conditions for lithosphere in- and outflow to a depth of 150 km. This way we can account for, and experiment with the effect of absolute plate motions on the subduction evolution in natural settings

(Chapters 4 and 5, respectively). In Chapter 5, we adopt the initial buoyancy and rheological settings that belong to the best performing subduction model of Chapter 4, and only vary the absolute plate motion conditions at the top of the southern and northern sidewall to study its effect on slab morphology evolution.

2.6 Initial conditions for 2D models.

In the 2D models presented in Chapter 3 we use oceanic lithosphere for both subducting and overriding plates. The initial age of the plates is varied in a range of 40-120 Myr. The initial temperature distribution within the lithosphere is determined from the equation of cooling of a semi-infinite half space [Turcotte and Schubert, 2002]. For the mantle a constant temperature gradient of 0.3 K/km is assumed. To create an initial buoyancy force (i.e. slab) in the model we push the subducted lithosphere from the top toward the trench by applying kinematic boundary conditions and allow it to subduct following a predefined curve with prescribed impermeable free slip condition mimicking the subduction fault. The initial slab buoyancy condition is created after 3-5 Myr of forced subduction. Next, the boundary condition for the top surface is changed to a free-slip condition and we remove the fault surface boundary conditions and allow flow to cross it freely. After these changes in initial settings we continue to model and investigate the model flow evolution based on self-consistent, internally driven, lithosphere subduction dynamics in 2D models.

2.7 Initial conditions and a 3D model setup for the western Mediterranean region.

In Chapters 4 and 5, 3D numerical modeling experiments are performed for investigating subduction evolution in the western Mediterranean region starting at ~35 Ma. The map of the region and a typical finite element mesh using the smallest domain is shown in Figure 2.1. The initial model geometry comprises six lithosphere domains with different rheology: two domains of old (>120 Ma) oceanic lithosphere (Central Atlantic and Western Alpine Tethys) for which we approximate the thermal structure from a cooling half space model assuming an age of 100 Ma [Turcotte and Schubert, 2002]; two continental lithosphere domains for which we assumed a lithosphere thickness of 150 km (Iberia and Africa) and a thermal gradient of ~10 K/km; and two

continental margins. This configuration is illustrated in Figure 2.2. The N-S oriented transition between Atlantic Ocean lithosphere and the continental domains was made for modeling convenience and does not significantly affect the subduction modeling we pursue. The western Alpine Tethys lithosphere located between Iberia and Africa has subducted since ~35 Ma leading to the present-day Rif-Gibraltar-Betic slab of which the 3-D subduction evolution is target of our investigations in Chapters 4 and 5.

For the determination of paleogeography of the lithosphere domains at ~35 Ma, we use the reconstruction of van Hinsbergen et al. [2014] which implements the latest constraints on Iberia and Africa motion [Vissers and Meijer, 2012a,b]. Time-averaged absolute plate motions for this region of the African plate (Atlantic-northern Africa) and of the Eurasian plate (Iberia) are derived from Doubrovine et al. [2012] and imposed on the top 150 km of the southern and northern sidewall.

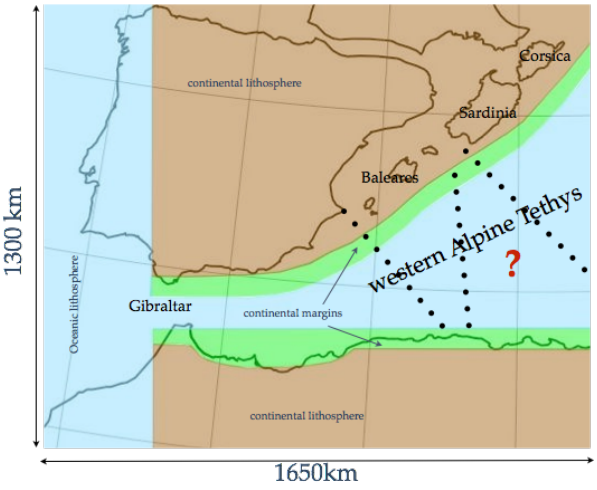

Figure 2.2. Paleo-geography of the western Mediterranean region in terms of continental and oceanic domains at ~35 Ma. Blue color represents oceanic lithosphere modeled in terms of thermal boundary layer, brown regions depict continental lithosphere limited in thickness to 150 km and green regions depict continental margins of which parts become subduction margin. Dotted lines indicate different proposed transform fault zones allowing for different subduction evolution of the regions at either side. The presented map view coincides with the smallest computational domain.

The initial subduction geometry at ~35 Ma is determined from three different tectonic reconstruction scenario, which we distinguish. For each scenario the subduction zone geometry and estimated slab length at ~35 Ma are used to determine the initial model buoyancy distribution. The proposed length of the slab varies from 120 km to more than 400 km [Faccenna et al., 2004; Verges and Fernandez, 2012; van Hinsbergen et al., 2014]. One of the continental margins depicted in Figure 2.2 will become an active subduction margin, dependent on adopted tectonic scenario. The remaining passive margins at ~35 Ma form a thermal transition from continental to oceanic lithosphere determined by interpolating the temperature profiles used for continental and oceanic lithosphere.

The rheological strength of the passive margin depends on several factors among which are margin age, its thermal structure, the presence or absence of active faulting in the region [Leroy, 2008; Handy and Brun, 2004]. Thus the strength of African and Iberian margins could be varied in numerical experiments of modeling the evolution of western Mediterranean. Margin strength is controlled by equation (2.2a,b), particularly by prescribing different initial values of τ_{max}. The average width of margins is 70 km except for the African margin of Morocco and west Algeria where a wider margin of 110 km was prescribed [van Hinsbergen et al., 2014].

In our 3D numerical experiments of Chapter 4 we will not only vary the initial values of margin strength but also experiment with different strength of mantle and lithosphere to model the subduction evolution of the western Mediterranean region. The prime target is to predict the first-order morphology of subducted slab under the region for which we test a wide range of parameter values (Table 2.2), both for strong and weak continental margins, while using the different initial subduction configurations as defined by the three different tectonic scenarios. In Figure 2.2, the dotted lines in the Western Alpine Tethys denote the possible position of weakness zone (section 2.3) that allow for different subduction evolution of the lithosphere at either side. These transform type boundaries have been proposed in tectonic reconstructions and we will experiment with them in Chapter 4.

References

1. Alisic, L., M. Gurnis, G. Stadler, C. Burstedde, and O. Ghattas (2012), Multi-scale dynamics and rheology of mantle flow with plates, J. Geophys. Res.,

117, B10402.
2. Billen, M.I., Hirth, G., 2007. Rheological controls on slab dynamics. Geochem. Geophys. Geosyst. 8, Q08012.
3. Billen, M.I. (2010), Slab dynamics in the transition zone. Physics of the Earth and Planetary Interiors, Volumes 183.
4. Burov, E.B. (2011), Rheology and strength of the lithosphere. Marine and Petroleum Geology. Vol. 28.
5. Chertova, M., T. Geenen, T., A.P. van den Berg, and W. Spakman (2012), Using open sidewalls for modeling self-consistent lithosphere subduction dynamics. Solid Earth Discuss. 4, 707-744.
6. Chertova, M.V., W. Spakman, T. Geenen, A. van den Berg, and D.J.J. van Hinsbergen (2014), Underpinning tectonic reconstructions of the western Mediterranean region with dynamic slab evolution from 3-D numerical modeling. JGR, vol. 119.
7. Christensen, U.R. and Yuen, D.A. (1984), The interaction of a subducting lithosphere slab with a chemical or phase boundary. Journal of Geophysical Research 89.
8. Čížková, H., J. van Hunen, and A.P. van den Berg (2007), Stress distribution within subducting slabs and their deformation in the transition zone. Physics of the Earth and Planetary Interiors. Volume 161, pages 202-214.
9. Čížková, H., A.P. van den Berg, W. Spakman, and C. Matyska (2012), The viscosity of Earth's lower mantle inferred from sinking speed of subducted lithosphere. Physics of the Earth and Planetary Interiors, Volumes 200–201, Pages 56-62, ISSN 0031-9201.
10. de Vries, J., A.P. van den Berg, and W. van Westrenen (2010), Formation and evolution of a lunar core from ilmenite-rich magma ocean cumulates, Earth and Planetary Science Letters, 292 (1-2), pp. 139-147.
11. Doubrovine, P. V., B. Steinberger, and T.H. Torsvik (2012), Absolute plate motions in a reference frame defined by moving hotspots in the Pacific, Atlantic and Indian oceans. Journal of Geophysical Research, 117, B09101, doi: 10.1029/2011JB009072.
12. Enns, A., T.W. Becker, and H. Schmeling (2005), The dynamics of subduction and trench migration for viscosity stratification. Geophys, J, Int., volume 160, pages 761-885.
13. Faccenna C., C. Piromallo A. Crespo-Blanc, L. Jolivet, and F. Rossetti (2004), Lateral slab deformation and the origin of the western Mediterranean arcs.

Tectonics;23:TC1012.
14. Gerya T.V. (2010) Introduction to Numerical Geodynamic Modelling. Cambridge University Press, 345 pp.
15. Handy, M.R. and J.P. Brun (2004), Seismicity, structure and strength of the continental lithosphere. Earth and Planetary Science Letters, 223 (3-4), pp. 427-441.
16. Hirth, G., and D. Kohlstedt (2003), Rheology of the upper mantle and the mantle wedge: a view from the experimentalists. In: Eiler, J. (Ed.), Inside the Subduction Factory. American Geophysical Union, Washington, DC.
17. Hockney, R.W. and J.W. Eastwood (1988), Computer Simulations Using Particles. IOP Publishing Ltd, Bristol.
18. Jacobs, M.H.G. and A.P. Van den Berg (2011), Complex phase distribution and seismic velocity structure of the transition zone: Convection model predictions for a magnesium-end member olivine-pyroxene mantle. Physics of the Earth and Planetary Interiors, 186 (1-2), pp. 36-48.
19. Karato, S. and M. Ogawa(1982), High-pressure recovery of olivine: implications for creep mechanisms and creep activation volume, Physics of the Earth and Planetary Interiors, 28 (2), pp. 102-117.
20. Karato, S. and P. Wu (1993), Rheology of the upper mantle: a synthesis. Science 260, 771–778.
21. Karato, S., M. Riedel, and D.A. Yuen (2001), Rheological structure and deformation of subducted slabs in mantle transition zone: implications for mantle circulation and deep earthquakes. Phys. Earth Planet. Int., 127, 83-108, 2001.
22. Karato, S. and H. Jung (2003), Effects of pressure on high-temperature dislocation creep in olivine polycrystals. Philosophical Magazine A 83, 401–414.
23. Leroy, M., F. Gueydan, and O. Dauteuil (2008), Uplift and strength evolution of passive margins inferred from 2D conductive modeling. Geophys. J. International, volume 172, pages 464-476.
24. Magni, V., J. van Hunen, F. Funiciello, and C. Faccenna (2012), Numerical models of slab migration in continental collision zones. Solid Earth, vol. 3, pages 293-306.
25. Mason, W.G., L. Moresi, P.G. Betts and M.S. Miller (2010), Three-dimensional numerical models of the influence of a buoyant oceanic plateau on subduction zones, Tectonophysics, Volume 483, Issues 1–2, Pages 71-79.

26. OzBench, M., K. Regenauer-Lieb, D.R. Stegman, G. Morra, R. Farrington, A. Hale, D.A. May, J. Freeman, L. Bourgouin, H. Mühlhaus, and L. Moresi (2008), A model comparison study of large-scale mantle–lithosphere dynamics driven by subduction. Physics of the Earth and Planetary Interiors, Volume 171, Issues 1–4, Pages 224-234, ISSN 0031-9201.
27. Schellart, W.P. and L. Moresi (2013), A new driving mechanism for backarc extension and backarc shortening through slab sinking induced toroidal and poloidal mantle flow: Results from dynamic subduction models with an overriding plate, J. Geophys. Res. Solid Earth, 118, 3221–3248.
28. Schott, B. and H. Schmeling (1998), Delamination and detachment of lithospheric roots. Tectonophysics, volume 296, pages 225-247.
29. Turcotte, D.L. and G. Schubert (2002), Geodynamics. Cambridge University Press.
30. Van den Berg, A., G. Segal, and D.A. Yuen (2014), SEPRAN: A versatile finite-element package for realistic problems in geosciences. Journal of Earth Sciences, submitted.
31. van Hunen, J. (2001), Shallow and buoyant lithospheric subduction: causes and implications from thermo-chemical numerical modeling. PhD thesis, Utrecht University, Utrecht.
32. van Hunen, J. and Allen, M.B. (2011), Continental collision and slab break-off: a comparison of 3-D numerical models with observations. Earth and Planetary Science Letters 302(1-2): 27-37.
33. van Summeren, J. (2008), Constraints on thermo-chemical convection from numerical modeling and geophysical data. Ph.D. Thesis, Utrecht University.
34. Vergés, J. and M. Fernàndez (2012), Tethys–Atlantic interaction along the Iberia–Africa plate boundary: The Betic–Rif orogenic system, Tectonophysics, Volume 579, 5 December 2012, Pages 144-172, ISSN 0040-1951.
35. Vissers, R. L. M., and P. T. Meijer (2012a), Iberia plate kinematics and Alpine collision in the Pyrenees, *Earth-Science Reviews*, *114*, 61-83.
36. Vissers, R. L. M., and P. T. Meijer (2012b), Mesozoic rotation of Iberia: subduction in the Pyrenees?, *Earth-Science Reviews*, *110*, 93-110.
37. van Hinsbergen, D.J.J., R.L.M. Vissers, and W. Spakman (2014), Origin and consequences of western Mediterranean subduction, rollback, and slab segmentation, *Tectonics*

Chapter 3

Using open sidewalls for modeling self-consistent lithosphere subduction dynamics

Abstract

Subduction modeling in regional model domains, in 2-D or 3-D, is commonly performed using closed (impermeable) vertical boundaries. Here we investigate the merits of using open boundaries for 2-D modeling of lithosphere subduction. Our experiments are focused on using open and closed (free slip) sidewalls while comparing results for two model aspect ratios of 3:1 and 6:1. Slab buoyancy driven subduction with open boundaries and free plates immediately develops into strong rollback with high trench retreat velocities and predominantly laminar asthenospheric flow. In contrast, free-slip sidewalls prove highly restrictive on subduction rollback evolution, unless the lithosphere plates are allowed to move away from the sidewalls. This initiates return flows pushing both plates toward the subduction zone speeding up subduction. Increasing the aspect ratio to 6:1 does not change the overall flow pattern when using open sidewalls but only the flow magnitude. In contrast, for free-slip boundaries, the slab evolution does change with respect to the 3:1 aspect ratio model and slab evolution does not resemble the evolution obtained with open boundaries using 6:1 aspect ratio. For models with open side boundaries, we could develop a flow-speed scaling based on energy dissipation arguments to convert between flow fields of different model aspect ratios. We have also investigated incorporating the effect of far-field generated lithosphere stress in our open boundary models.

By applying realistic normal stress conditions to the strong part of the overriding plate at the sidewalls, we can transfer intraplate stress to influence subduction dynamics varying from slab roll-back, stationary subduction, to advancing subduction. The relative independence of the flow field on model aspect ratio allows for a smaller modeling domain. Open boundaries allow for

* This chapter has been published as: Chertova, M.V., T. Geenen, A. van den Berg, W. Spakman (2012), Using open sidewalls for modeling self-consistent lithosphere subduction dynamics. Solid Earth, 3 (2), pp. 313-326.

subduction to evolve freely and avoid the adverse effects (e.g. forced return flows) of free-slip boundaries. We conclude that open boundaries in combination with intraplate stress conditions are to be preferred for modeling subduction evolution (rollback, stationary or advancing) using regional model domains.

3.1 Introduction

In the past decades, numerical modeling of lithosphere subduction has advanced considerably by incorporating coupling between plates, between plates and mantle, and by incorporating the complexity of detailed subduction zone processes (see Gerya [2011], for a review and references therein). Up to now modeling of regional subduction evolution is still being performed within spatially bound modeling domains in 2-D or 3-D [Quinquis et al., 2011; Jadamec and Billen, 2012]. The limited spatial domain particularly requires prescribing boundary conditions on the vertical sidewalls of the domain. These conditions are an important influence on the development of the model interior [Quinquis et al., 2011; Duretz et al., 2011, 2012; Ueda et al., 2012]. The usual attempt to reduce possible sidewall influence is by moving these far away from where subduction occurs by using a sufficiently large aspect ratio of model length to depth [Cizkova et al., 2012]. Boundary conditions on the vertical sidewalls can be no-slip (no flow at the boundary), free slip (impermeable; no flow through the boundary and zero traction in tangential direction), or open to some particular form of through-flow.

Free slip is the most commonly used boundary condition while open boundaries have been mostly limited to completely prescribed in- and outflow [van Hunen et al., 2000; Baes et al., 2010; Quinquis et al., 2011], or periodic conditions requiring that the through-flow at one side is the mirror image of through-flow on the other [Enns et al., 2004; Capitanio et al., 2010].

Open boundaries for which the horizontal in- and outflow are defined by a fully internally developed flow, have hardly been used and are the main topic of the present paper. Such open boundaries basically prescribe a hydrostatic pressure condition on the boundary preventing the model to collapse while horizontal in and outflow is free, in the sense that it is driven by the internal dynamics and the usual condition of incompressible flow. Among the range of boundary conditions used, open boundaries may fit best to real-mantle flow conditions surrounding subduction zones. We know of only one example

[Quinteros et al., 2010] of Eulerian modeling with non-periodic open boundaries.

Our aim in this paper is to investigate the benefits of using open boundaries as compared to using closed (free slip) conditions at the sidewalls of a two-dimensional (2-D) model domain. We focus on modeling self-consistent subduction driven by internal buoyancy and boundary stress conditions only, i.e. no kinematics are prescribed, in the presence of an overriding (oceanic) plate. Our focus will be on the effects of boundary conditions and model aspect ratios on subduction and mantle evolution. As our results show strong differences between using free slip and open boundaries, we are considering first order aspects only. Our results also show that with open sidewalls increasing the model aspect ratio does not change the overall evolution of subduction and mantle flow. In contrast, closed boundaries keep influencing the evolution of the model even for large model size of 6000 km by 1000 km. The primary reason is that closed sidewalls basically cause return flows from both sides towards the center of the model, which feeds back artificially into the evolving subduction process. We expect this also to hold for 3-D models despite the larger degree of freedom to develop lateral flow.

3.2 Model description

3.2.1 Model setup

We model self-consistent, internally driven, lithosphere subduction in the presence of an overriding plate in a 2-dimensional Cartesian geometry. Our main focus is on how distinctly different boundary conditions on the two sidewalls, open versus impermeable boundaries, affect subduction evolution. We will also investigate whether increasing the aspect ratio of the model domain from 3:1 (3000 km×1000 km) to 6:1 (6000 km×1000 km) is of influence, particularly, in reducing any observed adverse effect of boundary conditions.

The boundary condition for the top and the bottom of the box is free slip (impermeable). The surface condition will not allow for modeling topography but, as discussed later in Section 3.2.3, we impose a low-viscosity top layer of crust, which will partly compensate for the impermeability condition by allowing for lithosphere bending prior to subduction. For the right and left sides, different types of boundary conditions were implemented: open boundaries or free-slip boundaries. Open boundaries are implemented by

constraining zero tangential velocity on the boundary and by imposing a Lithostatic pressure condition for the normal stress on the boundary: $\sigma_n = P_{lith}$. This allows for horizontal in- and outflow purely driven by the internal dynamics of the model. The pressure condition prevents that the model collapses. As discussed in the introduction, open boundaries are hardly used in subduction modeling, but provide a more natural simulation of the mantle outside the model domain than the more common free-slip, impermeable boundary conditions. The free-slip condition prevents material transport through the boundary and forces the flow parallel to the boundary.

3.2.2 Governing equations

We adopt the Boussinesq approximation comprising three coupled equations, namely mass conservation of an incompressible viscous fluid,

$$\nabla \cdot u = 0 \tag{3.1}$$

the Stokes equation describing force balance,

$$-\nabla P + \nabla \cdot \tau = f(\rho) \tag{3.2}$$

and the heat equation, which here only takes into account heat diffusion and heat advection:

$$\rho c_p \frac{dT}{dt} - \nabla \cdot (k \nabla T) = 0 \tag{3.3}$$

(for explanation of symbols see Table 3.1 and Chapter 2). This system of equations is solved numerically using the finite element modeling package SEPRAN [Segal and Praagman, 2005]. The mesh element size varies from 1.5km in the trench region to 20km at the bottom of the model. Advection of the low viscosity material defining the crust and wedge is performed with a Lagrangian tracer technique where material properties are defined on tracers that are advected with the flow. Tracers are distributed initially only over the top 200 km of our domain where we use them to define rheological properties for a low viscosity top layer and wedge.

3.2.3 Rheological model

A composite rheology is used, which comprises dislocation and diffusion creep and a viscosity maximum η_{max} (Figure 3.1). The effective viscosity η_{eff} is determined as:

Symbol	Meaning	Value	Dim.
$\boldsymbol{c_p}$	Specific heat	1250	J $kg^{-1}K^{-1}$
$\boldsymbol{k}$	Thermal conductivity	4.27	W $m^{-1}K^{-1}$
R	Gas constant	8.31	$JK^{-1}m^{-3}$
α	Thermal expansivity	3×10^{-5}	K^{-1}
$\boldsymbol{\rho_0}$	Reference density	3413	Kg m^{-3}
$\boldsymbol{Ra}$	Thermal Rayleigh number,$\rho_0\alpha\Delta T h^3/\eta_0\kappa$	1.7×10^{6}	-
	Slab initialization	3.5	My
	Slab retreating	10-30	My
	Age of the lithosphere	100	My
$\boldsymbol{\eta_0}$	Reference viscosity	10^{21}	Pa s
γ_1	Clapeyron slope (410 km)	4.1	$MPaK^{-1}$
$\boldsymbol{\delta\rho_1}$	Density contrast (410 km)	273	Kg m^{-3}
γ_2	Clapeyron slope (660 km)	-1.9	$MPaK^{-1}$
$\boldsymbol{\delta\rho_2}$	Density contrast (660 km)	342	kg m^{-3}
$\boldsymbol{\eta_{LM}}$	Viscosity of the lower mantle	2×10^{22}	Pa s
v_{subd}	Initial subduction velocity	10	cm yr_{-1}
$\boldsymbol{A_{diff}}$	Diffusion prefactor	5.3×10^{15}	s^{-1}
$\boldsymbol{A_{disl}}$	Dislocation prefactor	2×10^{18}	s^{-1}
$\boldsymbol{V_{diff}}$	Activation volume for the diffusion creep	5	cm^3mol^{-1}
$\boldsymbol{V_{disl}}$	Activation volume for the dislocation creep	10	cm^3mol^{-1}
$\boldsymbol{E_{diff}}$	Activation energy for the diffusion creep	240	KJ mol^{-1}
$\boldsymbol{E_{disl}}$	Activation energy for the dislocation creep	423	KJ mol^{-1}
$\boldsymbol{b}$	Burgers vector	5×10^{-10}	m
$\boldsymbol{d}$	Grain size	10^{-6}	m
$\boldsymbol{m}$	Grain size exponent	2.5	-
$\boldsymbol{n}$	Stress exponent dislocation creep	3	-
$\boldsymbol{T_0}$	Normalized surface temperature, $T_{surf}/\Delta T$	0.1605	-
$\boldsymbol{Di}$	Dissipation number, $\alpha g h/c_p$	0.24	-
$\boldsymbol{\Phi}$	Viscous dissipation	-	W m^{-3}
γ	Yield stress gradient	0.1-0.6	-
$\boldsymbol{\dot{\varepsilon}}$	Second invariant of the strain rate, $(1/2\Sigma_{ij}\dot{\varepsilon}_{ij}{}^2)^{1/2}$	-	s^{-1}
$\boldsymbol{u_j}$	*i*-th component of the velocity	-	-
$\boldsymbol{P}$	Lithostatic pressure	-	-
$\boldsymbol{\partial_i}\Delta$P	Dynamic pressure gradient, $\partial_i P - \rho_0 g_i$	-	-
$\boldsymbol{\tau_{ij}}$	*Ij*-th component of the deviatoric stress tensor, $\eta\dot{\varepsilon}_{ij}$	-	-
$\boldsymbol{T}$	Temperature	-	-
$\boldsymbol{\dot{\varepsilon}_{ij}}$	Strain rate, $\dot{\varepsilon}_{ij} = \partial_i u_j + \partial_j u_i$	-	-
μ	Shear modulus	80×10^{9}	Pa
h	Height of the model domain	1000	km
	Width of the domain	3000-6000	km

Table 3.1. Parameters of the model

$$\frac{1}{\eta \text{eff}} = \frac{1}{\eta_{diff}} + \frac{1}{\eta_{disl}} + \frac{1}{\eta \text{max}},$$

with $\eta_{max} = 10^{24}$Pa s limiting the effective viscosity in the coldest parts of the lithosphere, with the viscosity due to diffusion creep,

$$\eta_{diff} = \mu A_{diff}^{-1} (b/d)^{-m} exp[(E_{diff} + PV_{diff})/RT], \quad (3.4)$$

and dislocation(power law) creep

$$\eta_{disl} = \mu \, A_{\text{disl}}^{-\frac{1}{n}} \dot{\varepsilon}^{\frac{1-n}{n}} exp[(E_{\text{disl}} + PV_{\text{disl}})/nRT], \quad (3.5)$$

where $\dot{\varepsilon}$ is the second invariant of the strain-rate tensor, A_{diff}, A_{dis} are diffusion and dislocation creep viscosity prefactors, μ is the shear modulus, b is Burgers vector, d is the grain size, m is the grain size exponent, $V_{diff,dis}$ and $E_{diff,dis}$ are activation volume and activation energy for diffusion and dislocation creep, respectively, P is the lithostatic pressure and T - temperature (Table 3.1). Parameters are taken for wet olivine [Karato et al., 2001], values are given in Table 3.1. Activation volumes, energy and grain size were chosen to fit seismic studies and postglacial rebound estimations of upper mantle and asthenosphere viscosities [Kaufmann, 2000; Burgan and Dresen, 2008; Simmons et al., 2006].

3.2.4 First order phase changes

Our models include the two major phase transitions at approximately 410 km and 660 km depth. The values of the Clapeyron slope and density contrast are given in Table 3.1. These parameters are chosen following Billen [2010]. The 410 km phase change contributes to the buoyancy force and increases slab pull. The phase change at 660 km has a positive buoyancy effect on cool material resisting slab penetration to the deeper mantle. We ignore thermal effects associated with the phase changes. Phase transitions are parameterized in the model with the phase-transition function:

$$\Gamma_k = \frac{1}{2}[1 + \sin\left(\frac{\pi z_{diff}}{w}\right)] \quad (3.6)$$

where $zdiff = z - z_{tr} - \gamma_k \cdot (T - T_{tr})$, w is the half-width of k transition zone set to 50 km, z_{tr} and T_{tr} are the reference depth and temperature of the phase transition, respectively, γ_k is the Clapeyron slope, T is temperature [Cristensen and Yuen, 1985; van Hunen, 2001].

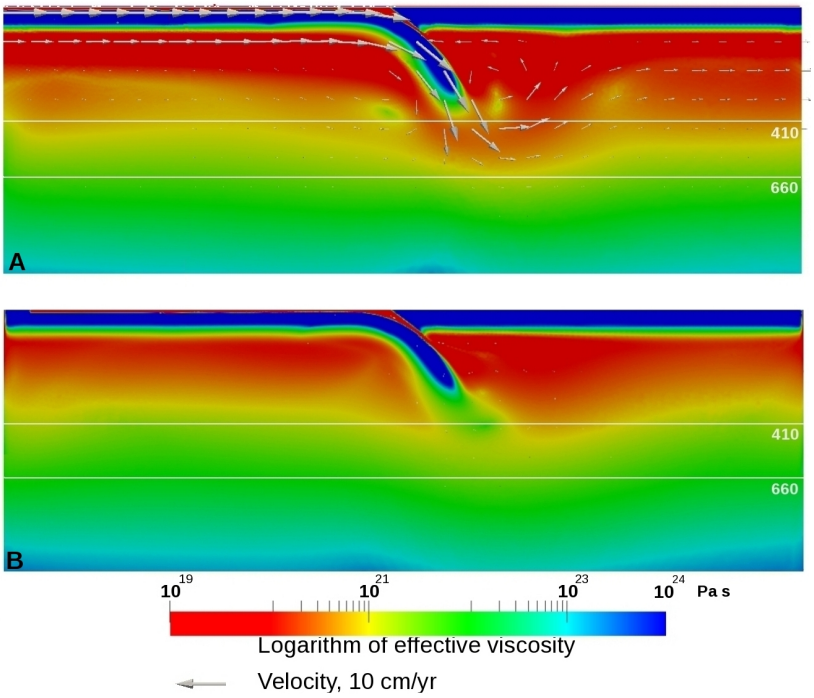

Figure 3.1. The rheology and flow field after the initial 3.5My of kinematically forced subduction consistent with (A)- open sidewalls, (B)- closed sidewalls. The color scale shows 10-logarithm of effective viscosity. White lines corresponds to the approximate position of phase transition zones at 410km and 660km.

3.2.5 The starting configuration leading to the initial buoyancy field

To enable internally driven subduction, first an initial buoyancy distribution is created by kinematically forced subduction (10 cm/yr) along an arc-shaped fault extending from 0 to 300 km depth. The lithosphere temperature distribution prior to subduction is determined from the equation of cooling of a semi-infinite half-space [Turcotte and Schubert, 2002] for a lithosphere age of 100 My. Boundary temperature conditions are T = 273 K at the surface, T = 2000 K at the bottom. On the side boundaries we prescribe a stationary temperature profile during the subduction process. This also defines the thermal structure of the overriding plate.

We implemented a 10 km thick weak layer (10^{19} Pa s) on the top of the subducted plate [Han and Gurnis, 1999; Manea and Gurnis, 2007; Cizkova et al., 2007; Behounkova and Cizkova, 2008; Babeyko and Sobolev, 2008; Quinteros et al., 2010]. This mimics a subduction channel and proves sufficient for initiating and maintaining subduction in our modeling. An accretionary wedge of weak crust is formed above the subduction zone and has the advantage to prevent artificial rheological coupling between the subducting and overriding plates. The presence/absence of the accretionary wedge only leads to small differences in dip angle and stress field of the trench zone and does not affect the overall subducting slab evolution for the boundary conditions we consider in our models, we conclude from various tests. The focus in our paper is on the large-scale evolution of the subduction system linked to various boundary conditions and aspect ratios of the model domain rather than on the detailed evolution of the plate boundary region.

Figure 3.1a shows the initial rheology field for the model with open boundaries. In the oldest part of the slab, both dislocation and diffusion creep give high viscosity values, which are limited here by $\eta_{max} = 10^{24}$ Pa s. In the asthenosphere viscosity decreases to values of 10^{19} Pa s, below which it increases to 0.5×10^{21} Pa s in the transition zone and to 10^{22} Pa s at the top of the lower mantle. The tip of the slab in this initial configuration shows thickening due to mantle resistance, which is also visible in the τ_{22} component of the stress distribution (Figure 3.2). The starting configuration, rheology and flow field, using free-slip sidewalls is illustrated in Figure 3.1b. The two types of boundary conditions, closed or open, lead to a different internal flow field and velocity gradient field on which viscosity depends. Therefore, the starting configuration, particularly the viscosity field, depends on the boundary conditions used and is different when using open sidewalls or free-slip sidewalls.

The dominant deformation mechanisms acting in the initial model are shown in Figure 3.3. Diffusion creep (red) is dominant below the asthenosphere and away from the slab, where dislocation creep is active. Small red regions beneath the overriding plate correspond to low strain rate regions. In the core of the slab and overriding plate, the viscosity is limited to $\eta_{max}=10^{24}$ Pa s. The low viscosity crustal layer and accretionary wedge are shown in yellow.

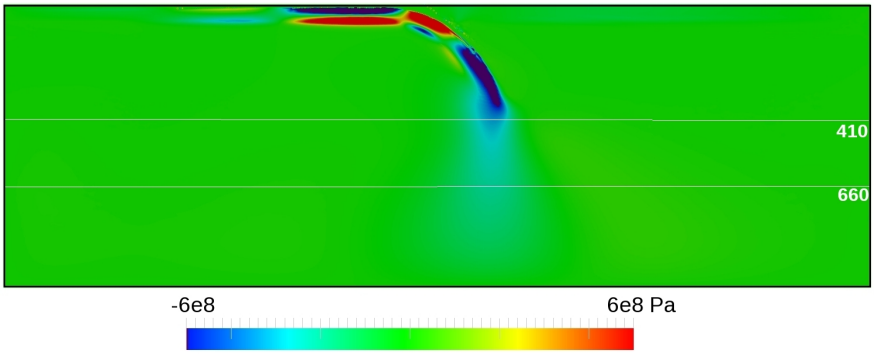

Figure 3.2. Stress component τ_{22} for the initial model with open boundaries after 3.5My of kinematically forced evolution (Figure 3.1a). Note the down-dip compression in the slab.

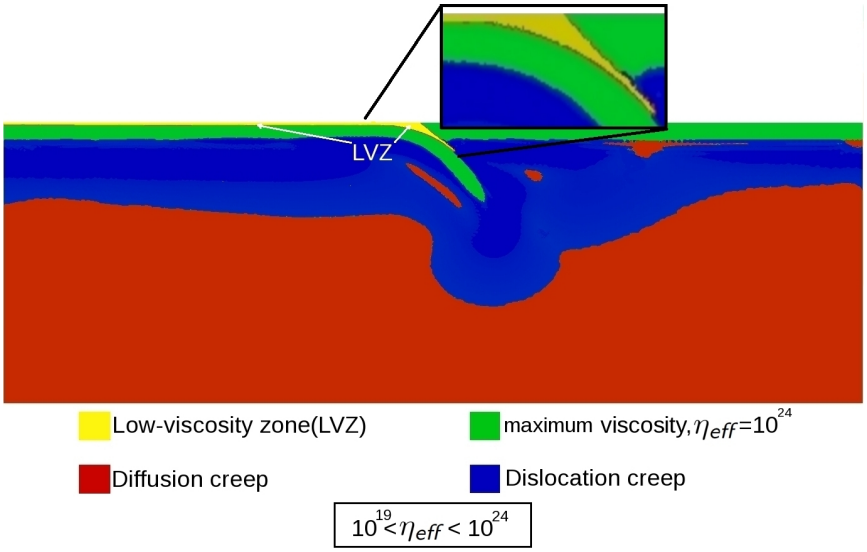

Figure 3.3. Dominant deformation mechanism in the initial model with open side boundaries of Figure 3.1a. Different colors correspond to regions where the individual deformation mechanism is dominant.

3.3 Results of numerical modeling

We first focus on models with open versus closed boundary conditions and on model domains with different aspect ratios. This concerns end-member models driven by slab buoyancy only. Subsequently, we incorporate far-field effects additionally constraining the motion of the upper plate. These are

imposed by means of normal-stress boundary condition (τ_{11}) acting on the strong lithosphere at the sidewall. This condition allows investigating stationary or advancing subduction using open boundaries of which we will show several results.
After the initial 3.5My of kinematically forced subduction has provided an initial buoyancy configuration as discussed in Section 3.2.5, the forcing is removed and the internal dynamics take over in driving subduction. We label the models using "O" to denote open, "C" for closed, "R" for "spreading ridge", and "3" and "6" to denote aspect ratios 3:1, and 6:1, respectively.

3.3.1 Open versus closed vertical boundaries and aspect ratio of 3:1

For the models with aspect ratio 3:1, Figure 3.4 shows the velocity field and rheology structure of four models (columns) at 2 My intervals (rows) and with different boundary conditions on the left and right sidewalls.
Figure 3.4a depicts the evolution of the model OO3 with two open side boundaries. During the initial stage, about 3.5– 4 My from the beginning of the subduction, we observe a strong horizontal flow associated with the subducting plate. This flow pattern bends into the subduction zone following the slab. During this early stage, the upper plate does not move appreciably. However, in the next 2 My slab rollback starts and forces an overall left directed horizontal flow of the upper plate and its underlying asthenosphere. The subducting plate is still being pulled into the subduction zone, but with decreasing speed. Around 5.5 My the slab reaches the base of the upper mantle and further subduction meets resistance due to slab interaction with the 660 km phase transition and with the increased mantle viscosities of the lower mantle. This is followed by the onset of increased slab retreat. The overriding plate attains velocities of 10–15 cm/yr, while the advance velocity of the subducting plate drops down to small values (2–3 cm/yr). During the subsequent subduction evolution, we observe strong horizontal left-directed laminar flow concentrated in the asthenosphere and characterized by low viscosity (red colors) in Figure 3.4a. This development proves to be characteristic for models with open boundaries and driven by slab buoyancy only.
Figure 3.4b illustrates the evolution of a model with a closed left and an open right boundary (CO3). The closed left boundary effectively fixes the upper plate to the side. During the whole evolution of the subduction process, we

observe a low velocity magnitude (more than 10 times lower than for model OO3). As a result also the viscosity structure is different from model OO3.
The minimum viscosities for the asthenosphere, corresponding to lower strain rate, are higher (around 1 order of magnitude), and the rheological width of the asthenosphere is reduced considerably. After the slab reaches the top of the lower mantle, we observe no more trench retreat and the velocity magnitude drops to almost zero. This occurs because the left part of the domain effectively forms a closed volume at this stage in which the slab is blocking flow to the right part of the domain. This is a pure 2-D effect. In 3-D modeling flow is developing at the (open) lateral edge of the slab, which allows material to move away sideways from below the slab [OzBench et al., 2008; Stegman et al., 2010; Funiciello et al., 2003; Piromallo et al., 2006].
Figure 3.4c shows the evolution of a model with closed boundaries on both the left and right sides. The closed left boundary again fixes the upper plate, but at the closed right boundary a spreading ridge is allowed to develop in the upper right corner of the model (CCR3) [Enns et al., 2004].
The spreading ridge enables the lithosphere plate to separate from the vertical boundary by allowing hot asthenosphere to flow upward. This facilitates more free lateral movement of the upper plate and is initiated by defining a warm weak zone at the boundary in the initial temperature field. For this model we also observe much lower flow magnitudes (1 cm/yr after arriving of the slab at the 660 km boundary) compared to OO3 and, correspondingly, a different evolution of the viscosity structure. The slab behavior and trench rollback are similar to the model CO3 except one difference: in model CCR3 a gap between the subducted slab and the overriding plate forms. This gap is filled with asthenosphere material as can be seen from Figure 3.4c mimicking the formation of a backarc basin. While in model CO3, the open right boundary allows for modest inflow of asthenosphere material with flow speeds comparable to the overlying upper plate, this does not happen in model CCR3. When the slab reaches the bottom of the upper mantle material exchange with the left part of the model is mostly blocked as in model CO3. However, the closed right boundary now forces an asthenospheric return flow in response to slab rollback with larger magnitude than the free upper plate can attain. As a consequence back-arc basin opening develops.

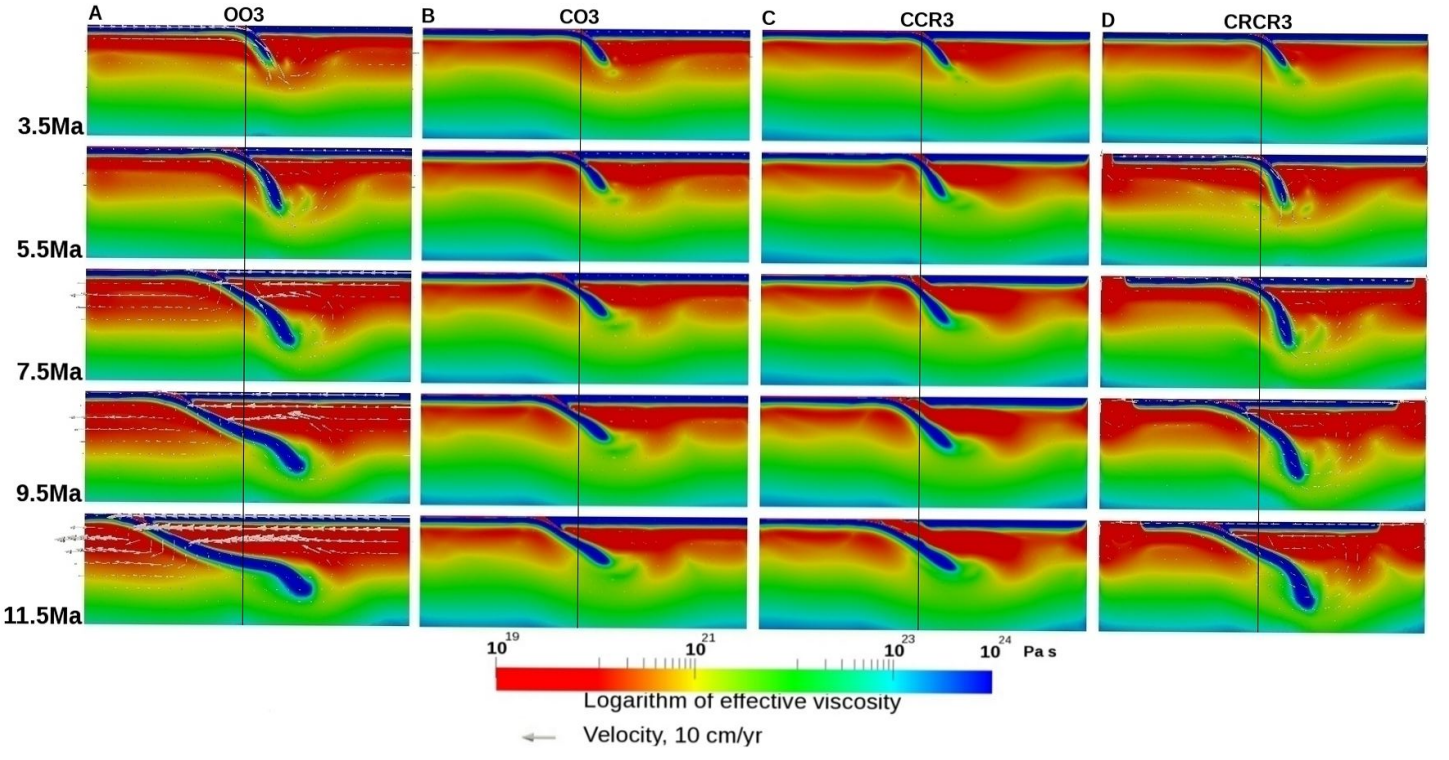

Figure 3.4. Evolution of the subduction process for model OO3 with open boundaries, model CO_3 closed left and open right boundary, model CCR3 with closed right and left boundaries with spreading center on the right boundary and model CRCR3 with closed boundaries. Arrows show the direction and magnitude of flow field. Identical scaling of the velocity vectors applies to all cases.

Lastly, Figure 3.4d illustrates the evolution of a model with closed boundaries but with spreading ridges in both upper corners (CRCR3) allowing both lithosphere plates to separate from the sidewall. Although the 3:1 aspect ratio was wide enough to enable the development of large horizontal flow in the model with open boundaries OO3, this proves more complicated for model CRCR3 with closed boundaries in combination with free plates. We observe strong boundary influence on the motion of the plates and the flow field around the slab. This flow is directed upward close to the vertical boundaries and pushes both plates toward the subduction zone. For this model with closed boundaries and free plates, we observe a lower velocity for the overriding plate (5–6 cm/yr on average) compared to OO3 model and higher viscosities for the asthenosphere. The rollback process develops slower than in model OO3, but the evolution of the slab and the overriding plate, as well as the evolution of rollback, are more similar to the model OO3 than to models CO3 and CCR3. No back-arc basin evolves in model CRCR3. The reason is that, while rolling back, the subducting plate is still advancing as can be inferred from the slab reaching larger depths, which reduces the sinking velocity and no gap appears between upper and lower plate.

3.3.2 Comparison of the end-member (OO3 and CRCR3)

From the velocity vector plots, Figures 3.4a and 3.4d, a clear difference in the magnitude of flow between the models OO3 and CRCR3 is observed, illustrating the strong impact of the choice of boundary conditions. Despite the smaller rollback rate, we observe higher horizontal velocities of the subducting plate for the closed boundary case CRCR3, as a result of the ridge push from the spreading centers at both sides of the subduction zone. The flow patterns in both models are distinctly different: in model OO3 a strong lateral flow is created by slab rollback pushing material out of the model domain. This sets up a high-magnitude channel flow in the low-viscous asthenosphere (peak velocity 16.5 cm/yr). For the model with closed boundaries, the flow aligns with the slab and splits up into two cells with upward limbs near the side boundaries.

Besides the differences in magnitude of the velocity field, we notice also a difference in rheological structure. For model OO3, at the start of the subduction process, the minimum viscosities in the asthenosphere are around 10^{19} Pa s. For model CRCR3 these are by one order of magnitude larger.

These viscosity values decrease with time, but the asthenosphere in model CRCR3 stays narrower than in model OO3. This feature is related to the dominant deformation mechanism in the asthenosphere, which is strain-rate dependent dislocation creep (Figure 3.2). Overall, viscosity values in model CRCR3 are larger during the entire subduction process.
The evolution of the subduction angle is also different between the two end member models OO3 and CRCR3: for model OO3 it gradually decreases while for model CRCR3 it increases with time. This is related to the large difference in the speed of trench retreat while the deep part of the slab is not moving backward. In OO3 this changes the average slab dip and subduction angle. In model CRCR3, the slab penetrates deeper into the lower mantle during the subduction process as a result of a smaller rate of trench retreat creating a steeper average subduction angle.

3.3.3 Comparison of models with different aspect ratios

One possible way to reduce the influence of the sidewalls conditions on the evolution of lithosphere subduction is to increase the width of the domain, but at increased cost of computations. To investigate this we increased the domain width to 6000km doubling the aspect ratio to 6:1. Figure 3.5 shows results for models with open and closed sidewalls with spreading ridges, labeled OO6 and CRCR6, respectively. The flow fields are illustrated here by plotting the instantaneous streamlines, which show again significant differences between both models.
For model CRCR6, the velocity magnitude is smaller (after 14 My of subduction maximum velocities are 6.5 and 3.5 cm/yr for OO6 and CRCR6 respectively) and the lowest viscosities beneath the slab are at least 10 times higher than in model OO6. Similar observations were made for model OO3 and CRCR3. Figure 3.6 shows vertical profiles of horizontal velocity computed at different distances from the left side of the models OO6 and CRCR6 after 14 My from the beginning of the subduction process. These profiles clearly illustrate the difference between the flow regimes for these two models. Particularly for model OO6, it illustrates the channel flow regime of the asthenosphere as well as plate-like behavior [van den Berg et al., 1991; Turcotte and Schubert, 2002]. Flow velocities in the asthenosphere channel are much higher for the open boundary case, while plate velocities are higher for the closed boundary case with free plates. Apparently the slab rollback

process produces a significant pressure gradient that drives laminar flow in the asthenosphere.

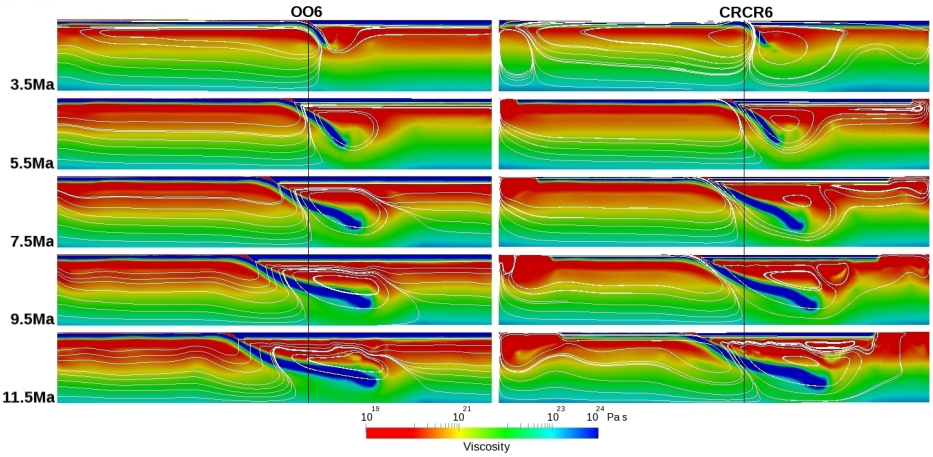

Figure 3.5. Snapshots of the effective viscosity and flow pattern for 2 subduction models, on the right-model domain with ratio 6:1, closed boundaries (CRCR6), on the left-model domain with ratio 6:1, open boundaries (OO6).

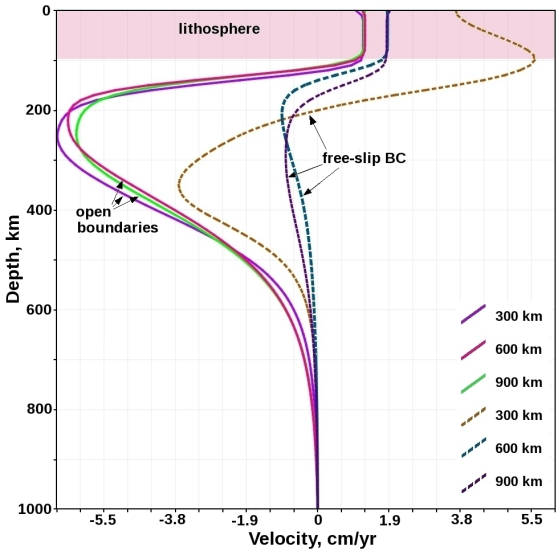

Figure 3.6. Velocity profiles for the model with open boundaries, OO6 (solid lines) and model with closed boundaries, CRCR6 (dashed lines). Profiles were taken after 14 My from the beginning of the subduction process, distances from the left side of the model domain indicated in the legend.

For the closed boundary model CRCR6 the flow tends to follow the slab then deflects downward and forms closed streamlines. In this model the return flow in the upwelling limbs of the convective cells at both sides contributes to the convergence of the two plates, which puts the subduction channel under lateral compression. For models with a thin crustal weak layer this lateral compression may lead to locking between the subducting and overriding plates. We conclude that using a larger aspect ratio does not reduce the differences in subduction evolution and overall flow field between models with open and closed boundaries.
In contrast, model CRCR3 shows weaker slab rollback associated with only little asthenosphere return flow from the far-field. Flow patterns around the slab in model CRCR6 are different from those in OO6 due to the different retreat velocity and the return flow resulting from the closed sidewalls. In model OO6 with open boundaries streamlines cross the slab and leave the domain, illustrating that the boundary does not obstruct the slab migration.

3.3.4 Rollback velocity and the overall magnitude of flow speed

The almost uniform velocities within the subducting and overriding plates allow us to focus on the speed of slab rollback measured from the trench position through time. Figure 3.7 shows the speed of rollback for the models with aspect ratio 3:1 and 6:1 and different side boundary conditions. For the models OO3 and CRCR3, yellow and green curves respectively, Figure 3.7 shows the difference between rollback speed amounting to a factor of nearly 3 after 8 My of subduction. We observe common trends in the development of the rollback speed: (1) until the slab reaches the 410 km phase change, the speed of rollback increases with a factor of 2; (2) next subduction rollback slows down until the slab reaches the 660 km phase change and the top of the lower mantle; (3) Lastly, slab rollback continues while the tip of the slab is hanging in the highly viscous lower mantle, i.e. without an increase in the penetration depth of the slab.
For model OO3, we observe an increase in rollback speed during this last stage of subduction, which is linked to the trench coming closer to the open boundary. This latter effect is not observed in the 1:6 aspect ratio model OO6 (Figure 3.7, blue curve). For model OO6, the rollback speed stabilizes after the slab tip gets stuck in the high viscosity lower mantle. Model CRCR6 (Figure 3.7, red curve) with free plates has a particular evolution from initially

no rollback to strongly increasing speeds peaking around 8 My. This evolution is dominated by the detaching of the overriding plate from the right boundary while low-viscosity mantle material starts filling the gap. Figure 3.7 demonstrates in a different way the large effects of boundary conditions, open versus closed, which cannot be reduced using larger aspect ratio.

Another large difference between the results obtained for different aspect ratios of the modeling domain concerns the overall magnitude of flow speed of the lithosphere plates, subduction speed and mantle flow. Figure 3.7 shows that for the 3:1 model with open boundaries the average rollback speed is roughly 15 cm/yr, whereas for the model with aspect ratio 6:1 it is around 5 cm/yr. A similar reduction in flow speed characterizes the mantle flow. In all aspect-ratio cases the initial driving slab buoyancy is the same. These flow speed reductions can be tied to the longer length of the lithosphere plates in the 6:1 models causing a longer sub-lithospheric frictional shear zone where a significant part of the mechanical energy of the system is dissipated.

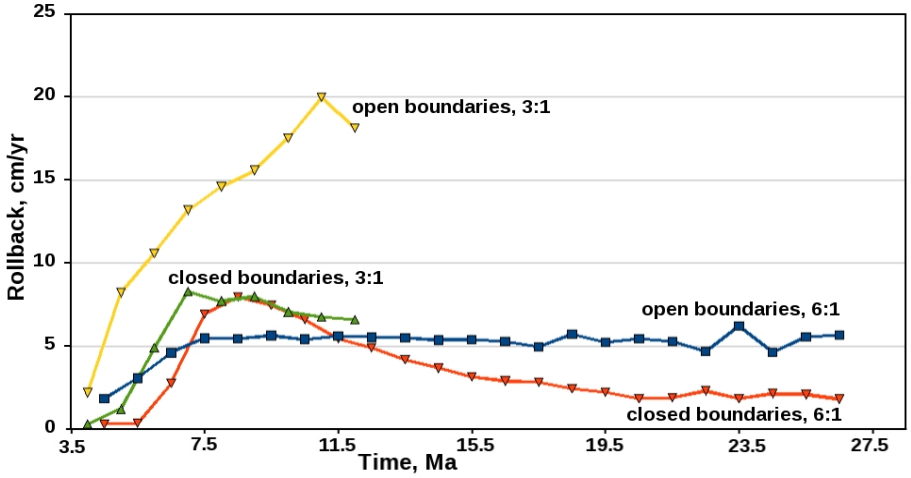

Figure 3.7. Speed of rollback for the model with open boundaries and model with closed boundaries: model OO3 (yellow line), model CRCR3 (green line), model OO6 (blue line) and model CRCR6 (red line).

For models with open boundaries, we can, in an approximate way, compensate for the reduced (increased) effect of viscous dissipation in the 3:1 (6:1) models by a scaling relation applied to the velocity field and which accounts for the effect of additional viscous dissipation in an extended computational domain. To determine this velocity scaling, we investigated

aspect ratios of 3:1, 4:1, 5:1 and 6:1, where an aspect ratio of 6:1 would correspond to the ocean half-width of 3000 km of the subducting plate. The scaling procedure is explained in more details in Appendix A. The scaling procedure compensates the overall velocity field for the effect of bottom-side traction of that part of the plate located outside the model domain, which allows to account for bottom-side traction of the whole plate from the spreading ridge to the trench. In combination with intraplate stress imposed at the sidewalls, it facilitates modeling of a natural subduction process with correct plate length and ridge push within a smaller model domain.

This scaling procedure has been applied during the computation of the OO3 model to approximate flow speed results as observed for the 6:1 aspect ratio. Figure 3.8 shows scaled rollback velocities of the OO3 model together with original (unscaled) velocities for both the OO3 and OO6 models. These results illustrate the feasibility of approximate upscaling the numerical results for a larger domain. For the models with closed boundaries, we cannot apply velocity scaling due to lateral variations of the flow close to the side boundaries. For models with closed boundaries not only the velocity magnitude but also the flow pattern is changing with decreasing/increasing domain size. In this case comparison of the subduction dynamics in models with different aspect ratio is not meaningful.

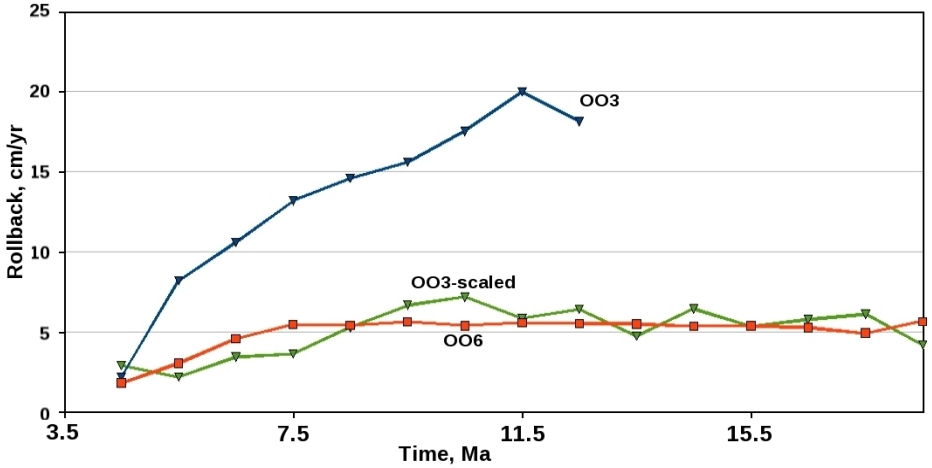

Figure 3.8. Evolution of the speed of rollback for two models: model OO3 with aspect ratio 3:1 (blue line), and model OO6 with aspect ratio 6:1 (red line) and scaled speed of rollback for the model OO3 with aspect ratio 3:1 (green line)

3.3.5 Constraining the motion of the lithosphere plates

In the open boundary models OO3 and OO6, the motion of the subducting and overriding plate is entirely controlled by the buoyancy of the subducting slab. We invariably observe (relatively fast) slab rollback in these models, whereas on Earth not all subduction zones show strong rollback and advancing trenches are also proposed [Funiciello et al., 2008; Schellart et al., 2008]. OO3 and OO6 are in fact end member models as on Earth the global coupling between plates may impose far-field control on the velocity of both overriding and subducting plate. We devised a number of experiments to investigate the combination of far-field control and local slab buoyancy on the evolution of subduction using various boundary conditions in combination with open boundaries.

As a first open-boundary experiment, we impose far-field control by just fixing (F) the upper plate to the right boundary (model OOF3). We compare this to a model in which the left boundary is open while the right boundary is entirely closed (model OC3). The latter experiment is similar to that of Quinteros et al. [2010] who also use a single open vertical boundary in their numerical modeling of free slab movement.

Results are presented in Figure 3.9 showing snapshots of the effective viscosity field at 5 My intervals. The initial models at 3.5 My are similar apart from the fact that model OOF3 already shows clear laminar flow field in the asthenosphere under the overriding plate as facilitated by the open boundaries. During the next 5My the flow fields are of comparable magnitude and differ mostly in the flow near the tip of the slab. The average slab dip develops different between the models and particularly when the slab reaches the transition zone the evolution of these models starts to diverge. For model OOF3, active subduction continues and the slab penetrates deeper under the overriding plate, although with a decreasing speed and with overall shape deformation (along dip buckling) as a result of the interaction with increased viscosities at depth.

In the second model (OC3), the slab starts hanging in the transition zone after 8 My of evolution, the dip angle increases and the slab tends to overturn. The position of the trench does not change with time. The flow field pattern to the right of the slab is completely different from that of model OOF3 with an open right boundary, which allows flow to leave the domain. In the second model OC3, the closed right boundary creates a circulation beneath the upper

plate, which in combination with increasing viscosity below 660 km depth results in slab bending and folding.

To avoid prescribing plate velocities, we can devise a more general implementation of the far-field control by imposing an intraplate stress as a normal traction on the open boundary from the surface down to the base of the lithosphere. We applied this to the upper plate only. Some examples are presented here demonstrating that open boundaries in combination with intraplate stress constraints can lead to strongly reduced slab rollback, (temporary) stationary subduction, or even advancing trenches as compared to the end-member "free" in/outflow models OO3 or OO6.

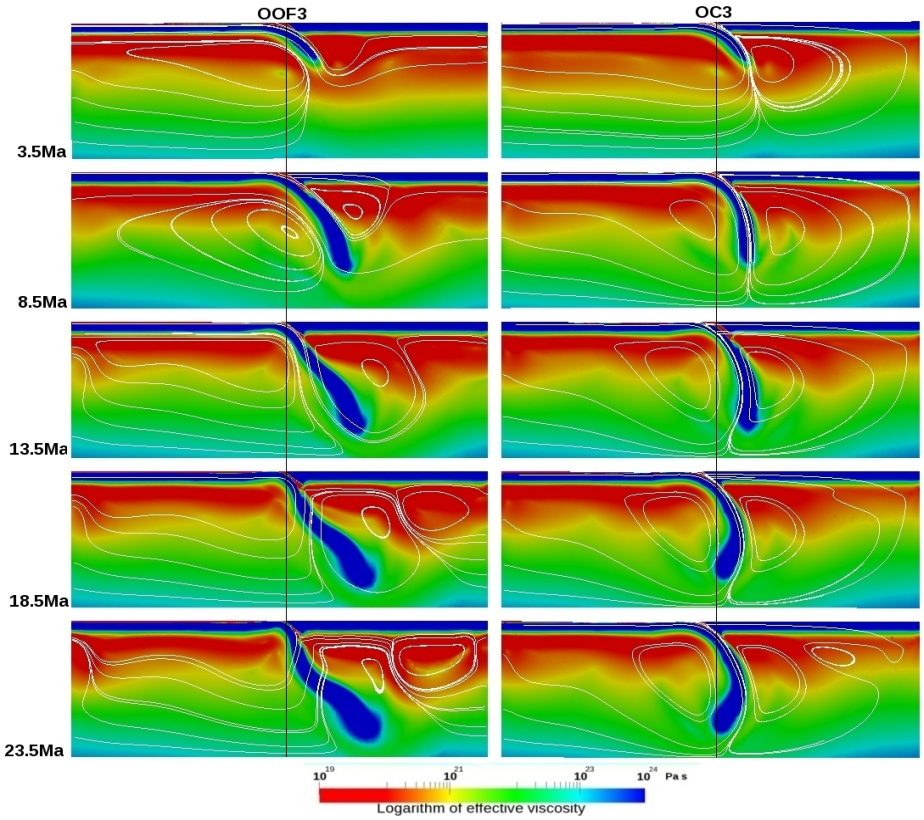

Figure 3.9. Evolution of the subduction process for model OOF3 with open boundaries and fixed overriding plate (on the left) and model OC3 with closed right boundary (on the right).

We varied the applied intraplate stress within reasonable limits for subduction zones (up to 52 MPa, Lithgow-Bertelloni and Guynn [2004]). The results of the subduction models with different intraplate stress values applied to the upper plate are presented in Figure 3.10 where a pull is exerted of 18 MPa (10A), 36 MPa (10B), and 52 MPa (10C) on the upper plate. With increasing value of the intraplate stress we generally observe decreasing trench retreat. In more detail Figure 3.10b shows an initial stage of stationary subduction, while Figure 3.10c exhibits an initial phase of trench advance (to the right). These initial stages differ when as a result of a relatively short slab, the slab pull is still small and the pull on the upper plate is able to force stationary subduction or even slab advance. When the slab touches the 660-km boundary, there is a short episode of trench-stationary subduction, and after a few My trench retreat develops in the model [Funiciello et al., 2003]. These results demonstrate that open boundaries are not restrictive on modeling rollback, stationary subduction or trench advance. In addition they again demonstrate the strong dependence of the evolution of trench motion and slab morphology on boundary conditions.

3.4 Discussion and conclusions

In this paper we set out to investigate the merits of using open sidewalls in 2-D modeling of subduction evolution as opposed to the more common impermeable free-slip condition. The particular implemented condition is to maintain lithostatic pressure at the boundaries while flow perpendicular to the boundary is free. The internal buoyancy in combination with normal stress conditions (pull/push) on the cross sectional area of the two lithosphere plates, is driving the flow. The absence of kinematic boundary conditions leads to a fully dynamic, self-consistent evolution of the internal dynamics of the model. Simulating a weak upper crust (10 km thick, 10^{19} Pa s) allowed for modeling continuous subduction without prescribing a particularly subduction channel geometry. We observed that changing the aspect ratio for models with open boundaries did not change the general flow patterns and subduction evolution, except for a general drop in flow speed amplitude for which we derived an approximate scaling procedure based on energy dissipation.

The modeling results obtained with the usual free-slip condition (no horizontal flow) at the sidewalls are in strong contrast with the results obtained for open boundaries. We observed in all experiments a strongly deviating subduction

evolution due to the unavoidable influence of return flows induced by the free-slip boundaries and an order of magnitude difference in flow-dependent effective viscosity. If the lithosphere plates are allowed to move away from the boundary, which we implemented to relax the free-slip condition on the motion of the plates, upward return flows at either boundary have an important adverse effect on subduction evolution, by forcing additional convergence, and model evolution in general. These effects could not be sufficiently reduced by taking a larger 6:1 aspect ratio (simulating the half-size of modern oceans), whereas for open boundaries it was found that the flow pattern and subduction evolution was basically independent of the aspect ratio. Also for closed sidewalls a general drop in flow speed was observed for larger aspect ratio models. However, the free-slip boundaries prevented application of a useful scaling procedure. While the width of the model domain was varied we kept the depth of the model constant. In our rollback models, the slab is draping on the 660-boundary as a result of increasing viscosity in combination with a decrease in negative buoyancy resulting from the 660 km phase transition. In this model scenario, the effect of the bottom boundary will not be very strong. For the investigation of slab behavior in the lower mantle a model with much larger depth is required. But, for such models we still expect that the open boundaries would allow using a smaller lateral extent of the domain (2000–3000km) in comparison to free-slip models to reduce the effect of the sidewall boundary conditions.

Although our experiments are in 2-D, we do expect that using open boundaries in 3-D modeling of subduction evolution [Jadamec and Billen, 2010; Piromallo et al., 2006; van Hunen et al., 2011] may proof beneficial. In 3-D, flow patterns have larger degrees of freedom as toroidal flow can be excited, e.g. around slab edges, and perhaps remote free-slip boundaries may suffice, but as no material is allowed to leave or enter the model unfavourable effects of free-slip sidewalls cannot be excluded.

Open boundary flow, if any, is restricted to be perpendicular to the sidewall. This condition, as any type of boundary condition, poses constraints on the internal flow. But the advantage we experience from using open boundaries is that we can deal with lateral in- and outflow of the lithosphere in a more general way (in 2-D and current 3-D models), e.g. by prescribing intraplate stress, or even just by imposing kinematic constraints on the side walls, while lateral flow below the lithosphere can fully develop, in the sense that it is not

influenced by (possibly remote) impermeable vertical boundaries.
Other advantages are the independence of the aspect ratio of the model domain, which allows for smaller models with increased resolution for modeling detail. An approximate scaling procedure can be used to tune the overall flow speed amplitude to levels consistent with the mantle outside the model domain as far as buoyancy inside the model would drive motions outside the model.

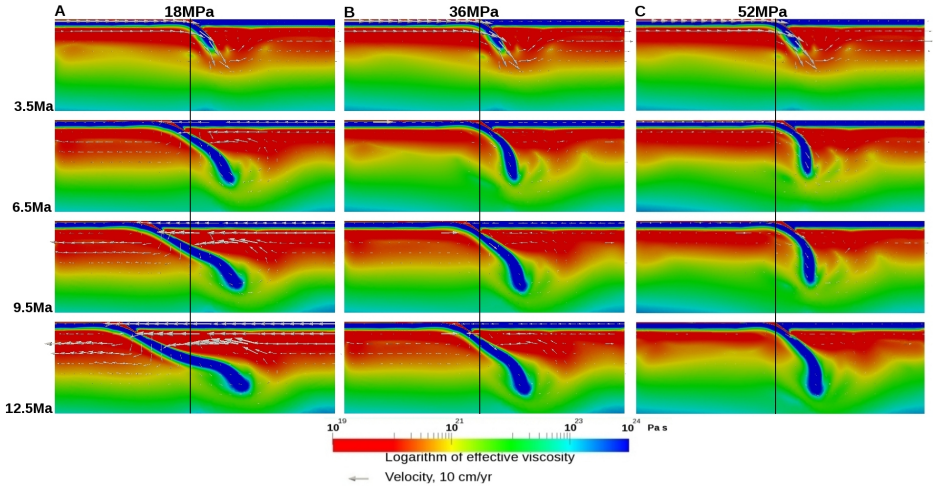

Figure 3.10. The evolution of the models with open boundary conditions with different intraplate stress values on the overriding plate: (A) model with intraplate stress 18 MPa; (B) model with intraplate stress 36 MPa; (C) model with intraplate stress 52 MPa. Vertical black lines represent the initial trench position.

Appendix A
Scaling of the velocity for models with contrasting aspect ratios

We have shown that for models with open boundaries, the convective flow pattern is unaffected by the aspect ratio of the domain. However, due to the fact that the amount of viscous dissipation in the model interior decreases with decreasing aspect ratio, we observe an increase in the magnitude of the flow velocity with decreasing aspect ratio of the model. We present an iterative method that allows us to scale the velocity of the small aspect ratio domain

such that it is in agreement with larger aspect ratio models.

Figure A1 shows a snapshot of the dissipated power distribution:

$$\Phi = \frac{1}{2}\dot{\varepsilon}_{ij}\tau_{ij} \quad \text{(A1)}$$

where, $\dot{\varepsilon}_{ij} = \partial_i u_j + \partial_j u_i$ and $\tau_{ij} = \eta\dot{\varepsilon}_{ij}$. This figure illustrates that the dissipative power is concentrated within the slab and its surrounding in the central region of the domain. Other areas of significant dissipative power are located in the asthenosphere directly below the lithospheric plates towards the left and right hand boundary of the domain. The asthenospheric contribution to the dissipative power scales with the width of the domain.

Based on this configuration of the dissipative power, we have applied an approximate scheme to scale the velocity for the effect of power dissipated in a virtual lateral extension of the domain, schematically illustrated in Figure A2.

This way a uniform velocity scale factor is determined iteratively in the following steps:

1. Compute the volume integrated dissipative power for the interior domain labeled model 1 in Figure A2,

$$P_{in}^{j} = \int_{V_{in}} \Phi^{(j)} dV, \quad \text{(A2)}$$

where j is the iteration number,

2. Estimate the corresponding power, dissipated in the virtual extensions of the model, the regions labeled 1 and 2 in Figure A2,

$$P_{out}^{j} = \int_{V_{out}} \Phi^{(j)} dV, \quad \text{(A3)}$$

This is done by uniform lateral extrapolation of the dissipation function profiles at the left and right hand side boundaries of the interior domain.

3. A velocity scaling factor is defined as

$$f_j = \frac{(P_{out}^{(j)} + P_{in}^{(j)})}{P_{in}^{(1)}} \quad \text{(A4)}$$

4. Apply the scaling factor to the velocity field,

$$U^{(j+1)} = f_j U^{(j)}. \quad \text{(A5)}$$

This procedure is repeated until convergence $|f_{j+1} - f_j| \leq 10^{-6}$, which is typically obtained within a few iterations. Despite of the fact that the values for the dissipation in the external regions represent less than 15–20% of the total dissipation in the model, this iterative procedure leads to a significant reduction in the velocity field magnitude, due to the non-linear rheology.

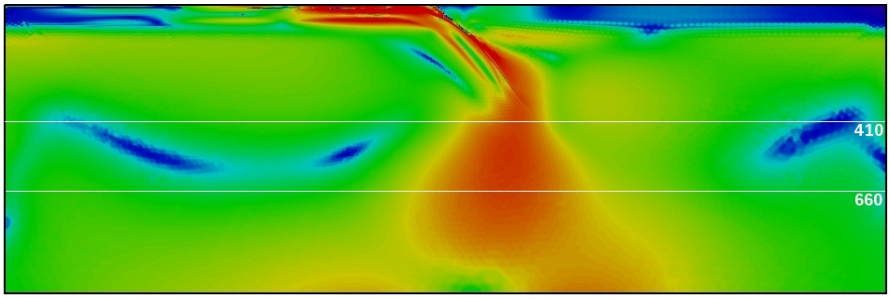

Figure A1. Energy dissipation for the model with open boundaries and aspect ratio 3:1 at time = 3.5My.

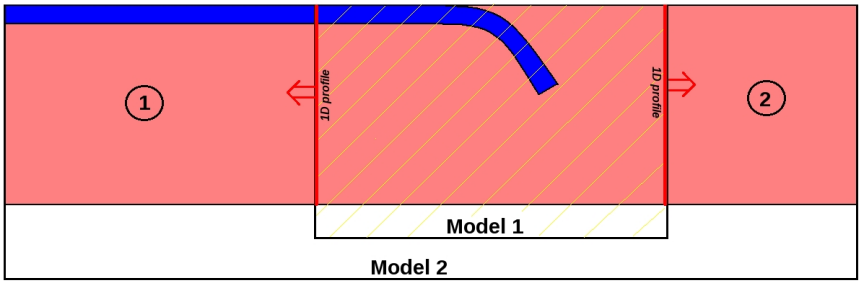

Figure A2. Schematic representation of the subduction model. See text for the explanation.

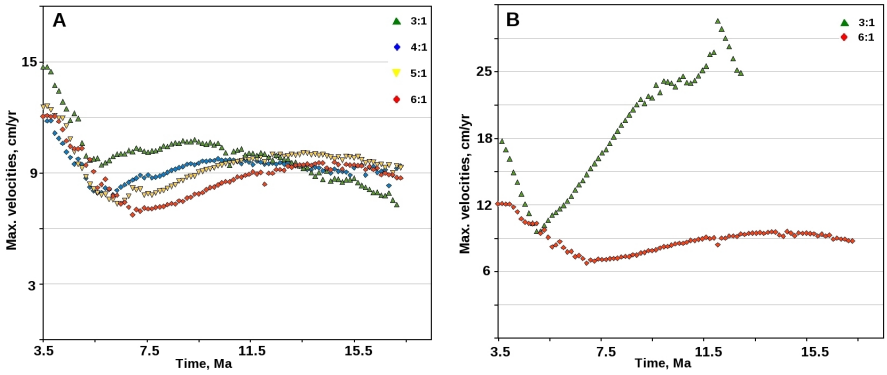

Figure A3. (A) Maximum velocities for model with aspect ratio 6:1, and scaled maximum velocities for models with 3:1, 4:1 and 5:1 aspect ratios. (B) Comparison of maximum velocities for two models without applying the velocity scaling procedure.

The above-mentioned procedure was tested on several models with different aspect ratios. The results of the velocity scaling for these models are shown in Figure A3.

The results of the velocity scaling for these models are shown in Figure A3a where maximum velocity values in the domain for the model with aspect ratio 6 and scaled models with smaller aspect ratios are presented. The maximum velocities are typically observed in the asthenosphere below the overriding plate. The maximum evolution time is 18 My since, for the model with the smallest aspect ratio; the trench has reached the left boundary at this stage. The time-averaged difference in maximum velocities is ~6% for the 4:1 and 5:1 model and 14% for 3:1. The maximum difference in velocity magnitude is, 20% for the 5:1 model 30% for the 4:1 model and 45% for the 3:1 model. Without velocity scaling the difference in maximum velocities between 3:1 and 6:1 aspect ratio models after 12 My of evolution reaches approximately 70% and increases over time as illustrated in Figure A3b.

References

1. Babeyko, A. Y. and S.V. Sobolev (2008), High-resolution numerical modeling of stress distribution in visco-elasto-plastic subducting slabs. Lithos, 103, 205–216.
2. Baes, M., R. Govers, and R. Wortel (2011), Subduction initiation along the inherited weakness zone at the edge of a slab: Insights from numerical models. Geophys. J. Int., 184, 991–1008.
3. Behounkova, M. and H. Cizkova (2010), Long-wavelength character of subducted slabs in the lower mantle. Earth Planet. Sci. Lett., 275, 43–53.
4. Billen, M. I. and M. Gurnis (2003), Comparison of dynamic flow models for the Central Aleutian and Tonga-Kermadec subduction zones. Geochem. Geophys., 4, 17 pp., doi:10.1029/2001GC0002952003.
5. Billen, M. I. (2010), Slab dynamics in the transition zone. Physics of the Earth and planetary interiors, 25, 297–356.
6. Burgmann, R. and G. Dresen (2008), Rheology of the lower crust and upper mantle: evidence from rock mechanics, geodesy and field observations. Annu. Rev. Earth Planet. Sci., 36, 531–536.
7. Capitanio, F. A., D. R. Stegman, L.N. Moresi, and W. Sharples (2010), Upper plate controls on deep subduction, trench migration and deformations at convergent margins. Tectonophys., 483, 80–92.

8. Cizkova, H., A.P. van den Berg, W. Spakman, and C. Matyska (2012), The viscosity of Earth's lower mantle inferred from sinking speed of subducted lithosphere. Phys. Earth Planet. Int., 200–201, 56–62.
9. Cizkova, H., J. van Hunen, and A.P. van den Berg (2007), Stress distribution within subducting slabs and their deformation in the transition zone. Phys. Earth Planet. Int., 161, 202–214.
10. Cristensen, U. R. and D. A. Yuen (1985), Layered convection induced by phase transition. J. Geophys. Res., 99, 10291–10300.
11. Duretz, T., T. V. Gerya, and D.A. May (2011), Numerical modelling of spontaneous slab breakoff and subsequent topographic response. Tectonophysics, 502, 244–256.
12. Duretz, T., T. V. Gerya, B. J. P. Kaus, and T.B. Andersen (2012), Thermo-mechanical modeling of slab eduction. J. Geophys. Res., 117, doi:10.1029/2012JB009137.
13. Enns, A., T. W. Becker, and H. Schmeling (2005), The dynamics of subduction and trench migration for viscosity stratification. Geophys. J. Int., 160, 761–775.
14. Funiciello, F., C. Faccenna, D. Giardini, and K. Regenauer-Lieb (2003), Dynamics of retreating slabs: Insights from three dimensional laboratory experiments. J. Geophys. Res., 108, 16 pp., doi:10.1029/2001JB000896.
15. Funiciello, F., C. Faccenna, A. Heuret, S. Lallemand, E. Di. Giuseppe, and T.W. Becker (2008), Trench migration, net rotation and slab-mantle coupling. Earth Planet. Sci. Lett., 271, 233–240.
16. Gerya, T. (2011), Future directions in subduction modeling. J. Geodynam., 52, 344378.
17. Han, L. and M. Gurnis (1999), How valid are dynamic models of subduction and convection when plate motion are prescribed? Phys. Earth Planet. Int., 110, 235–246.
18. Jadamec, M. A. and M.I. Billen (2010), Reconciling surface plate motions with rapid three-dimensional mantle flow around a slab edge. Nat. Lett., 465, 338–342.
19. Jadamec, M. A. and M.I. Billen (2012), The role of rheology and slab shape on rapid mantle flow: Three-dimensional numerical models of the Alaska slab edge. J. Geophys. Res., 117, 20 pp., doi:10.1029/2011JB008563.
20. Karato, S., D. Rubie, and S. Hong Yan (1993), Dislocation recovery in olivine under deep upper mantle conditions: implication for creep and diffusion. J.

Geophy. Res., 98, 9761–9768.

21. Karato, S., M. Riedel, and D.A. Yuen (2001), Rheological structure and deformation of subducted slabs in mantle transition zone: implications for mantle circulation and deep earthquakes. Phys. Earth Planet. Int., 127, 83–108.
22. Kaufmann, G. and K. Lambek (2000), Mantle dynamics, postglacial rebound and the radial viscosity profile. Phys. Earth Planet. Int., 121, 301–324.
23. Lithgow-Bertelloni, C. and J.H. Guynn (2004), Origin of the lithospheric stress field. J. Geophys. Res., 109, 32 pp., doi:10.1029/2003JB002467.
24. Manea, V. and M. Gurnis (2007), Subduction zone evolution and low-viscosity wedges and channels. Earth Planet. Sci. Lett., 264, 22– 45.
25. OzBench, M., K. Regenauer-Lieb, D. Stegman, G. Morra, R. Farrington, A. Hale, D.A. May, J. Freeman, L. Bourgouin, H. Muhlhaus, and L. Moresi (2008), A model comparison study of large-scale mantle-lithosphere dynamics driven by subduction. Phys. Earth Planet. Int., 171, 224–234.
26. Piromallo, C., T.W. Becker, F. Funiciello, and C. Faccenna (2006), Three-dimensional instantaneous mantle flow induced by subduction. Geophys. Res. Lett., 33, 4 pp., doi:10.1029/2005GL025390.
27. Quinquis, M., S. Buiter, and S. Ellis (2011), The role of boundary conditions in numerical models of subduction zone dynamics. Tectonophys., 497, 57–70.
28. Quinteros, J., S. V. Sobolev, and A. A. Popov (2010), Viscosity in transition zone and lower mantle: Implication for slab penetration. Geophys. Res. Lett., 37, 5 pp., doi:10.1029/2010GL043140.
29. Schellart, W. P., J. Freeman, D. R. Stegman, L. Moresi, and D. May (2007), Evolution and diversity of subduction zones controlled by slab width. Nature, 446, 308–311.
30. Schellart, W. P., D. R. Stegman, and J. Freeman (2008), Global trench migration velocities and slab migration induced upper mantle volume fluxes: Constraints to find an Earth reference frame based on minimizing viscous dissipation, Earth Sci. Rev., 88, 118–144.
31. Schmeling, H., A. Babeyko, A. Enns, C. Faccenna, F. Funiciello, T. Gerya, G. Golabek, S. Grigull, B. Kaus, G. Morra, S.M. Schmalholz, and J. van Hunen (2008) A benchmark comparison of spontaneous subduction models-towards a free surface. Phys. Earth Planet. Int., 171, 198–223.
32. Simmons, N. A., A. M. Forte, and S. P. Grand (2006), Constraining mantle flow with seismic and geodynamic data: a joint approach. Earth Planet. Sci.

Lett., 246, 109–124.
33. Stegman, D. R., W. P. Schellart, and J. Freeman (2010), Competing influence of plate width and far-field boundary conditions on trench migration and morphology of subducted slabs in the upper mantle. Tectonophys., 483, 46–57.
34. Turcotte, D. L. and G. Schubert (2002), Geodynamics. Cambridge University Press.
35. Ueda, K., T. V. Gerya, and J.-P. C. Burg (2012), Delamination in collisional orogens: thermo-mechanical modeling. J. Geophys. Res., 117, 25 pp., B08411, doi:10.1029/2012JB009144.
36. van den Berg, A. P., D. Yuen, and P. E. van Keken (1991), Effect of depth variations in creep laws on the formation of plates in mantle dynamics. Geophys. Res. Lett., 18, 2197–2200.
37. van Dinther, Y., G. Morra, F. Funiciello, and C. Faccenna (2010), Role of the overriding plate in the subduction process: insights from numerical models. Tectonophys., 484, 74–86.
38. van Hunen, J. (2001), Shallow and buoyant lithospheric subduction: causes and implications from thermo-chemical numerical modeling. PhD thesis, Utrecht University, Utrecht.
39. van Hunen, J., A. P. van den Berg, and N. J. Vlaar (2000), A thermo-mechanical model of horizontal subduction below an overriding plate. Earth Planet. Sci. Lett., 182, 157–169.
40. van Hunen, J. and M. B. Allen (2011), Continental collision and slab break-off: A comparison of 3-D numerical models with observations. Earth Planet. Sci. Lett., 302, 27–37.

Chapter 4

Underpinning tectonic reconstructions of the western Mediterranean region with dynamic slab evolution from 3D numerical modeling*

Abstract

No consensus exists on the tectonic evolution of the western Mediterranean since ~35 Ma. Three disparate tectonic evolution scenarios are identified, each portraying slab rollback as the driving mechanism but with rollback starting from strongly different subduction geometries. As a critical test for the validity of each tectonic scenario we employ thermo-mechanical modeling of the 3-D subduction evolution. From each tectonic scenario we configure an initial condition for numerical modeling that mimics the perceived subduction geometry at ~35 Ma. We seek to optimize the fit between observed and predicted slab morphology by varying the nonlinear viscoplastic rheology for mantle, slab, and continental margins. From a wide range of experiments we conclude that a tectonic scenario that starts from NW-dipping subduction confined to the Balearic margin at ~35 Ma is successful in predicting present-day slab morphology. The other two scenarios (initial subduction from Gibraltar to the Baleares, and initial subduction under the African margin) lead to mantle structure much different from what is tomographically imaged. The preferred model predicts slab rotation by more than 180°, east-west lithosphere tearing along the north African margin, and a resulting steep east-dipping slab under the Gibraltar Strait. The preferred subduction model also meets the first order temporal constraints corresponding to Mid-Miocene (~16 Ma) thrusting of the Kabylides onto the African margin and nearly stalled subduction under the Rif-Gibraltar-Betic arc since the Tortonian (~8 Ma). Our modeling also provides constraints on the rheological properties of the mantle

* This chapter has been published as: Chertova, M.V., W. Spakman, T. Geenen, A. van den Berg, and D.J.J. van Hinsbergen (2014), Underpinning tectonic reconstructions of the western Mediterranean region with dynamic slab evolution from 3-D numerical modeling. JGR, vol. 119.

and slab, and of continental margins in the region.

4.1 Introduction

For the western Mediterranean region (Figure 4.1) distinctly different tectonic reconstructions exist for the past ~35 My, which all appear to be based on broadly similar geological and plate kinematic constraints [e.g. Rosenbaum et al., 2002; Faccenna et al., 2001; 2004; Jolivet et al., 2009; Schettino and Turco, 2006; Handy et al., 2010; Carminati et al., 2012; Verges and Fernandez, 2012; van Hinsbergen et al., 2014]. Despite the large consensus that subduction rollback since ~35 Ma is regarded as the geodynamic process driving tectonic change, there is significant disagreement on its spatial-temporal evolution and how this couples to tectonic evolution. Rollback is either portrayed as originating from a long N-NW dipping subduction zone stretching from Gibraltar in the W to the Baleares in the NE [e.g. Dercourt et al., 1986, Faccenna et al., 2004; Schettino and Turco, 2006; Handy et al., 2010; Carminati et al., 2012], or from a laterally restricted NW dipping slab confined to the Baleares margin [e.g. Rosenbaum et al., 2002; Spakman and Wortel, 2004; Frizon de Lamotte et al., 2009; van Hinsbergen et al., 2014], or from a SE dipping subduction under the north-African margin [Verges and Fernandez, 2012] (Figure 4.2). These three disparate tectonic evolution scenarios illustrate the current lack of convergence towards a single tectonic evolution model for the western Mediterranean.

Although collecting more geological and geophysical data may perhaps provide a resolution, we followed the, as yet, unexplored avenue of designing and applying quantitative tests for the various proposed geodynamic rollback hypotheses. The most crucial test is whether 35 My of subduction evolution, as qualitatively portrayed in each tectonic reconstruction, can predict the position and 3-D morphology of tomographically imaged slabs in the upper mantle of the region. To investigate this we employed 3-D thermo-mechanical subduction modeling starting from an initial configuration defined from each tectonic reconstruction. In this “forward” approach we experimented with different initial settings for the rheology of the mantle, lithosphere and continental margins and their geometry as a strategy to optimize the fit between predicted and observed slab position and morphology.

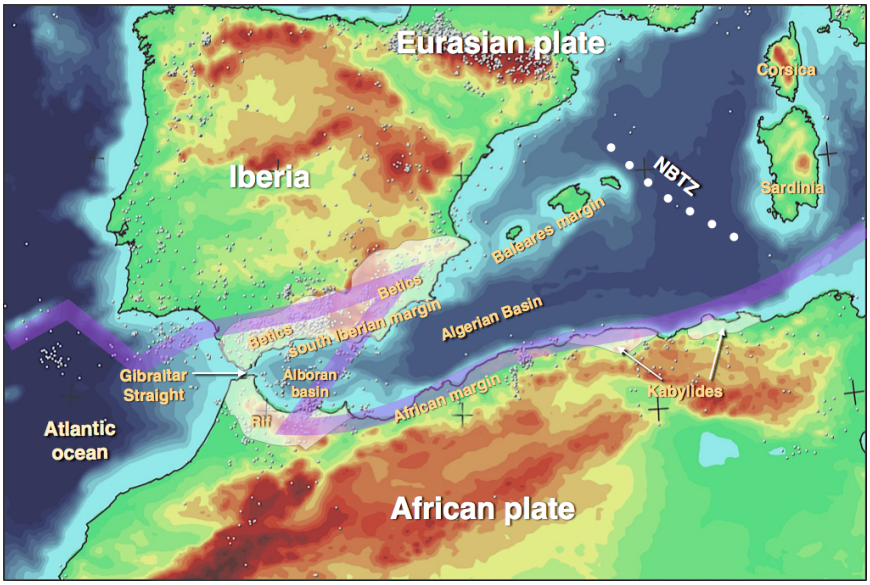

Figure 4.1. Map of the westernmost Mediterranean region with the main geographic names and some tectonic features used in the paper. NBTZ- North Balearic Transform Fault zone. The transparent purple line depicts the diffuse plate boundary between the African and Eurasian plate in the region (after Gutscher 2012).

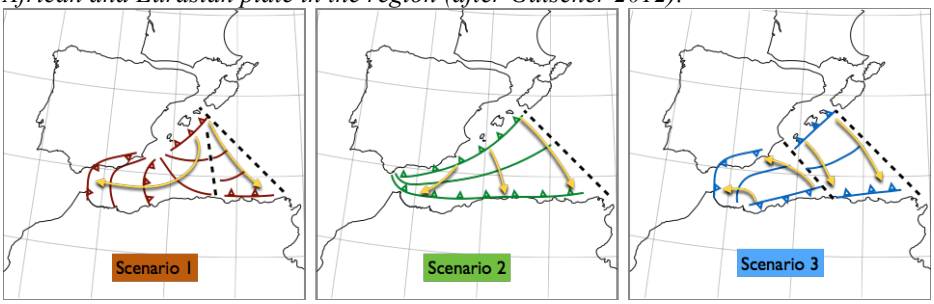

Figure 4.2. An illustration of rollback as portrayed in the three different reconstruction scenarios shown in the paleogeography at ~35Ma [van Hinsbergen et al., 2014]: Scenario 1 starts from an initial short subduction zone near the Baleares [e.g. Rosenbaum et al. 2002; Spakman and Wortel 2004; van Hinsbergen et al. 2014]; Scenario 2 involves a long initial trench along the entire Gibraltar-Baleares margin [e.g. Gueguen et al. 1998; Faccenna et al. 2004; Jolivet et al. 2006]; and Scenario 3 starts from a S-SE dipping initial subduction zone under African margin [Verges and Fernandez 2012]. Dashed lines represent proposed transform fault regions. The triangular zone between the transform zones of Scenario 1 depicts the lithosphere that rolls back toward the east Kabylides [Spakman and Wortel, 2004]. Not displayed is the more eastern subduction system leading to rollback to the E-SE involving the Apennines-Calabria subduction system [e.g. Faccenna et al. 2004; Spakman and Wortel 2004]. Paleogeography at 35Ma from van Hinsbergen et al. [2014]

This is different from "inverse" approaches in which the tomographic model is input to reconstruct the initial condition, i.e. the past [e.g. Liu and Gurnis, 2008; Ismail-Zadeh et al., 2012; Spasojevic et al., 2009]. Here we specifically conformed to the 3-D geometry of the subduction zone at ~35 Ma as portrayed in, or derived from, a tectonic reconstruction to define the initial condition for 3-D modeling, and next predict the future. Our results show a strong difference in subduction evolution between the different tectonic reconstructions and a strong dependence on assumed rheology. However, a suite of different experiments, in which also initial conditions are varied within the limits posed by a particular reconstruction, led to a clear and positive outcome.

The generic research aim we pursue here is to make a significant step forward from kinematics-based tectonic reconstructions toward dynamics-based reconstructions in which the role of deep driving processes that underpin regional tectonic evolution is quantitatively assessed and incorporated. The initial step we make is quantitative testing, through 3-D numerical modeling, of the qualitative concepts of the driving geodynamic processes that have been proposed to underpin the kinematic reconstruction of tectonic evolution. This proves to be a very powerful strategy for constraining the tectonic evolution of the western Mediterranean.

4.2 Modern mantle structure from seismic tomography: the Rif-Gibraltar-Betic (RGB) slab

Early tomographic observation of a positive seismic velocity anomaly across the upper mantle of the western Mediterranean region led to the first interpretations of deep subduction [Spakman, 1986; Blanco and Spakman, 1992]. Since the late 90's, improved tomographic models all exhibit a volume with positive P-wave speed anomalies, which extends from under the Rif-Gibraltar region curving to the NE and E to under the eastern Betics (Figure 4.3)[Bijwaard et al., 1998; Calvert et al., 2000; Gutscher et al., 2002; Piromallo and Morelli, 2003; Spakman and Wortel, 2004; Bezada et al., 2013; Palomeras et al., 2014]. A breakthrough interpretation was made by Gutscher et al. [2002] who explained marine geophysical observations of an active forearc west of the Gibraltar Straight with the existence of a continuous east-dipping slab.

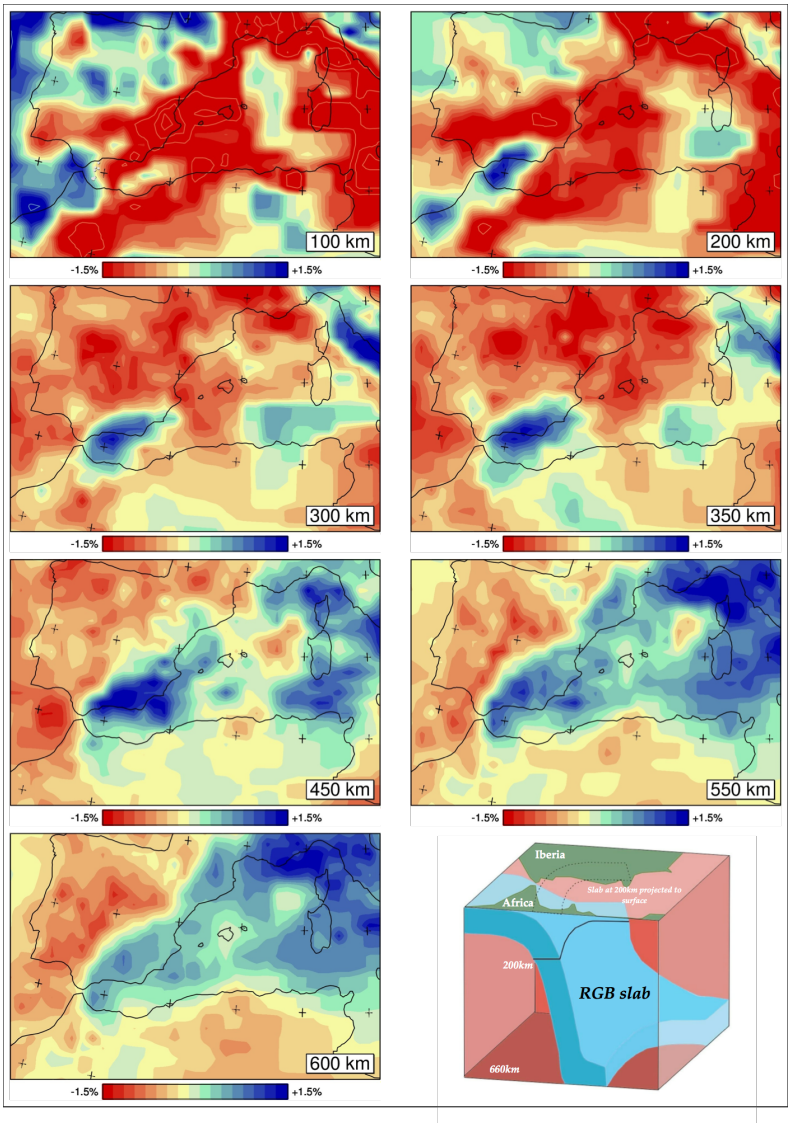

Figure 4.3. Mantle structure of the Western-Mediterranean region from the tomography model UU-P07 (Amaru, 2007). Shown are P-wave seismic velocity anomalies relative to the 1-D reference model ak135 of Kennett et al. 1995. The blue anomaly under the Rif, Gibraltar Straight and Betics (southern Iberia) is the blurred image of the Rif-Gibraltar-Betic (RGB) slab. The spatial resolution is presented in van Hinsbergen et al. (2014). The first order slab structure is similar to that obtained by Bezada et al. (2013) from tomographic analysis of an independent regional data set. A cartoon interpretation of the RGB-slab following Spakman and Wortel (2004) is presented to the lower right.

We refer to Gutscher [2012] for an extensive review on present-day subduction under the Gibraltar Strait and for the evidence of the predominantly oceanic nature of the subducted lithosphere. Spakman and Wortel [2004] analyzed the 3-D morphology of this subducted lithosphere, which we name here the Rif-Gibraltar-Betic (**RGB**) slab to emphasize its lateral extent (Figure 4.3).

The slab image displayed in Figure 4.3 is from the model of Amaru [2007] and is of comparable morphology but of higher amplitude compared to the anomaly in the model of Bijwaard and Spakman [2000], which was used by Gutscher et al. [2002] and Spakman and Wortel [2004]. Bezada et al. [2013] recently obtained a similar tomographic image of the RGB slab from a regional tomographic analysis of a new teleseismic data set observed with a dense regional station network. Figure 4.3 presents the target slab morphology of which we attempt to reproduce first order features by numerical simulation of the RGB-slab evolution.

The robust features from independent tomographic studies are the steeply east-dipping slab under the Gibraltar Strait and Alboran basin, and a slab morphology that extends from under the NW Rif towards the north and next curving eastward under the Betics. Most of the anomaly is found under south Iberia while in the transition zone the anomaly may also partly lie under the Algerian basin. Furthermore, under the northwest African margin no evidence is found for subducted lithosphere, either attached or detached [Spakman and Wortel, 2004; Bezada et al., 2013; van Hinsbergen et al., 2014 and spatial resolution estimates presented in these papers], whereas a detached slab is imaged below the Kabylides in northeast Algeria [Spakman and Wortel, 2004; van Hinsbergen et al., 2014]. The recent surface wave tomography model of Palomeras et al. [2014] corroborates the slab detachment geometry imaged under the eastern Betics (Figure 4.3)[Spakman and Wortel, 2004; Bezada et al., 2013] and in addition proposes slab continuous with the Moroccan Rif lithosphere and also slab partly attached to Iberian lithosphere under the central Betics.

4.3 Tectonic reconstructions of the western Mediterranean region

We categorize published tectonic reconstructions into three evolution scenarios of the western Mediterranean, which we briefly introduce here in the same order as we use them for our numerical experiments. Our focus is on how subduction evolution is portrayed in these scenarios from the start of rollback at ~35 Ma and not on the geological evidence and interpretations underlying the construction of these tectonic models.

The first reconstruction scenario (**S1**) proposes that subduction in the western Mediterranean started from a NE-SW striking trench located southeast of the Balearic islands leading, after initial southward rollback, to a dominant phase of westward rollback of the RGB slab [e.g., Royden, 1993; Lonergan and White, 1997; Rosenbaum et al., 2002; Spakman and Wortel, 2004; van Hinsbergen et al., 2014]. Here we follow the analysis of Spakman and Wortel [2004] and van Hinsbergen et al. [2014] who qualitatively reconciled tectonic evolution with subduction evolution and present-day slab morphology. The initial trench was ~300 km wide measured from the North Balearic Transform Fault (NBTZ) to the southwest. Plate convergence between Africa and southern Iberia in these models is deemed insufficient to form a subduction zone, and was accommodated by thrusting and Iberian margin thickening. The basic concept of trench evolution as a result of rollback is sketched in Figure 4.2, Scenario 1. The proposed direction of initial rollback is southward during the first 5-10 My. This is followed by rapid Early Miocene radially outgrowing rollback to the W, S and SE. S-SE rollback of the eastern part of the slab culminates in Mid Miocene thrusting of the Kabylides fold-thrust belt over the African margin in Algeria. Here, the slab splits into two parts. The western part of the subduction zone, rotated ~100° clockwise by then into a N-S position, rolls back toward Gibraltar in the west and the south Iberian margin in the northwest. The eastern part of the slab, which underlies the eastern part of the Kabylides (Figure 4.1), detaches and is tomographically detected in the upper mantle below the African margin of northeast Algeria (Figure 4.3) [Spakman and Wortel, 2004; van Hinsbergen et al., 2014]. Our focus here is on the western part of the subduction system that at this stage was extending from the central Algerian margin to the Baleares margin. Its southern part rolled back rapidly in westward direction toward Gibraltar since middle Miocene time accommodated by lithosphere tearing creating a STEP

fault [Govers and Wortel, 2005] parallel to the north African margin, which results in opening the Algerian basin by >500 km of E-W extension [Mauffret et al., 2004]. The northern part of the slab rolled back with a slower rate, likely because it subducted the southern continental margin of Iberia instead of oceanic lithosphere. This led to an additional ~80° clockwise rotation of the northern segment, culminating in an E-W, southward dipping orientation of the slab below the south Iberian margin. In all reconstructions, the slab arrives near its modern position in the Tortonian complying with the geological evidence coming from uppermost Tortonian and Messinian sediments unconformably covering the Gibraltar trench, both onshore and offshore [Crespo-Blanc and Campos, 2001; Melialdea et al., 2004; Chalouan et al., 2006; Iribarren et al., 2007; Ammar et al., 2007].

The second reconstruction scenario (**S2**) assumes that already in the Early Oligocene an initial subduction zone of long lateral extent existed from the Baleares margin to Gibraltar (Figure 4.2, Scenario 2). This has been a leading concept for more than two decades [e.g. Dercourt et al. 1986; Gueguen et al., 1998; Wortel and Spakman, 2000; Faccenna et al., 2004; Jolivet et al., 2000, 2009; Schettino and Turco, 2006; Handy et al., 2010; Billi et al., 2011; Carminati et al., 2012]. Particularly, Faccenna et al. [2004] coupled the tectonic evolution of the Western Mediterranean to present-day mantle structure as imaged by Piromallo and Morelli [2003]. In this reconstruction, the subduction process was already developed at ~35 Ma with a slab length of up to ~400 km length. This maximum estimate resulted from the difference between tomographically observed slab length and the total amount of plate convergence and tectonic shortening near Gibraltar during the past ~35 My. However, the initial slab might have been shorter (at ~35 Ma) if the subducted lithosphere was weak enough to significantly stretch during subduction rollback since 35 Ma [Faccenna et al., 2004]. Oligocene to Middle Miocene rollback was largely southward leading to the opening of the Algerian basin in a predominant N-S direction toward Africa (Figure 4.2, Scenario 2) and thrusting of the Kabylides onto the African margin in the Middle Miocene. A subsequent rapid clockwise trench rotation towards present-day Gibraltar was accommodated along the Rif margin, followed by ~200 km of E-W extension of the Alboran domain.

The recent reconstruction model of Verges and Fernandez [2012] constitutes our third scenario **S3**. In contrast to initial subduction under the European

(Iberian-Baleares) margin, as in scenarios S1 and S2, an initial Early-Middle Cenozoic subduction zone is proposed that dipped southward below the North African margin. It is tectonically broadly similar to the westward rollback phase of scenario **S1** in that it invokes large-scale northwestward and westward rollback of the RGB-slab accommodated by E-W opening of the Algerian basin (Figure 4.2, Scenario 3). This initially south dipping subduction zone was of 400-500 km lateral extent, situated under the western Algerian margin, and was connected in the east through a transform to a north (west) dipping subduction zone below the eastern Baleares from which the Kabylides were derived (Figure 4.2, Scenario 3). In this reconstruction, subduction evolves slowly during the Eocene and has produced a slab length of ~300 km in the Early Oligocene [Verges and Fernandez, 2012].

4.4 4-D thermo-mechanical modeling of subduction evolution

Each of the above reconstruction scenarios are used to define various starting configurations of subduction at ~35 Ma (section 4.3) from which our numerical models of slab evolution will evolve in a dynamic self-consistent way. The experiments aim to test if one, or more, of these starting slab geometries at the inception of rollback would lead to a prediction of the modern mantle structure as imaged by seismic tomography (Figure 4.3), i.e. after modeling of 35 My of subduction evolution. To this end, we first introduce the 3-D model geometry and the governing transport equations and rheology, after which we explain in more detail our modeling approach of determining the initial condition at ~35 Ma for each reconstruction in terms of temperature field, rheology, and buoyancy.

4.4.1 Model geometry and boundary conditions

We adopt a regional Cartesian model volume for the western Mediterranean as illustrated in Figure 4.4. The dimensions of the model box are 1650×1300×1000 km. The top boundary is free-slip and the bottom is no slip. To allow for slab decoupling from the top surface, a weak crustal layer is emplaced on top of the oceanic lithosphere following Chertova et al. [2012]. The side boundaries are open for lateral in- and outflow [Chertova et al.,

2012], except for the top 150 km of the southern and northern parts of the domain at which kinematic boundary conditions of plate motion will be implemented. Open-side boundaries affect the flow field pattern inside the domain to a much lesser extent than closed, free-slip boundaries [Chertova et al., 2012]. This allows to significantly decrease domain dimensions in favor of shorter overall computation time per modeling experiment.

At the top 150 km of the southern and northern sidewalls of the domain, velocity boundary conditions are imposed simulating the relative and absolute plate motions of the African and Iberian (Eurasian) plates. Relative plate motions were taken from the reconstruction of van Hinsbergen et al. [2014], which is embedded in the Eurasia-North America-Africa plate circuit of Torsvik et al. [2012], and incorporate the recent Iberia-Eurasia reconstruction of Vissers and Meijer [2012]. The relative plate motions are placed in the global moving hotspot reference frame of Doubrovine et al. [2012] to constrain plate motions relative to the mantle. Considering that the temporal details of this motion are uncertain [Doubrovine et al., 2012], we adopt the average plate velocity of past 35 My as kinematic boundary conditions for our modeling on the southern domain edge in northwest Africa and on the northern edge in northern Iberia. In our models Africa is moving in an almost northern direction (N9°E) with a speed of 8.6 mm/yr and Iberia is moving in a northeast direction (N58°E) with a speed of 4.6 mm/yr. The paleogeography of the region at ~35 Ma defines the division of the model into continental and oceanic domains and is taken from the tectonic reconstruction of van Hinsbergen et al. [2014].

In general, the different reconstruction scenarios agree on the paleogeography (relative distances) at about 35 Ma (Figure 4.4). As noted above, these scenarios are predominantly different in initial slab geometry and trench location. Figure 4.4 also shows the subdivision of the lithosphere into oceanic (blue), continental (brown), and continental margin (green) domains. The initial subduction zone geometry for each of the scenarios will be introduced below (Figure 4.5). In our models the difference between oceanic and continental lithosphere is expressed in the thermal structure and rheology in terms of the strength of the lithosphere. We did not assign a different density to continental lithosphere relative to oceanic lithosphere, hence there are no lateral buoyancy contrasts, except the contrast corresponding to the initial subducting slab. To the west from Gibraltar, the transition between continental

lithosphere of Iberia and Africa, and oceanic lithosphere of the Atlantic Ocean is represented as a NS-oriented straight line. This part of the domain was geometrically simplified, as its detailed structure is not of significant influence on the subduction evolution modeled.

The reconstruction of van Hinsbergen et al. [2014] determines that ~140 km of oceanic or transitional lithosphere (here modeled as oceanic) separated the paleo-margins of Africa and Iberia at the longitude of Gibraltar at ~35 Ma. To the east, the Alpine-Tethys lithosphere has a north-south extent of up to ~440 km between Baleares and African margin at the longitude of the NBTZ. The width of continental margins is prescribed as 70 km except for the north Moroccan margin, where we allow for wider margin of ~110 km [van Hinsbergen et al., 2014; Verges and Fernandez, 2012].

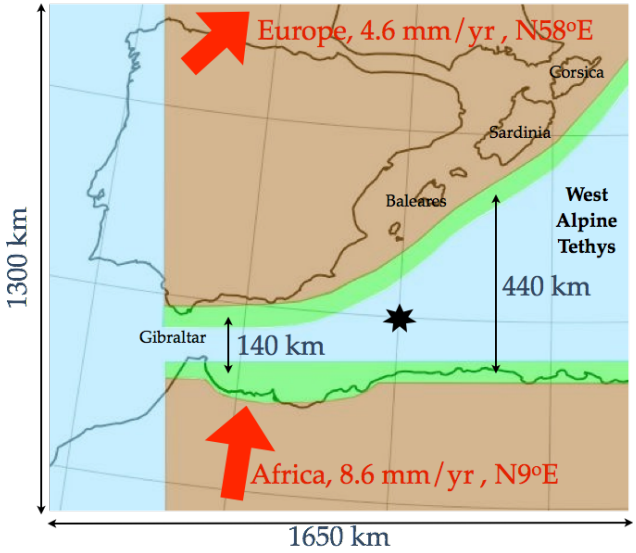

Figure 4.4. The top view of the modeled region showing the paleogeography at ~35 Ma (after van Hinsbergen et al. 2014). Brown regions are modeled as continental lithosphere, blue regions as oceanic lithosphere and green regions denote continental margins. Location of active or incipient subduction at ~35 Ma will be indicated in Figure 4.6. The arrows denote the average absolute plate motion of Iberia and Africa over the past 35My determined from Doubrovine et al. (2012). From the reconstruction of van Hinsbergen et al. (2014) we estimate about 140 km of oceanic or transitional lithosphere between Iberia and Africa, and about 440 km between African and the Balearic margin. The average width of continental margins is 70 km. The star shows the position of vertical viscosity profiles in Figure 4.6.

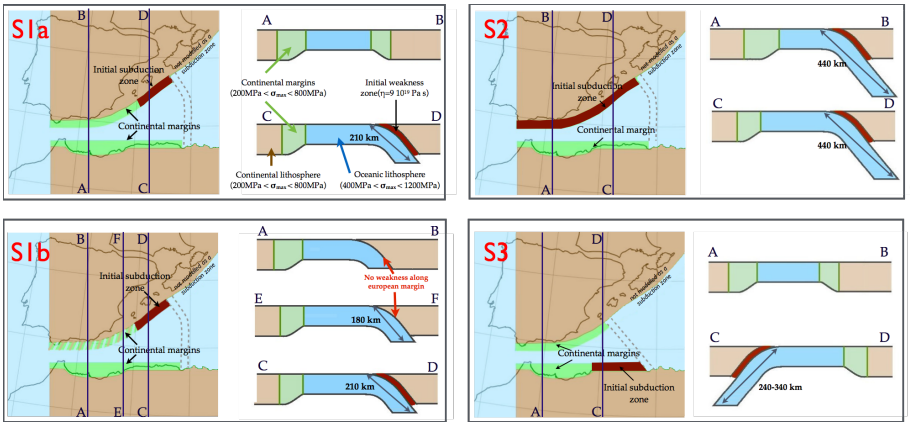

Figure 4.5. Geometry defining the initial conditions for models with subduction starting under the Balearic margin (S1a, S1b), under the whole Iberian-Baleares margin (S2) and under the African margin (S3). The meaning of the colors is as in Figure 4.4. The fat red lines indicate the initial subduction zone. Vertical cross-sections correspond to the NS-lines in the map. The cross-sections show the implemented structure of the African and Iberian-Balearic margins for each of the initial models. Dashed lines in the maps depict the transform/decoupling zone represented by weak young lithosphere. For initial configuration S1b, the south-Iberian margin is hatched to denote initial thickening.

4.4.2 Model equations

We model the evolution of the western Mediterranean region with the finite element modeling package SEPRAN [http://ta.twi.tudelft.nl/sepran/sepran.html]. We solve the following three dimensionless equations (used symbols are given in Table 4.1) applying the extended Boussinesq approximation for a medium including solid-state phase transitions [Cristensen and Yuen, 1984] including:

Mass conservation of an incompressible viscous fluid,

$$\partial_j v_j = 0, \qquad (4.1)$$

the Stokes equation describing force balance,

$$-\partial_i P + \partial_j \tau_{ij} = (RaT - \sum_k Rb_k \Gamma_k) g_i \,, \qquad (4.2)$$

and the heat conservation equation:

$$\frac{\partial T}{\partial t} + v_j \partial_j T - \partial_j \partial_j T - Di(T + T_0) g_i v_i -$$

$$- \sum_k \gamma_k \frac{Rb_k}{Ra} Di(T + T_0) \frac{d\Gamma_k}{dt} = \frac{Di}{Ra} \Phi \,. \qquad (4.3)$$

The size of the tetrahedral finite elements in our models varies from 7 km at the top to 25 km at the bottom of the model. The number of degrees of freedom for most models is around 3 million. For the modeling of subduction evolution in 3D we use parallel computation. The total number of time steps varies between 1500-2200. Material properties such as viscosity of the crustal layer and yield strength are defined on particle tracers that are advected with the flow. Tracers were initially randomly distributed inside the modeling domain.

Our models include the two major phase transitions near 410 km and 660 km depth in the unperturbed mantle. The 410 km phase change contributes to the negative buoyancy force and increases slab pull while the phase change at 660 km has a positive buoyancy effect on cold material resisting slab penetration to the deeper mantle [Christensen and Yuen, 1984]. Values for the Clapeyron slope and density contrasts are given in Table 4.1. Phase transitions are parameterized in the model with the phase-transition function:

$$\Gamma_k = \frac{1}{2}\left[1 + \sin\left(\frac{\pi z_{diff}}{w}\right)\right] \qquad (4.4)$$

where $zdiff = z - ztr - \gamma k \cdot (T - Ttr)$, w is the half-width of k transition zone set to 50 km, ztr and Ttr are the reference depth and temperature of the phase transition, respectively, γk is the Clapeyron slope, T is temperature [Cizkova et al., 2002; van Hunen, 2001].

4.4.3 Rheological model

A composite viscoplastic rheology is used comprising dislocation and diffusion creep and a simplified plasticity in terms of stress limiting the viscosity (Figure 4.6)[Cizkova et al., 2002; van Hunen and Allen, 2011; Gerya et al., 2004; Schott and Schmeling, 1998; Enns et al., 2005; OzBench et al., 2008; Mason et al., 2010; Magni et al., 2012]. The effective viscosity η_{eff} is determined as:

$$\frac{1}{\eta \text{eff}} = \frac{1}{\eta_{diff}} + \frac{1}{\eta_{disl}} + \frac{1}{\eta \text{y}}, \quad (4.5a)$$

where

$$\eta_{diff} = \mu A_{diff}^{-1} (b/d)^{-m} exp[(E_{diff} + PV_{diff})/RT], \quad (4.5b)$$

$$\eta_{disl} = \mu \, \text{A}_{\text{disl}}^{-\frac{1}{\text{n}}} \dot{\varepsilon}^{\frac{1-\text{n}}{\text{n}}} \exp[(\text{E}_{\text{disl}} + \text{PV}_{\text{disl}})/\text{nRT}], \quad (4.5c)$$

$$\eta_y = \frac{\tau_y}{2\dot{\varepsilon}} \quad (4.5d)$$

and

$$\tau_y = \min(\tau_0 + \gamma P, \tau_{max}). \quad (4.5e)$$

In these equations $\dot{\varepsilon}$ is the second invariant of the strain-rate tensor, $A_{diff,disl}$ are diffusion and dislocation creep viscosity prefactors, μ is the shear modulus, γ is the yield stress gradient, b is Burgers vector, d is the grain size, m is the grain size exponent, $V_{diff,disl}$ and $E_{diff,disl}$ are activation volume and activation energy for diffusion and dislocation creep, respectively, P is the lithostatic pressure, T is temperature, τ_0 is the yield stress value at the top surface, τ_{max} is the maximum yield stress value. Parameters for dislocation and diffusion creep are taken for wet olivine (Table 4.1) [Karato et al., 2001]. The first component of τ_y defines the depth dependent strength of the material. If the stress exceeds this value the material gradually becomes weaker. The strength of the material increases with depth until it reaches τ_{max}. Within the slab this strength limitation results in weakening of the slab in the bending zone accommodating subduction and rollback.

In our modeling we experimented with different rheological parameters. The rheology was defined in each experiment by setting values for the activation volume for dislocation and diffusion creep as well as for τ_{max} and μ to define the stress limiting of viscosity.

Symbol	**Meaning**	**Value**	**Dimension**
$\boldsymbol{c_p}$	Specific heat	1250	J $kg^{-1}K^{-1}$
$\boldsymbol{k}$	Thermal conductivity	4.27	W $m^{-1}K^{-1}$
α	Thermal expansivity	3×10^{-5}	K^{-1}
$\boldsymbol{\rho_0}$	Reference density	3413	Kg m^{-3}
$\boldsymbol{Ra}$	Thermal Rayleigh number, $\rho_0 \alpha \Delta T h^3 / \eta_0 \kappa$	1.7×10^6	-

$\boldsymbol{a}\times\boldsymbol{b}\times\boldsymbol{c}$	Dimensions of the model: height, width, length	1×1.65×1.3	1000 km
$\boldsymbol{\eta_0}$	Reference viscosity	10^{21}	Pa s
$\boldsymbol{U_A}$	African velocity, angle	8,6;N9°E	mm yr^{-1}; -
$\boldsymbol{U_E}$	European velocity, angle	4,6;N58°E	mm yr^{-1}; -
γ_1	Clapeyron slope (410 km)	4.1	$MPaK^{-1}$
$\boldsymbol{\delta\rho_1}$	Density contrast (410 km)	273	Kg m^{-3}
γ_2	Clapeyron slope (660 km)	-1.9	$MPaK^{-1}$
$\boldsymbol{\delta\rho_2}$	Density contrast (660 km)	342	Kg m^{-3}
$\boldsymbol{\eta_{LM}}$	Viscosity of the lower mantle	2×10^{22}	Pa s
$\boldsymbol{A_{diff}}$	Diffusion prefactor	5.3×10^{15}	s^{-1}
$\boldsymbol{A_{disl}}$	Dislocation prefactor	2×10^{18}	s^{-1}
$\boldsymbol{V_{diff}}$	Activation volume for the diffusion creep	4-6	cm^3mol^{-1}
$\boldsymbol{V_{disl}}$	Activation volume for the dislocation creep	8-12	cm^3mol^{-1}
$\boldsymbol{E_{diff}}$	Activation energy for the diffusion creep	240	KJ mol^{-1}
$\boldsymbol{E_{disl}}$	Activation energy for the dislocation creep	423	KJ mol^{-1}
$\boldsymbol{b}$	Burgers vector	5×10^{-10}	m
$\boldsymbol{d}$	Grain size	10^{-6}	m
R	Gas constant	8.314	$J\ mol^{-1}K^{-1}$
$\boldsymbol{m}$	Grain size exponent	2.5	-
$\boldsymbol{n}$	Stress exponent dislocation creep	3	-
$\boldsymbol{T_0}$	Normalized surface temperature, $T_{surf}/\Delta T$	0.1605	-
$\boldsymbol{Di}$	Dissipation number, $\alpha gh/c_p$	0.24	-
$\boldsymbol{\Phi}$	Viscous dissipation	-	W m^{-3}
γ	Yield stress gradient	0.1-0.6	-
$\dot{\boldsymbol{\varepsilon}}$	Second invariant of the strain rate, $(1/2\Sigma_{ij}\dot{\varepsilon}_{ij}{}^2)^{1/2}$	-	s^{-1}
$\boldsymbol{v_j}$	*i*-th component of the velocity	-	-
$\boldsymbol{P}$	Lithostatic pressure	-	-
$\boldsymbol{\partial_i}\Delta P$	Dynamic pressure gradient, $\partial_i P - \rho_0 g_i$	-	-
$\boldsymbol{\tau_{ij}}$	*Ij*-th component of the deviatoric stress tensor, $\eta\dot{\varepsilon}_{ij}$	-	-
$\boldsymbol{T}$	Temperature	-	-
$\dot{\boldsymbol{\varepsilon}}_{\boldsymbol{ij}}$	Strain rate, $\dot{\varepsilon}_{ij} = \partial_i u_j + \partial_j u_i$	-	-
μ	Shear modulus	80×10^9	Pa

Table 4.1. List of parameters.

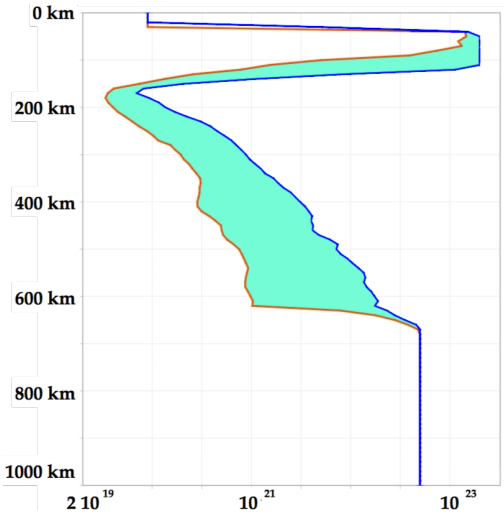

Figure 4.6. Viscosity profiles in the beginning of the subduction process for models with highest and lowest value for the activation volumes of dislocation and diffusion creep. The depth profiles are taken in the point (marked with a star in Figure 3) with surface coordinates (800km, 700 km).

The activation volume was varied between 4 and 6 cm^3mol^{-1} for diffusion creep and 8-12 cm^3mol^{-1} for the dislocation creep respectively and the strength of the material defined in terms of τ_{max} was varied in the range of 50-1200 MPa for different parts of the model and in different experiments as was also done by others [Alisic et al., 2012; van Hunen and Allen, 2011]. This allowed us to experiment with weak and strong continental margins in combination with weak or strong slabs evolving through a weak or strong ambient mantle. The strength of the continental lithosphere was also defined by a maximum yield stress value and was varied between 200-800 MPa. The rheological strength of the continental margins is essentially unknown. Margin strength was varied between experiments and preset in each experiment with the value of τ_{max} ranging between 50 and 800 Mpa (Table 4.2).

To illustrate the typical range in upper mantle viscosities resulting from these parameter variations we show in Figure 4.6 the average difference between viscosity profiles for the models with strong and weak ambient mantle rheology at the beginning of the subduction process just before the development of fast rollback. These profiles are taken in the "undisturbed"

part of the domain, i.e. far from the subduction zone (marked with a star in Figure 4.4) where strong strain rate variations may determine rheology. The blue line shows the viscosity profile for a model with strong rheology using $V_{diff} = 6\ \mathrm{cm^3 mol^{-1}}$ and $V_{disl} = 11\ \mathrm{cm^3 mol^{-1}}$. The orange line corresponds to the viscosity profile for a similar model experiment but with a weak rheology using $V_{diff} = 4\ \mathrm{cm^3 mol^{-1}}$ and $V_{disl} = 8\ \mathrm{cm^3 mol^{-1}}$. The lower mantle viscosity for these two models was set to $5\text{x}10^{22}$ Pa s following Cizkova et al. [2012]. The minimum viscosity allowed is set to $1\text{x}10^{19}$ Pa s and maximum viscosity is set to 10^{24} Pa s [Magni et al., 2012; Garel et al. 2014]. We refer to Chertova et al. (2012) for illustrations of viscosity field evolution typical for subduction evolution as is modeled here.

The viscosity of the weak crustal layer that allows slab decoupling from the top free-slip surface was taken as 9×10^{19} Pa s and its thickness is 30 km. Here we follow the approach of Cizkova et al. [2007], OzBench et al. [2008], Stegman et al. [2010], Chertova et al. [2012], and Capitanio et al. [2013].

4.4.4 Initial conditions

The three tectonic reconstructions scenarios essentially start from different initial subduction zone configurations at ~35 Ma. These were translated here into initial temperature conditions for 3D modeling. In Figure 5 we display four setups of initial configurations for scenarios S1, S2 and S3, where S1a and S1b are alternative starting configurations for S1, which will be discussed below (section 5.1.3). In addition to the map-view display of Figure 4, thick dark red zones indicate the location of the subduction zone at ~35 Ma. Vertical cross-sections depict the character of the margins, passive or subduction, and amount of initial subduction.

We assumed an initial subduction "channel" of 40 km filled with a weak material with a viscosity of 9×10^{19} Pa s [van Hunen and Allen, 2011; Chertova et al., 2012]. The relatively large width of the subduction channel is not critical [Chertova et al., 2012] and only and facilitates decoupling of the slab and overriding plate in the initial few million years of subduction in the presence of advancing African motion before active subduction turns into a regime of predominant slab rollback.

The dashed lines in Figure 4.5 between the Baleares and African margins represent a weakness zone which separates the oceanic lithosphere of the

RGB slab in the west from the lithosphere that will rollback to the southeast and east [Spakman and Wortel, 2004]. The subduction that occurred to the east of the decoupling zone it is not incorporated in the main modeling effort here, although we will show one model in which we took the Kabylides segment into account. For all scenarios, the decoupling zone is implemented as a narrow (70 km) region filled with thin young oceanic lithosphere (5-50 My), although in reality it may have been an inherited transform fault that formed during the Jurassic opening of the Alpine Tethys. This lithosphere acts as a weakness zone due to its temperature determined rheology at shallow depths. To the east of this decoupling zone we have implemented a 100 My old oceanic plate.

Although we model the Alpine-Tethys lithosphere as being of oceanic origin, its precise character is unknown. It is Jurassic to earliest Cretaceous in age [Vissers et al., 2013], but it cannot be excluded that the now subducted domain was (partly) of transitional nature resulting from thinning of continental lithosphere, which subsequently cooled and thickened similar to oceanic lithosphere in terms of thickness and temperature structure. The initial temperature profile of the oceanic/transitional lithosphere is determined from the equation of cooling of a semi-infinite half space for a lithosphere age of 100 My, equivalent to an earliest Cretaceous lithosphere age consistent with the age of the end of spreading of the Alpine Tethys ocean [Vissers et al., 2013]. A constant temperature gradient of 10 K/km is prescribed for the continental lithosphere across its thickness of 150 km.

4.4.4.1 Scenario 1: Initial subduction confined to the Balearic margin (models: S1.*)

The initial geometry for S1 is quantified from the recent reconstruction of van Hinsbergen et al. [2014] and presented in Figure 4.5, panel S1a. At ~35 Ma, the initial trench is 300 km long and located south of the Balearic Islands. In the east, the initial slab length is ~200 km from the surface. This decreases to 0 km below the base of the lithosphere close to the Iberian margin just west of cross-section CD in Figure 4.5-S1a. The initial subduction direction is NW with an assumed dip angle of 40^{o}.

The thickness of both European and African continental margins is gradually increasing toward the interior of the continents. We experimented with different initial settings of maximum yield stress (eq. 4.5e). Weak margins

were defined by $\tau_{max} = 50 - 200$ MPa and strong margins by $\tau_{max} = 400 - 800$ Mpa.

For the continental margin of south Iberia we also experimented with different initial margin geometries (Figure 4.5). Between 80 Ma and 35 Ma, convergence between Africa and south Iberia was not more than a few tens of kilometers [van Hinsbergen et al., 2014], and may have led to thickening of the south Iberian margin. We mimicked the margin thickening by a gradual increase in margin thickness from 0 km at Gibraltar to ~30 km at the transition to the Baleares margin as depicted in Figure 4.5-S1b. This led to a mechanically stronger margin for which we could still vary the maximum yield stress τ_{max}.

4.4.4.2 Scenario 2: Initial subduction along the entire Iberian-Balearic margin (models S2.*)

Scenario S2 assumes an initial subduction zone of 900 km along the entire Iberian margin from the Gibraltar to the Baleares (Figure 4.5-S2). We experimented with models starting from an initial length of the slab of ~400 km all along the Iberian-Baleares margin and with models in which the depth of the slab below the base of the lithosphere increases linearly from 0 at Gibraltar to ~300 km at the eastern Baleares as end-member models for scenario S2. The initial subduction direction was north at Gibraltar, gradually changing to northwest under the Balearic margin with a subduction angle of ~40°.

4.4.4.3 Scenario 3: Initial SE dipping subduction under the North African margin (models S3.*)

Initial conditions of a S-dipping subduction zone under the African margin are shown in Figure 4.5–S3. At ~35 Ma, the length of initial slab was ~300 km with an initial subduction angle of ~45°. The trench started at the north-African margin ~300 km to the east from the (future) Moroccan Rif. Between the Rif and the trench a wide continental margin (110 km) was prescribed [Verges and Fernandez, 2012; van Hinsbergen et al., 2014]. Along southern Iberia we prescribed a continental margin of which the strength is controlled by τ_{max}. The geometry of the weak decoupling oceanic transform zone (dashed in Figure 4.5-S3) is taken from Verges and Fernandez [2012] and was

located more to the west than in S1 and S2, excluding most of the Balearic margin.

4.4.5 Criteria for model evaluation, modeling targets, and optimization strategy

Our primary target for model evaluation is prediction of the observed present-day mantle structure. However, current tomography models are not perfectly resolved [Spakman and Wortel, 2004; Bezada et al., 2013] and lead to a blurred view on mantle structure. Therefore we compare predictions of slab morphology to the robust features of the imaged slab anomaly, which we identified as the curvature and position of the slab (section 4.2; Figure 4.3). These targets should be reached after 35 My of subduction evolution starting from the initial conditions defined above.

We note that observations and interpretations of present-day mantle anisotropy [e.g. Diaz et al. 2010; Alpert et al. 2013; Diaz and Gallart 2014] and of crustal motions [e.g. Vernant et al. 2010; Koulali et al. 2011] are not taken here as particular modeling targets because the sensitivity of these observations for the past 35 My of subduction evolution is unknown.

The temporal evolution of subduction is another important constraint. An intermediate milestone for all numerical models is that slab rollback largely stalls at ~8 Ma as suggested by earlier mentioned geological constraints. For S1 and S2 an intermediate target is the collision of the Kabylides with Africa (~15-17 Ma), which corresponds to rollback of the easternmost part of our modeled slab having reached the African margin.

Our models started with the initial buoyancy field as described in the previous sections. Slab buoyancy and the prescribed plate motions at the south-edge and north-edge of the model domain drive the subsequent subduction evolution. As the rheology of the mantle, slab, and margins is poorly known we tuned these for different model regions (by varying parameters in eq. 4.5) to optimize for each reconstruction scenario the possibility for the end-stage of slab evolution to approximate the real-Earth targets.

Model	τ_{max} (MPa)				Subd.z. l. (km)	Kin. Par.	γ	V_{dis}; V_{dif} (cm^3/mol)	Sl.d. (km)
	Oc.l	Con.l	Eu.m	Af.m					
Scenario 1: Exploring rheology of the mantle and continental margins									
S1.1-1	800	800	800	800	300	D	0.2	8; 5	50
S1.1-2	800	800	100	100	300	D/2	0.1	9; 5	50
S1.1-3	400	800	100	100	300	D/2	0.3	9; 5	50
S1.1-4	1200	800	100	100	300	D/2	0.3	9; 5	50
S1.1-5	400	800	50	50	300	D/2	0.1	8; 4	50
S1.1-6	800	400	100	100	300	D/2	0.1	9; 5	50
S1.1-7	800	200	100	100	300	D/2	0.1	9; 5	50
S1.1-8	800	800	100	100	300	D	0.3	8; 4	50
Scenario 1: Exploring the strength of the Iberian margin									
S1.2-1	800	800	800	100	250	D	0.2	8; 4	50
S1.2-2	800	800	800	200	250	D	0.3	8; 4	50
S1.2-3	1000	1000	1000	200	250	D	0.5	8; 4	50
S1.2-4	1000	1000	1000	50	250	D	0.6	8; 5	50
Scenario 1: Increasing Iberian margin thickness									
S1.3-1	800	800	200	100	800	D	0.3	8; 4	50
S1.3-2	800	800	800	100	250	D	0.3	8; 4	50
Scenario 2: Initial N-NW directed subduction from Gibraltar to the Baleares									
S2.1-1*	800	800	50	50	800	D/2	0.1	8; 4	200
S2.1-2	800	800	50	50	800	D/2	0.1	8; 4	200
S2.1-3	800	800	200	200	800	D	0.3	9; 5	200
S2.1-4	800	800	200	800	800	D	0.3	11; 6	200
Scenario 3: Initial S-SE dipping subduction under the African margin									
S3.1-1	800	800	200	200	400	D	0.3	8; 4	150
S3.1-2	800	800	800	200	400	D	0.3	9; 4	150
S3.1-3	800	800	800	200	400	D	0.5	10; 5	150
S3.1-4	800	800	800	800	400	D	0.5	12; 6	150
S3.1-5	800	800	800	800	400	D	0.3	10; 5	60
Scenario 1: Sensitivity of subduction models to variations in initial conditions									
S1.4-1	800	800	800	100	250	D	0.3	8; 4	90
S1.4-2	800	800	800	100	250	D	0.3	8; 4	50
S1.4-3*	800	800	800	100	250	D	0.3	8; 4	60
S1.4-4*	800	800	800	100	250	D	0.3	8; 4	50
S1.4-5*	800	800	800	100	250	D	0.3	8; 4	50
S1.4-6	800	800	300	100	250	D	0.3	8; 4	50
S1.4-7*	800	800	800	100	250	D	0.3	8; 4	50

Table 4.2. List of models. Models marked S1., S2.*, or S3.* are computed for tectonic scenarios S1, S2, S3, respectively. Oc.l. and Con.l. means oceanic and continental lithosphere respectively, Eu.m. and Af.m – European and African margin, Vdis and Vdif activation volumes for the dislocation and diffusion creep and Kin. Par. – kinematic parameters implemented to the*

*African and European plates. Models marked with * depend on additional parameters which are not included in this table. For the description of these models see text.*

4.5 Experiments

A summary of important models is given in Table 4.2. The models are divided into six groups, each serving a particular modeling objective. Model names start with the scenario identifier S1, S2, or S3.

4.5.1 Scenario 1: Initial subduction confined to the Baleares margin.

We started our experiments with modeling the subduction evolution based on S1. This is the most complex evolution scenario and involved a large number of experiments to explore the plausible range of parameters for mantle viscosity and strength of the continental margins. From this experience we benefited in modeling the subduction evolution for tectonic scenarios S2 and S3.

4.5.1.1 Exploring rheology of the mantle and continental margins

From an initial condition of a short slab, extending ~50 km under the Balearic lithosphere (Figure 4.5-S1a), all models (Table 4.2) start to roll back, initially to the south and subsequently quite rapidly rotating to the west. The transition between the Iberian margin and Balearic subduction zone initially acts as a pivot point about which rollback rotates to the west. For a strong slab, the strength of the margin at this point determines whether the margin starts to fail (weak margin) or whether it will act against further rollback (strong margin). These observations are also valid for tearing of the north African margin accommodating westward rollback.

Model S1.1-1 (Figure 4.7) is an example of a model with a strong Iberian and African margin (τ_{max} =800 MPa) and a strong slab (τ_{max} =800 MPa). During the first 5 My, the slab under the Baleares margin subducts another ~50 km in northwest direction (Figure 4.7, 30 Ma) with relative convergence speed of 6 mm/yr, followed by increasing rollback to the southwest. Such a rapid transition is also observed in other numerical and laboratory experiments [Becker et al., 1999; Faccenna et al., 2001, Schellart and Moresi, 2013]. When

the trench reaches the African margin at ~25-20 Ma rollback only occurs westward. No appreciable tearing occurs in the slab or along the margins during the last 20 Ma of evolution. Slab rollback gradually stagnates while the slab thickens due to ongoing Africa-Iberia convergence. At 0 Ma, a wide, shallow anomaly is observed far from the present day slab position under the Gibraltar and this model does not reach the modeling target.

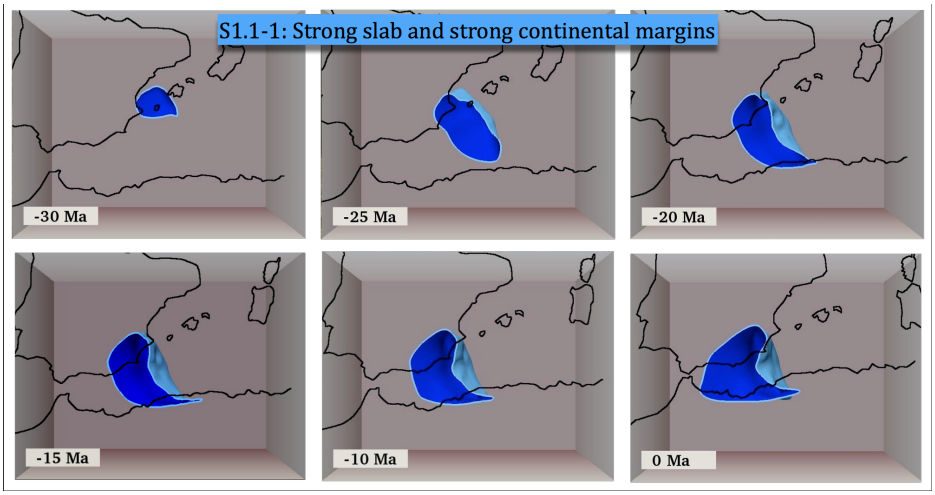

Figure 4.7. Evolution of the model S1.1-1. The 1400°-isotherm of the slab is shown in light blue below 150 km. Dark blue shows the interior of the slab. Black contours indicate the paleo-coastlines of North Africa, Iberia, the Balearic Islands, and of Corsica and Sardinia. These were linearly interpolated between their position at 35 Ma and the present. These coastlines only serve to illustrate the approximate plate position of the African and Iberian continents with respect to the slab.

To allow the slab to progress further to the west, we first tried models (not in Table 4.2) with weaker slabs and weaker margins with $\tau_{max\_slab} = \tau_{max\_margin}$ on the order of 200-300 MPa (eq. 5.e). In these models, margins start to drip from the strong (800 MPa) continents, large holes form in the slab and it experiences major down-dip stretching during the entire evolution, particularly when its base reaches into the more viscous transition zone (410-660 km) while the upper part continues retreat to the west (Appendix A1). Remnants of slab in this model are found under the entire Alboran-Algerian basin, inconsistent with tomography observations. From these experiments we concluded that we should proceed with the combination of a relatively strong

slab to suppress slab stretching, and a weaker continental margin to facilitate tearing.

With the next generation of models (S1.1-2, S1.1-3, S1.1-4 and S1.1-8) we tested different strengths of the oceanic lithosphere and upper mantle in combination with weak continental margins (τ_{max}=50 or 100 MPa) (Table 4.2). In most models we used reduced plate velocities due to initial underestimation of the plate velocities. The best performing of these models is model S1.1-8 for which we used a strong (800 MPa) slab and a weak mantle (V_{dif}=4 cm^3mol^{-1}, V_{disl}=8 cm^3mol^{-1}). Its subduction evolution (Figure 4.8) shows a slab arriving in the present-day target region of Gibraltar. After an initial stage (35-30 Ma) of nearly stationary subduction, fast rollback develops to the SW and later to W. When the trench reaches the African margin, lithosphere tearing starts to propagate to the west along the African and Iberian margins, creating slab edges and associated STEP faults [Govers and Wortel, 2005], accommodating subsequent westward rollback. Slab tearing occurs as a viscous necking process of the weak continental margin [Andrews and Billen, 2009; Mason et al., 2010; Duretz et al., 2011, 2013; van Hunen and Allen, 2011]. The final trench position in model S1.1-8 is slightly to the west and south of the modeling target, and we do not observe the curved morphology of the slab under the Betic region (Figure 4.3). Instead the slab lies under the Alboran and Algerian basins, inconsistent with tomographic models.

To illustrate the influence of mantle and slab strength on the subduction evolution, a west-east cross-section of model S1.1-8 is shown across the Gibraltar Strait in the end-stage (0 Ma) in Figure 4.9 together with the final slab geometry attained in models S1.1-2 and S1.1-4. Compared to model S1.1-8, model S1.1-2 has a weaker slab (defined in terms of a relatively low γ=0.1) and a stronger mantle (V_{diff}=5 cm^3mol^{-1}, V_{disl}=9 cm^3mol^{-1}). As a result the weak slab did not reach the present day position after 35 My of subduction. In model S1.1-4 we used a stronger slab (1200 MPa) than in model S1.1-8 and a stronger mantle restricting slab rollback to a position ~200 km east of Gibraltar. An experiment with a strong slab in a weak mantle led to complete detachment of the slab at ~15 Ma far east of Gibraltar as the weak margins and mantle could not sufficiently support the weight of the slab (Appendix A2).

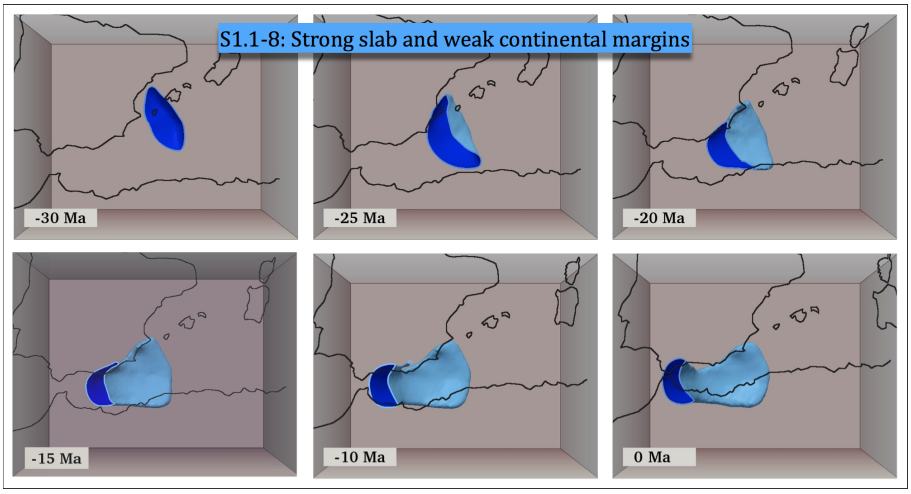

Figure 4.8. The evolution of the model S1.1-8 shown from a depth of 200 km. See caption of Fig. 7 for other descriptions.

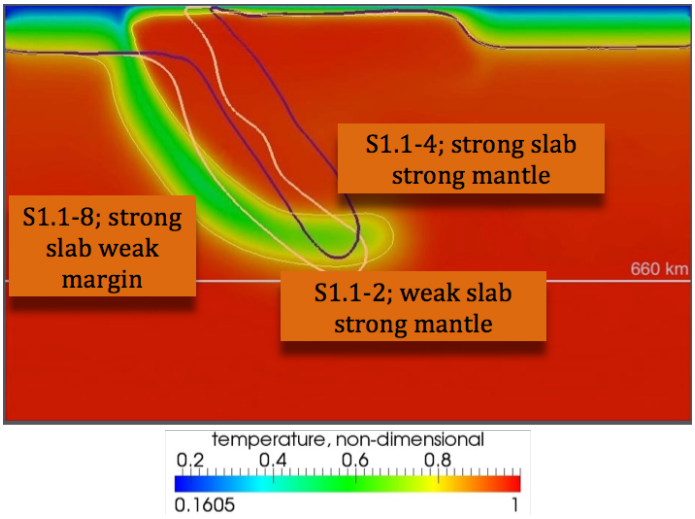

Figure 4.9. W-E cross-section of the temperature field of the model S1.1-8 after 30 My from the beginning of the subduction. The 1400°-isotherm for three models is shown. Colors denote the temperature filed of model S1.1-8.

Two experiments, S1.1-6 and S1.1-7, were performed to investigate the influence of the continental strength on subduction evolution. In these experiments, τ_{max} was reduced by factors 2 and 4, respectively, from the reference value of τ_{max}= 800 MPa. The mantle in these experiments was

strong (activation volumes are 5 and 9 cm^3mol^{-1}), the slab was weak (γ=0.1). Reduction by a factor of 2 did not influence the overall character of the rollback process but with a reduction by a factor 4, the continental lithosphere of Africa became involved in the subduction process, which is not observed in margin geometry or in mantle structure inferred by tomography (Appendix A3).

Based on this group of experiments we continued our experiments with slab strength of 800 MPa and a weak African margin (~50-200 MPa).

4.5.1.2 Exploring the strength of the Iberian margin

As a result of tearing of the Iberian margin and westward rollback, none of the previous models yielded a slab evolution that incorporated ongoing clockwise rotation of the northern sector leading to the E-W trending slab underneath the eastern Betic region (Figure 4.3). With the second group of S1.* models in Table 2 we investigated the potential role of the south-Iberian margin west of the Baleares in causing slab rotation. We tested different values of τ_{max} for the Iberian margin and for oceanic lithosphere, as well as different values for γ, which influences the depth-dependence of τ_y (eq. 4.5e).

The first two models, S1.2-1, S1.2-2 (Figure 4.10), using the strength of 800 MPa for the Iberian margin, showed a similar subduction evolution as model S1.1-8 (Figure 4.8) while the last two models, S1.2-3, S1.2-4, show less trench retreat. The initial evolution was similar to S1.1-8 until the strong Iberian margin locally restricted rollback leading to a clockwise rotation of the slab (25-15 Ma). However, eventually the Iberian margin started to tear, which restored the N-S strike of the trench, leading to an end-stage of rollback similar as for S1.1-8. We conclude that rheological strengthening of the continental margin along Iberia alone does not lead to the observed curvature and location of the slab as portrayed in tomography.

4.5.1.3 Increasing Iberian margin thickness

We subsequently tested the effect of a thickened Iberian margin (Figure 4.5-S1b; section 4.4.4.1), which provides additional strength to the margin independent of its rheological/material strength. Variation of rheological parameters started from those used for model S1.1-8 (Figure 4.8). In model S1.3-1 the strength of the thickened European margin was 200 MPa. The model developed similar to S1.2-group of models and was not successful in preventing early lithosphere tearing under Iberia.

Next, a strong 800 MPa and thickened European margin (Figure 4.5-S1b) was used leading to model S1.3-2 (Figure 4.11). Until 25-20 Ma this model is similar to S1.2-2 (Figure 4.10), after which the slab stayed connected to the Iberian margin and consequently rotated clockwise into the curved geometry as observed in the mantle today. At ~10 Ma the slab reached its present-day position with little change in slab morphology until 0 Ma.

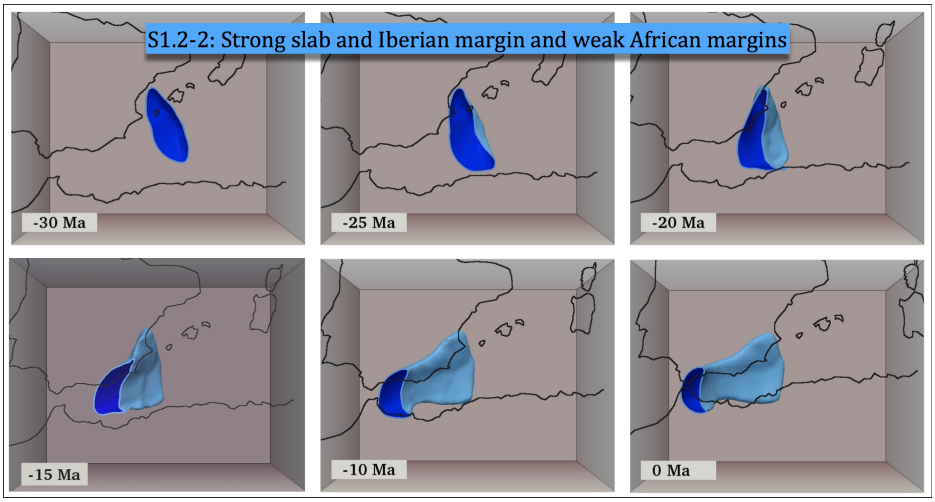

Figure 4.10. The evolution of the model S1.2-2 is shown below 200km. See the caption of Fig. 4.7 for other descriptions.

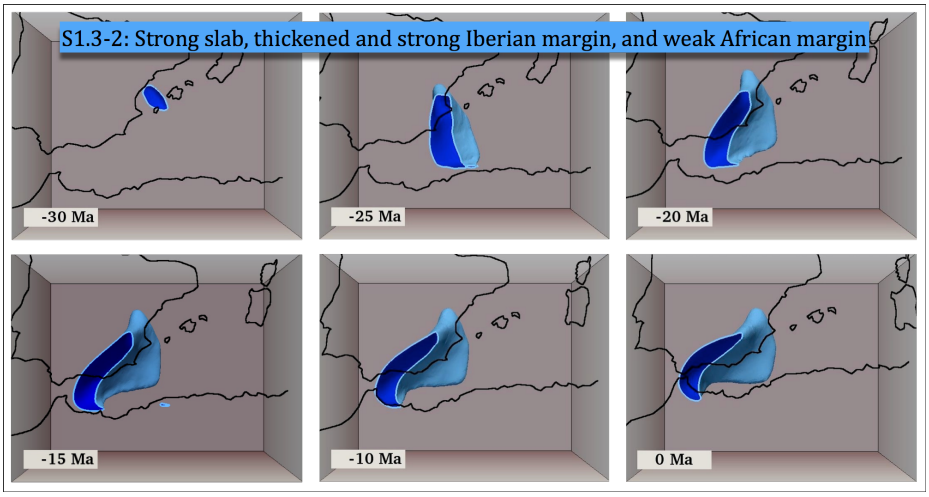

Figure 4.11. The evolution of the model S1.3-2 is shown below 200 km. See the caption of Fig. 4.7 for other descriptions.

Viscous necking of the subducted Iberian margin lithosphere was incipient during the last 10 My, but did not evolve into a detachment under the eastern Betic region as is observed in tomography. Apart from that, the present day trench position and continuous Gibraltar slab, the slab edge under the Moroccan Rif, the curved slab structure under the Betics, as well as the deeper slab structure successfully reproduced the tomographically imaged structure of the RGB slab (Figure 4.3) [Spakman and Wortel, 2004; Bezada et al., 2013; Palomeras et al., 2014].

4.5.2 Scenario 2: Initial N-NW directed subduction from Gibraltar to the Baleares

Within the parameter space as determined in the previous sections, we now test whether the initial conditions of Scenario 2 (Figure 4.5-S2, section 4.4.4.2) could also evolve into the present-day slab geometry inferred by tomography.

In a first configuration, a slab was implemented with an along-strike varying initial depth from 0 km below base of the lithosphere at Gibraltar to ~300 km below the Baleares. This initial setting led to subduction evolution model S2.1-1 (Figure 4.12; Table 4.2) with a rollback evolution similar to models like S1.2-2 (Figure 4.10) although tearing now only occurred along the African margin. After a short phase (4-5 My) of stationary subduction, fast rollback developed in a southwest direction and evolved quicker than previous models because of the longer initial slab length toward the NE (Baleares). From ~30 Ma to ~15 Ma, the trench retreated in a SW direction until it reached the Gibraltar region. The resulting shape of the trench is comparable to models S1.1*-S1.2*, but is rotated more in anticlockwise direction and located more to the south relative to these models. This resulted from a higher degree of southward rollback with subduction of African continental subduction during the last few My. The final slab morphology predicts the first 300-400 km of slab to be positioned largely under northern Africa. In addition, slab in the upper mantle transition zone is predicted under the Alboran and west Algerian basins as well as under southern Iberia. This slab morphology is not observed in tomographic models (section 4.2).

The second slab configuration we tested consisted of a uniform initial slab length of ~400 km along the entire Iberian-Baleares margin (Figure 4.5-S2).

This initial configuration was tested in models S2.1-2, S2.1-3, and S2.1-4, which differed in African margin strength and in increasingly stronger mantle rheology, respectively (Table 4.2). Model S2.1-2, with a weak African margin, exhibited fast rollback to the south and the slab completely detached from the surface after 15 My of the evolution. After 30 My, the detached slab was lying entirely on the 660 km boundary. For the part of the slab at the transition to Atlantic lithosphere in the Gibraltar region we observe fast lithosphere tearing in a southward direction, despite the 800 MPa strong Atlantic lithosphere of this region. The resulting slab geometry is not observed in the present-day mantle.

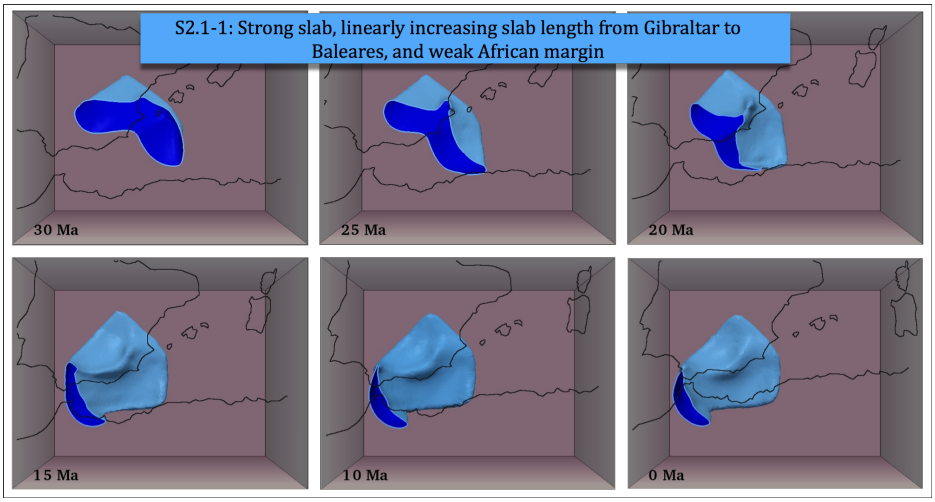

Figure 4.12. Evolution of the model S2.1-1 is shown below 200km. See the caption of Fig. 4.7 for other descriptions.

With the next two models, S2.1-3, and S2.1-4 (Figure 4.13), we attempted to suppress early lithosphere tearing by tuning the strength of the mantle and African margin targeted at optimizing the correlation between predicted and observed slab structure. These attempts were not successful. The large initial buoyancy force of the 400 km long slab produced fast mantle flow and high strain rates locally reducing the viscosity in the asthenosphere as a result of strong nonlinear dislocation creep (eq. 4.5c). Counteracting this behavior was possible through strengthening the mantle rheology by using higher activation volume values for diffusion and dislocation creep than used for models of the S1-group, e.g. S1.3-2 (Figure 4.11).

Slab evolution is illustrated through the last model S2.1-4 (Figure 4.13) in which the African continental margin and the oceanic plate have the same strength and the mantle is strongest. This model yielded slower rollback than in model S2.1-2 but nevertheless after 35 My of subduction evolution the slab is almost detached. Due to a stronger continental margin than in S2.1-2, the tearing zone for this model is now localized within the subducted slab instead of the continental margin. For scenario S2 we found no combination of initial slab geometry and margin/slab/mantle rheology that would lead to an end-stage comparable the present-day slab geometry (Figure 4.3). In particular, none of the models show a tendency to create a slab curvature from N-S at Gibraltar to E-W below southern Iberia between depths of 0-400 km.

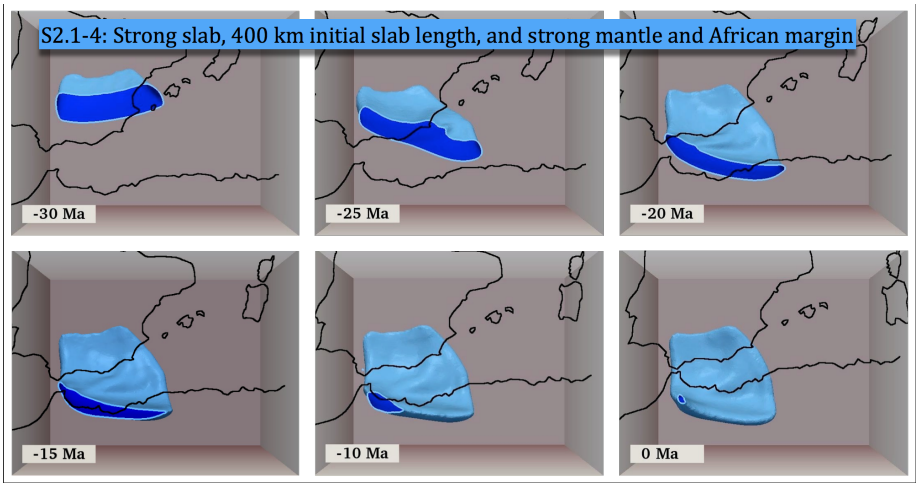

Figure 4.13. Evolution of the model S2.1-4 below 200km. See the caption of Fig.4. 7 for other descriptions.

5.3 Scenario 3: Initial S-SE dipping subduction under the African margin

Lastly, we tested whether modern mantle structure can be obtained by starting from the initial conditions of Scenario 3 (Figure 4.5-S3, section 4.4.4.3). Initial slab length is ~300 km. The first model S3.1-1 (Figure 4.14) implemented strength of 200 MPa for continental margins and 800 MPa for lithosphere (Table 4.2). In the first 4-5 My, stationary subduction gradually turned into a northward rollback regime followed by rapid rollback in the following ~5 My in predominantly northern direction. Next, lithosphere

tearing developed along the weak Iberian margin and the direction of the rollback rapidly changed to westward. After 18-20 My the trench reached Gibraltar with a N-S strike of the trench. The rollback process slowed down and stopped after 30 My of subduction evolution with a trench located west of Gibraltar. No slab curving under southern Iberia is predicted in this model.

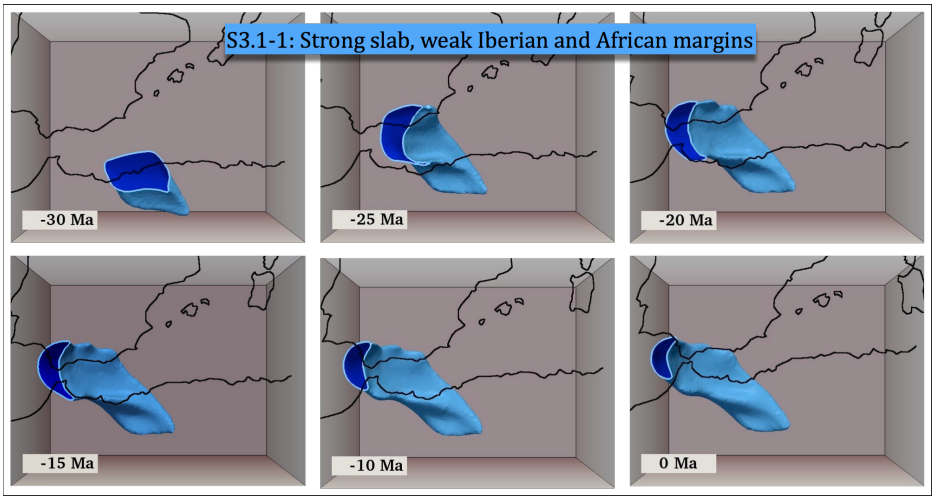

Figure 4.14. Evolution of the model S3.1-1 below 200km. See the caption of Fig. 4.7 for other descriptions.

For the next experiments we increased the strength of the European margin to prevent lithosphere tearing and generate bending. The values for the activation parameters as well as γ for τ_y were also increased to provide more mantle support for the slab and suppress fast lithosphere tearing along the Iberian margin. The best performing model (S3.1-4) is shown in Figure 4.15A. Subduction evolution up to 20 Ma is similar to S3.1-1 with initial slow subduction followed by rollback in northerly direction. After reaching the Iberian margin no lithosphere tearing occurred. Although in the uppermost mantle the trench and the slab have a curvature consistent with tomographic constraints, the deep part of the slab reaches far below the African plate, which is inconsistent with tomographic constraints (Figure 4.3).

As an attempt to improve the correlation between the modeled and observed slab at depths >200 km, we decreased the initial length of the slab at 35 Ma by ~100 km so as to suppress deep mantle resistance to the slab rollback and allow further slab propagation to the north. In the end-stage of this model, the slab is still located under northern Africa partly because of the northward

motion of the Africa plate overriding the deep slab since the start of rollback (Figure 4.15B). Although tectonic evolution scenario S3 comes closer to predicting the observed shallow mantle structure, a good fit between the overall predicted and observed slab morphology could not be achieved by varying the rheology, margin attributes, or initial slab geometry.

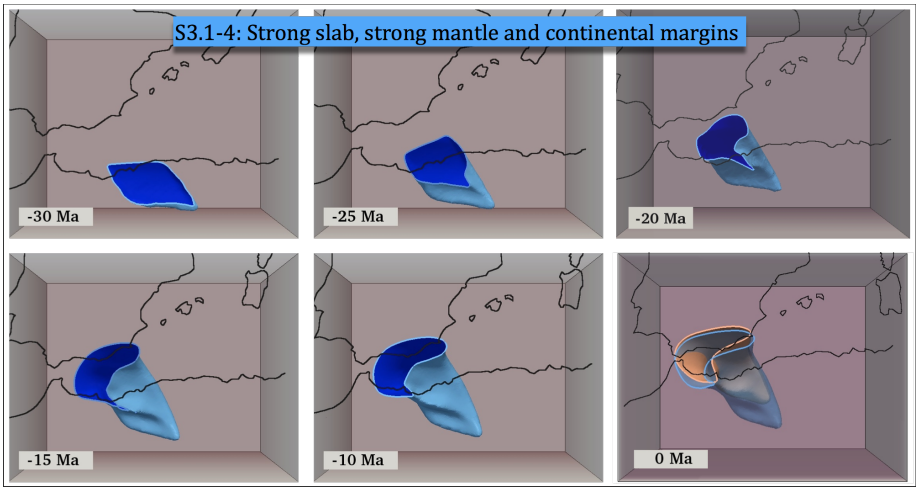

Figure 4.15. Evolution of the model S3.1-4 (blue) below 200km. In the last snapshot (0 Ma) two models S3.1-4 and S3.1-5 are shown. The last model, S3.1-5 is shown in orange color. See the caption of Fig. 4.7 for other descriptions

4.6 Discussion and additional experiments

4.6.1 Comparison of the best-fitting subduction models of each tectonic scenario

Our experiments demonstrate that the initial subduction configurations of the three different tectonic evolution scenarios lead to distinctly different subduction evolution of which the end-stage of slab morphology can be compared to the present-day mantle structure. Figure 4.16 shows from each tectonic scenario the subduction model that best fitted present-day mantle structure, i.e. S1.3-2 (Figure 4.11), S2.1-4 (Figure 4.13), and S3.1-4 (Figure 4.15).

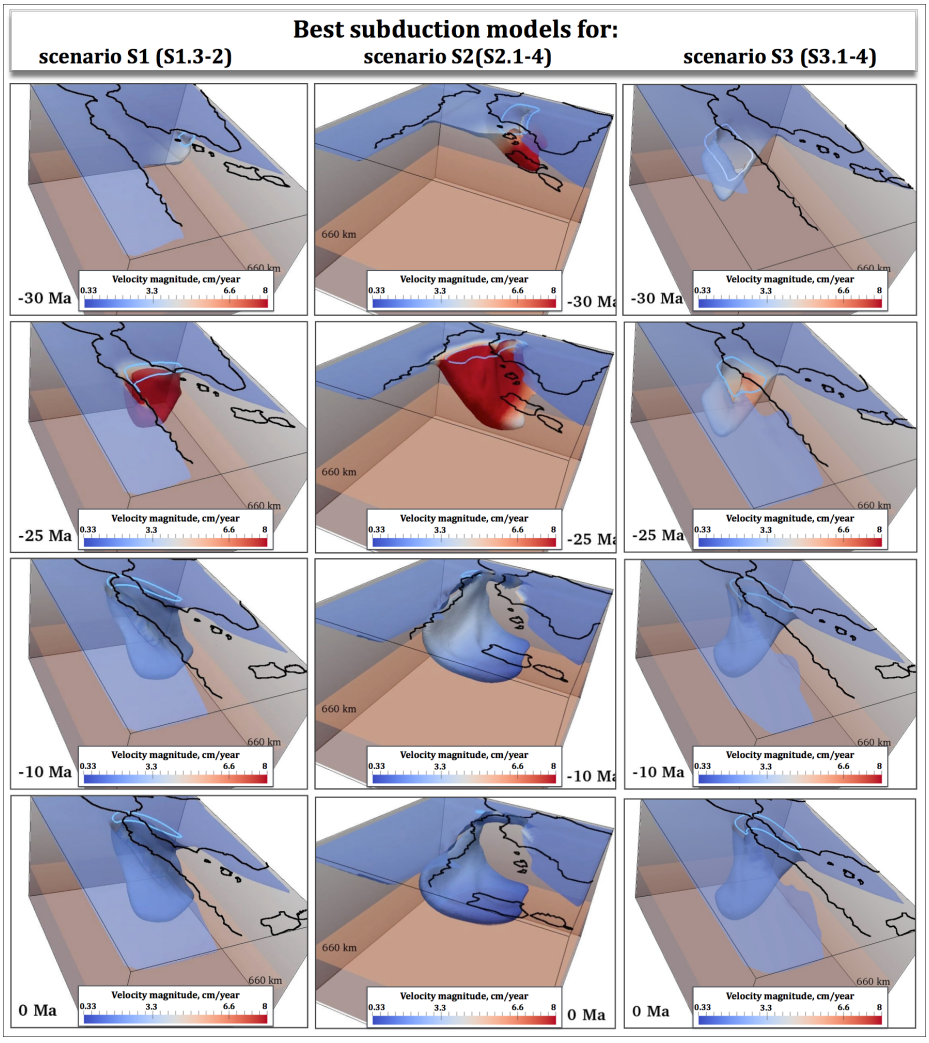

Figure 4.16. 3-D view on the evolution of the best model obtained for each reconstruction scenario. Left: Scenario S1, model S1.3-2, starting from a short trench at the Baleares margin. Middle: Scenario S2, model S2.1-4, starting from a long initial subduction zone and long slab. Right: Scenario S3, model S3.1-4, starting from a trench at the African margin. For S1.3-2 and S3.1-4 the view is from the southeast and for model S2.1-4 the view is from northeast. Blue contours at the surface show the shape of the cold anomaly at depth of 200 km.

In all models we observe an initial phase of fast rollback which reduces in speed once the slab entrains the more deeper and viscous mantle and even more when the slab comes into contact with the viscosity increase across the 660 km discontinuity, similar to those observed in laboratory experiments [Faccenna et al., 2001]. The subduction process developed initially much faster for models S2.1-4 and S3.1-4 than for S1.3-2 even though the mantle rheology for the first two models is much stronger. The cause is the smaller initial slab buoyancy in model S1.3-2. However, after 10 My of slab evolution model S1.3-2 evolved faster as a result of gradually increasing slab buoyancy and because margin tearing evolves in the dynamically favorable geometry of a STEP [Govers and Wortel, 2005] where trench and margin are perpendicular. By ~10 Ma, subduction in all three models had slowed down considerably, consistent with geological constraints.

For scenario S3, by tuning rheological parameters, we managed to model the curved orientation of the trench from Gibraltar to the Iberian margin, and upper part of the slab is consistent with tomographic observations (S3.1-4). Although this resembles the geometry of model S1.3-2 around 200 km depth, deeper in the upper mantle, particularly in the transition zone, the slab is located below the African margin, which is inconsistent with tomographic models (Figure 4.3). The S3.1-4 slab is also thicker in horizontal cross section than S1.3-2. This deformation resulted from the stronger mantle rheology that was required for modeling rollback to the south Iberian margin. At depth these two models become distinctly different which primarily is due to the initial subduction configurations.

The slab shape in model S2.1-4 is completely different from the two other models. The slab was attached to the African margin through a thin “neck” under northern Morocco. The deep part of the slab in this experiment was very wide and was extending far below Iberia, which is not observed in the imaged structure of the upper mantle for this region (Figure 4.3).

Subduction evolution model S1.3-2 (Figure 4.11, 4.16a) is the only one that comes close to reproducing first-order morphology and position of imaged mantle structure. It also complies with the first order geological observation (Section 4.3) that the subduction trench became essentially inactive around ~8 Ma. The match of predicted structure (Figure 4.11) to observed (Figure 4.3) is good in the top 300-400 km. In the deeper upper mantle, model S1.3-2 shows a more SW-NE orientation of the slab, whereas in tomography (Figure 4.3,

and Bezada et al. [2013]) the orientation is more WSW-ESE. This is because the southern deep part of the slab did not roll back further to the west. The final dipping and flattening geometry of the Gibraltar slab is presented in Figure 4.17 and shows a steep slab down to ~400 km depth, flattening in the transition zone. A steep Gibraltar upper mantle slab is imaged in tomography along the same W-E cross-section trough the Gibraltar straight [Gutscher et al., 2002; Spakman and Wortel, 2004; Bezada et al., 2013]. The difference with the modeled slab concerns the part in the transition zone that may be too stiff to bend, or it may be too long. Slab length in this Gibraltar cross section is determined by the initial lateral stretch of lithosphere along the African margin from Gibraltar to the (dashed) oceanic weakness zone in Figure 4.5-S1b that became involved in subduction (Figure 4.5-S1b). Hence the fit between observed and modeled slab is dependent on the initial geometry, along the African margin and in depth, of actual slab tearing in the Middle Miocene, which is unknown.

The modeled dynamic subduction evolution of model S1.3-2 provides a plausible geodynamic backbone of tectonic evolution and substantiates the tectonic evolution framework for RGB subduction as proposed by Spakman and Wortel [2004] that focused on slab tearing and curvature and the >180° rotation of the RGB-trench along the Betic margin. Rosenbaum et al. [2002], and recently van Hinsbergen et al. [2014] reconciled the first-order aspects of the geological evolution of the region with this geodynamic subduction framework.

For scenario S2 we could not find a model that correlates well with the tomographic observation of slab structure of the western Mediterranean despite tuning the rheology of the mantle and margins or the initial slab length. Similarly, we failed to find such slab evolution model for S3. For scenarios S2 and S3 we conclude from our experiments that the dynamically modeled slab evolution is quite different from how subduction evolution was originally portrayed to occur in each scenario. Therefore these proposed slab evolution scenarios cannot be considered to constitute a viable dynamic underpinning of the tectonic evolution scenarios S2 and S3.

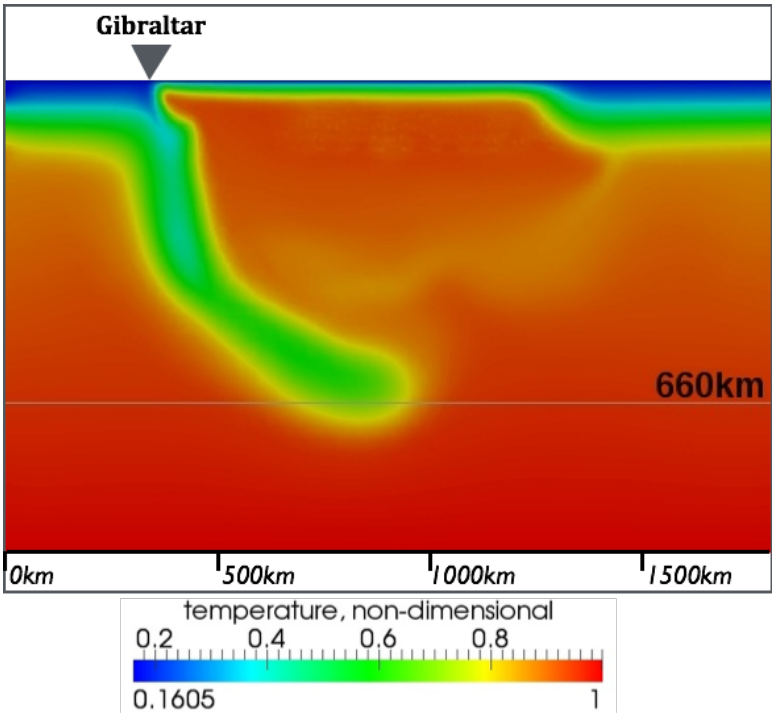

Figure 4.17. Cross-section of the temperature field of the model S1.3-2 after 35 My of subduction evolution, i.e. at 0 Ma.

4.6.2 Sensitivity of subduction model S1.3-2 to variations in initial conditions

For our preferred model, S1.3-2, we performed several tests for the sensitivity of subduction evolution to changes in the initial model configuration (Figure 4.5-S1b).

The first test concerned the model domain size, which we could keep relatively small owing to the use of open boundaries allowing for lateral in- and outflow [Chertova et al. 2012]. We performed a test with increased lateral domain dimensions. The resulting model S1.4-3 (Appendix A4) confirms the findings of Chertova et al. [2012] that slab evolution is not strongly dependent on domain size when using open side boundary conditions, which was implemented in our models.

The second test concerned the initial amount of subduction under Baleares margin, which is constrained to ~90-150 km [van Hinsbergen et al., 2014].

We ran model S1.4-1 (Table 4.2) with a 40 km longer slab than used for S1.3-2. The final position of the slab is more to the east, is less rotated, and the slab is somewhat thicker (Figure 4.18). This is all caused by earlier interaction of the slab with the more viscous transition zone and 660 boundary resisting further sinking and westward rollback.

With the next model S1.4-2 we tested the influence of the absence of phase transitions and of the viscosity jump at 660 km. The resulting slab is at the present-day position but the trench is less rotated and the slab has a smaller N-S extent (Figure 4.18). Primarily the absence of the phase transition and associated viscosity jump allows the slab to sink into the lower mantle, which also allows initiation of lithosphere tearing along the Iberian margin.

Another test concerned the dependence of subduction evolution on the initial thermal structure of the subduction channel. We prescribed sub-lithosphere temperature conditions into the subduction channel, which resulted in faster initiation of slab rollback (model S1.4-4). The resulting geometry of the RGB-slab for this model is shown in Figure 4.19 and reveals only small differences with S1.3-2. The final position at the Gibraltar Strait is the same. The major difference is a slightly longer and thicker slab in its NE edge. This resulted from the faster rollback evolution, which lowers the deforming stresses at the pivoting point for slab rotation at the transition from the Baleares to the Iberian margin.

The location of slab stalling at ~8-10 Ma may be correlated with the position at which we end a weak African margin in the Moroccan Rif region. To test this, we terminated the weak margin 50 km more to the east. The resulting shape of the slab of this model S1.4-5 is shown in Figure 4.20, which shows that slab rollback stalled 30 km more to the east. Hence, the transition from the weak African margin to strong Atlantic lithosphere proves to be important for the rollback evolution.

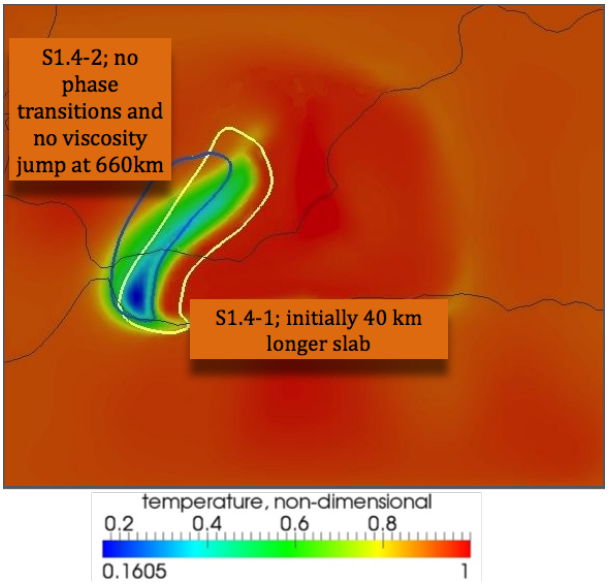

Figure 4.18. Comparison of models S1.3-2 (color contoured temperature plot) with a model starting from a longer initial slab (S1.4-1, yellow contour) and with a model having no phase changes and no viscosity jump (S1.4-2 blue contour). The cross-section is taken after 35 My of subduction, i.e. at 0Ma.

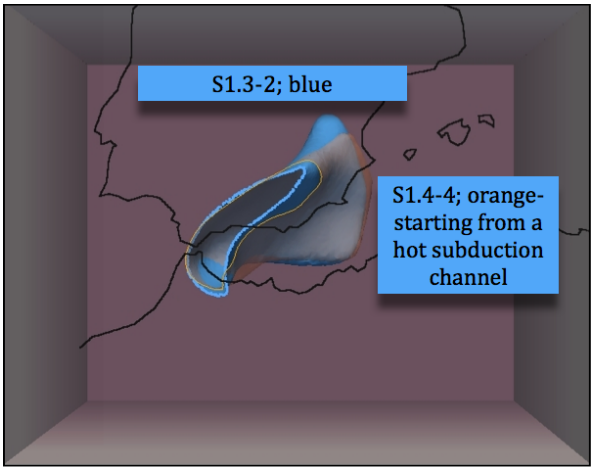

Figure 4.19. The present-day slab shape below 200km for model S1.4-4 (shown in transparent orange) in comparison with model S1.3-2 (Fig. 4.11; light blue).

The last experiment tested for the rheological strength of thickened south Iberian margin. In model S1.4-5 the equal strength of the continental margin and oceanic lithosphere prevented early lithosphere tearing along a thickened (Figure 4.5-Sb) Iberian margin and facilitated trench rotation. However, this model failed to reproduce possible slab breakoff under the eastern Betic since ~10 Ma, as interpreted from mantle tomography [Spakman and Wortel, 2004; Bezada et al., 2013; Palomeras et al., 2014]. In model S1.4-6 we used τ_{max} =300 MPa for the thickened Iberian margin. The resulting end-stage of this model is shown in Figure 4.21 in comparison with model S1.4-4 (transparent blue), which both have the same "hot" subduction channel. The divergence in the evolution of the subduction process for these models started at ~20 Ma. Model S1.4-6 demonstrated a slightly faster rollback rate leading to a slightly more westerly position of the slab at 10-12 Ma. Interestingly, since 10-12 Ma slab breakoff developed under the eastern Betic margin. In the final stage, the Betic segment of the slab was ~200 km shorter laterally than in model S1.3-2 which improves the correlation with the imaged shallow slab structure (Figure 4.3).
These sensitivity tests demonstrate the robustness of the slab evolution underpinning tectonic evolution scenario S1 with respect to small changes in initial conditions.

4.6.3 Stress limited nonlinear rheology for slab, mantle and margins

In our modeling we used a visco-plastic rheology with a simple stress limiting mechanism (eq. 4.5), which facilitated slab bending and trench retreat. The dominant parameters determining the strength of the lithosphere are γ and $\tau_{max.}$ (eq. 4.5). This parameterization of the stress-limiting mechanism is the same as used by others [e.g. Schott and Schmeling, 1998; Enns et al., 2005; OzBench et al., 2008; Mason et al., 2010; Magni et al., 2012] where γ is varied between 0.055 and 0.9 and τ_{max} between 100 and 1200 MPa. When the lower bound (0.055) is implemented for our modeling, then even with a high τ_{max} of 800 MPa, the stress-limiting rheology facilitates easy slab bending leading to fast slab steepening and detachment already after ~15 My of evolution (Appendix A2).

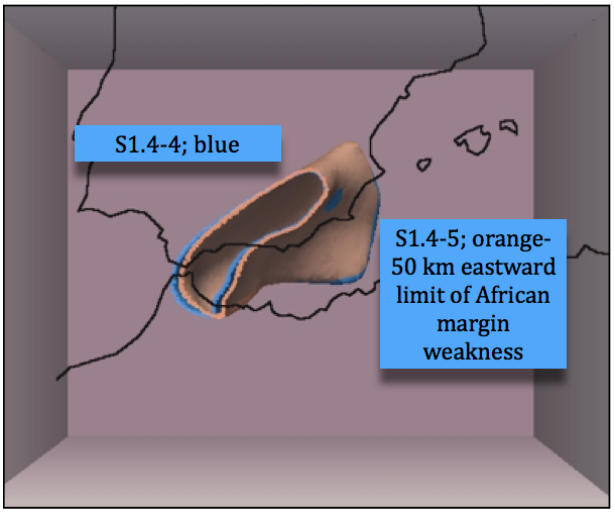

Figure 4.20. The present day slab shape below 200km for model S1.4-5 (orange color). Model S1.4-4 (Fig. 4.19) is given for comparison in transparent light blue.

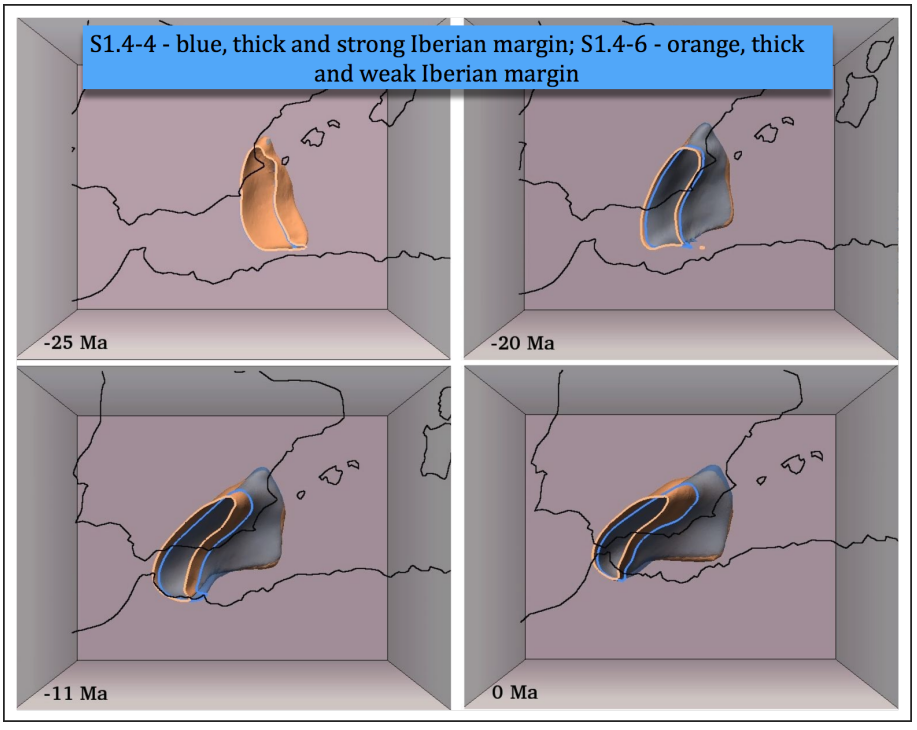

Figure 4.21. Evolution of the model S1.4-6 (orange contour) below 200 km. In blue transparent color model S1.4-4 (Fig. 19) is shown

Increasing the value for γ counteracts early detachment but when it reaches 0.6-0.7 the slab becomes too stiff to bend, hampering subduction evolution. For our models we found an appropriate range for γ of 0.3-0.6 independent of the value of τ_{max}. The strength of the slab in terms of τ_{max} should be between 600 and 800 MPa. Our results suggest that slabs of age > 100 Ma and subducted since the middle Cenozoic under these conditions are too strong for significant stretching. In this case slab stretching can be ignored when comparing estimated slab length/volumes from tomography with predictions from tectonic reconstruction [e.g. de Jonge et al. 1994; Spakman and Wortel, 2004; Spakman and Hall, 2010]. Similar to laboratory experiments (e.g. Funiciello et al. 2008), we observe that strong slabs can still develop very rapid slab rollback with trench speeds of up to 8 cm/yr, as in our modeling.

Our values of τ_{max} for the slab and the continental lithosphere, 600-800 MPa, are different from the values given in Alisic et al. [2012], who suggested a lithosphere-strength of 100 MPa from a global fit to various observables in a global instantaneous dynamic modeling. In our case using a maximum yield stress lower than ~300 MPa invariably resulted into too weak slabs that formed holes and stretched dramatically during rollback. This led to slab morphologies such a flat lying slab in the transition zone under the entire region covered by the Alboran and Algerian basins, which is not observed (Figure 4.3, Appendix A1).

In our models we do not attempt to include the complexities of continental (margin) rheology, which are still not well known (see Burov [2011], for a comprehensive review). We adopted the same nonlinear rheology as for the mantle and tuned overall margin strength with one parameter, τ_{max}. Tearing of continental margins is implied by all tectonic scenarios of the region and inferred from geochemical observations [Coulon et al., 2002; Duggen et al., 2004, 2005], and tomographic observations [Carminati et al., 1998; Spakman and Wortel, 2004]. Another example of continental margin tearing is the recent westward propagation of the Ryukyu trench in the direction of Taiwan (Lallemand et al. 2001). This indicates that continental margins are not necessarily strong when subject to a combination of laterally and vertically directed shear tractions owing to oblique plate convergence.

Our experiments required margin or slab tearing without which observed slab structure in the mantle could not be explained. For margin tearing to occur through viscous necking, we inferred from our experiments that the effective

strength, as denoted by $\tau_{max,}$ should be significantly smaller (τ_{max} = 50-300 MPa) than the strength of the slab (600-800 MPa), which allowed for tear propagation along the African margin. We note that our modeling of slab tearing/detachment is less elaborate than in Duretz et al. [2011, 2013] who implemented Peierls creep as the plasticity mechanism and could model both necking and shearing effects for lithosphere tearing. In addition, they incorporated compositional buoyancy forcing particularly of oceanic and continental crust. Our slab tearing occurred almost always quite shallow as we have prescribed the rheological weakness in the continental margin. The exception was model S2.1-4 (Figure 4.13; section 4.5.2).

The viscosity of the upper mantle depends on activation parameters for diffusion and dislocation creep (eq. 4.5). We have tested different values for these parameters to find an optimum for each reconstruction scenario. Rheological settings and values that led to the best-fitting slab evolution belong to the third group of experiments for tectonic scenario S1 (Table 4.2). For the other tectonic evolution models we attempted to optimize the fit between predicted and observed mantle structure by tuning mantle and margin rheology, but "best" values cannot be taken as useful as these models fail in producing a proper prediction of the mantle structure.

4.6.4 Role of the weakness zone at the eastern edge of the oceanic domain

The early phase of subduction in which rollback to the African margin started may depend on our implementation of the transition/weakness zone to the oceanic domain in the east, as well as on the fact that we did not model the subduction evolution of the eastern domain that ended up to form the detached Kabylides slab, and the Apennines-Calabria subduction system [e.g. Faccenna et al., 2004; Spakman and Wortel, 2004; van Hinsbergen et al., 2014]. Our simplification of this boundary causes a larger degree of freedom and higher flow speeds to develop and thus the modeled speed of initial subduction rollback may be higher than in reality.

To assess the influence of the eastern subduction boundary, we included (part of the) subduction of the eastern domain by constructing an initial condition that incorporates subduction of the Kabylides slab. To this end we extended the starting configuration of scenario S1 with a triangular zone of oceanic lithosphere east of the dashed weakness zone in Figure 4.5-S1b. The tip of this

triangular zone is at the Baleares margin while it is ~400 km wide along the east Algerian margin (see Figure 4.2-Scenario 1). Each long side of triangular zone constitutes a lithospheric weakness zone as in Figure 4.5-S1b.
Using the same rheological settings as for model S1.3-2 (Table 4.2; Figure 4.11), the slab evolution of this 2-slabs model, S1.4-7, is portrayed in Figure 4.22. The spatial evolution of the RGB-slab in the presence of the Kabylides slab is similar to that in model S1.3-2 (Figure 4.11), while the Kabylides slab evolves separately. At 10 Ma, the RGB-slab is located almost in the present day position, however, in comparison to the S1.3-2 model (Figure 4.11) it is located ~50 km to the east.

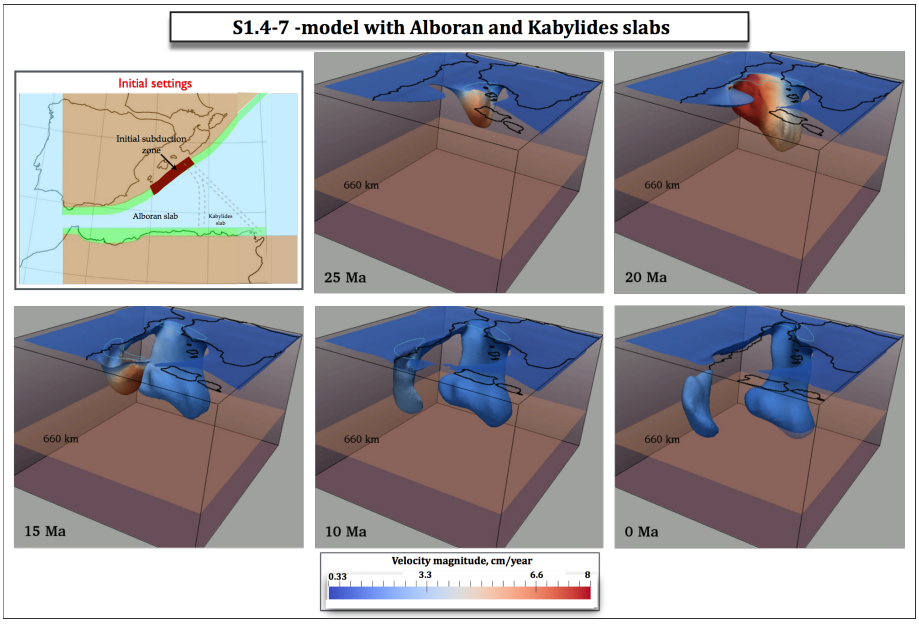

Figure 4.22. Model S1.4-7 that includes the evolution of the Kabylides slab. View from the NE.

The predicted location of the Kabylides slab matches its (blurred) tomographic image (Figure 4.3). Some important differences occur in the temporal evolution. First, the initial phase of stationary subduction of the RGB slab is now longer and takes around 8-10 My until 27-25 Ma. The RGB slab rolls back to the African margin where lithosphere tearing develops between 20 and 15 Ma. Around 15 Ma the Kabylides slab has also reached the African margin and detaches during the past 10 My. The addition of the Kabylides segment considerably improves the overall temporal evolution of

slab rollback leading to a good match with the emplacement of the Kabylides on the African margin in the Mid Miocene [Faccenna et al., 2004; Michard et al., 2006; van Hinsbergen et al., 2014].

4.7 Conclusions

We set out to test, by 3-D numerical modeling, the dynamic subduction evolution of the western Mediterranean since ~35 Ma as perceived, or portrayed, in three disparate tectonic reconstruction scenarios. From each scenario we determined an initial buoyancy condition, at 35 Ma, in terms of initial subduction zone configuration from which the 3-D slab evolution evolves dynamically and self-consistently. We experimented extensively with varying the nonlinear rheology of mantle, slab, and continental margins, and by varying initial slab configurations. For each scenario, we attempted to optimize the fit between predicted slab morphology after 35 My of model evolution and that observed with seismic tomography. This leads to the following conclusions:

1) A positive match between predicted and observed slab morphology was obtained for the subduction model of tectonic scenario S1 in which initial NW-directed subduction is restricted to the Baleares margin. For scenario S2, in which initial N-NW directed subduction from Gibraltar to the Baleares is proposed, we could not find a subduction model that reasonably fits present-day observations of mantle structure. Although scenario S3 that starts from initial S-SE-directed subduction under the north-African margin may successfully explain the slab structure in the top few hundred kilometers of the mantle, it leads to a slab extending far below the African continent, which is inconsistent with tomographic constraints.

2) We conclude from many experiments that the subduction evolution as portrayed for scenario S1 can be numerically simulated to produce an end-stage slab morphology close to that observed while satisfying the temporal constraints that the slab rolled back to the north African margin in the Middle Miocene (15 Ma) and was almost in its current position in the Tortonian (10-8 Ma). The robustness of the S1-slab evolution is demonstrated by several experiments varying the settings of model S1.3-2 that is based on a strong (800 MPa) and thickened south-Iberian margin (Figure 4.11). In particular, model S1.4-6 (Figure 4.21) shows that a thickened margin with an overall strength of 300 MPa leads to slow slab tearing since the Tortonian. In model

S1.4-7 (Figure 4.22) we included subduction of the Kabylides slab in the east and demonstrated a significant improvement of the temporal evolution constrained by rollback having reached the north-African margin by the Middle Miocene.

3) The following ranges in rheological parameters characterize our successful models: Slab strength is between 600 – 800 MPa for slab age > 100 Ma; African continental margin strength varies between 50-200 MPa for STEP-tearing; the south Iberian margin was thickened prior to the Miocene by 30km due to Africa-Iberia contraction and its margin strength is larger than ~300 MPa; an appropriate range for γ is 0.3-0.6 independent of the value of τ_{max}; activation volumes for diffusion and dislocation creep are 4-5 cm^3mol^{-1} and 8-9 cm^3mol^{-1} respectively. The old slab (>100 My) under these conditions is quite strong and cannot appreciably stretch during the subduction process.

4) The dynamic slab evolution of the successful numerical models of scenario S1 comprises the following first order geodynamic attributes that link to the tectonic/geological evolution of the region: a) Rollback to the African margin of the RGB- and Kabylides slabs (required for Kabylides emplacement). b) Westward tearing of the African margin, or slab, substantiating the explanation for the origin of, and westward trends in the geochemistry of margin volcanism. c) A more or less "in place" RGB-slab at ~8-10 Ma after which geological observations show no evidence for subsequent trench activity. d) A dominantly westward opening of the Algerian basin. e) A clockwise rotation of the RGB-slab of > 90° for the Gibraltar segment, and as a result of northward decreasing rollback rates amounts to >180° for the Betic segment, in accord with the dominant contractional direction as reconstructed for this region. f) A steep eastward dipping slab under the Gibraltar arc and a slab geometry curving from Gibraltar to the NE under the Betic region with a torn margin under the central-east Betic (model S1.4-6), as is observed with seismic tomography.

Our work constitutes a first step toward quantitative geodynamic underpinning of tectonic evolution scenario S1 and offers a viable subduction framework for further investigation of the geodynamic and geological evolution of the western Mediterranean. Our work demonstrates great potential of numerical simulation of geodynamic processes for constructing truly dynamics-based tectonic evolution models involving the deep driving processes of the mantle.

Appendix A.1

Here we show a model with a weak slab and continental margins attached to a strong continental lithosphere (Figure A1). The slab is partially attached to both continental plates via the weak margins; the main body of the slab is lying on a 660 boundary under the entire Alboran-Algerian basin and demonstrates a lot of holes due to stretching during the evolution of the subduction process. The resulting slab for this model does not correlate with tomography images (Figure 3) of the mantle structure of westernmost Mediterranean.

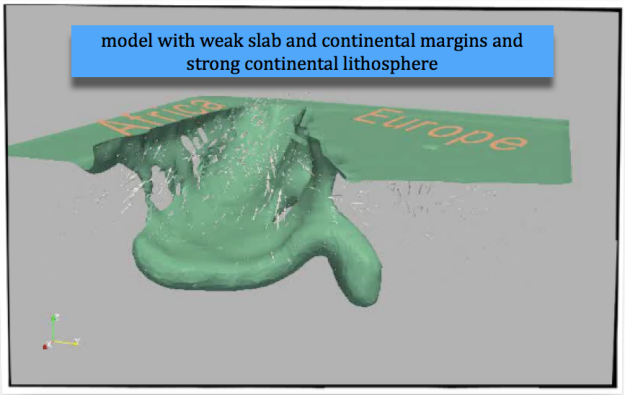

Figure A1. Model from first group of experiments S1.1 with weak oceanic lithosphere and continental margins and strong continental lithosphere. NE view.

Appendix A.2

The evolution of a model with a strong slab, weak African and Iberian margins and very weak mantle demonstrates a complete detachment of the slab after 15 My (Figure A2; the total evolution time for this model was set to 30 My). In this experiment the mantle is so weak that after rotation of the trench in a westward direction the slab steepens very fast and inflow of hot and highly mobile asthenosphere stimulates early slab detachment far east of the Gibraltar Strait and followed by fast slab sinking.

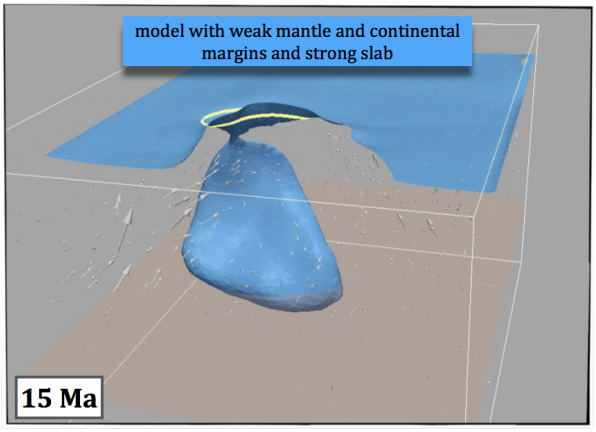

Figure A2. Model from group S1.1 with very weak mantle, strong slab and weak continental margins. NE view.

Appendix A.3

For this experiment we decrease the strength of the continental lithosphere. By prescribing $\tau_{max} = 200\ MPa$ we make it too weak to resist astenospheric flow and the continental lithosphere finally becomes part of the subduction process (Figure A3).

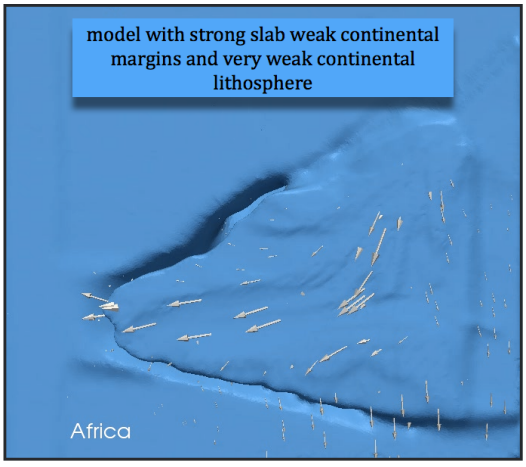

Figure A2. Model from group S1.1 with very weak continental lithosphere. Top view.

Appendix A.4

To demonstrate the independence of the modeled evolution of the subduction process in the westernmost Mediterranean on the domain size when using open side boundaries we perform the following test (Figure A4). The lateral

dimensions of the domain are increased to 2000×1600 km. The reference, S1.3-2 model and model S1.4-3 from this test develops similarly, after 35 My of the evolution only small differences observed for the deep part of the slab. Trenches coincide with each other. This shows that the adopted small domain dimensions do not significantly influence our subduction modeling of the western Mediterranean.

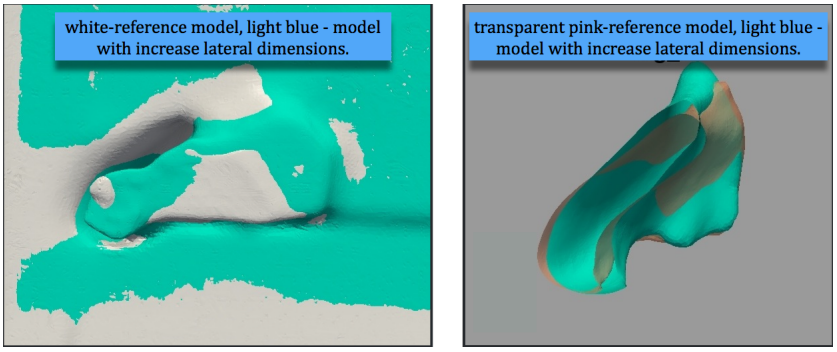

Figure A4. Difference between models S1.3-2 and S1.4-3 (model with increased lateral dimensions) after 35 My of the evolution. Top view. On the left - 1400 isotherms indicate similarity between top parts of the models. On the right – slab shape at 200 km and deeper for S1.3-2 (orange) and S1.4-3(turquoise-green).

Reference

1. Alisic, L., M. Gurnis, G. Stadler, C. Burstedde, and O. Ghattas (2012), Multi-scale dynamics and rheology of mantle flow with plates, J. Geophys. Res., 117, B10402, doi:10.1029/2012JB009234.
2. Alpert, L.A., M.S. Miller, T.W. Becker, and A. Allam (2013), Structure beneath the Alboran from geodynamic flow models and seismic anisotropy. J. Geophys. Res., 118. DOI:10.1002/jgrb.50309.
3. Amaru, M.L. (2007), Global travel time tomography with 3D reference models, PhD thesis, Utrecht University, Utrecht, the Netherlands.
4. Andrews, E.R., and M.I. Billen (2009), Rheologic controls on the dynamics of slab detachment, Tectonophysics, 464, 60-69, doi:10.1016/j.tecto.2007.09.004.
5. Becker, T. W., C. Faccenna, R. J. O'Connell, and D. Giardini (1999), The development of slabs in the upper mantle: Insights from numerical and laboratory experiments, J. Geophys. Res., 104(B7), 15207–15226, doi:10.1029/1999JB900140.

6. Bezada M.J., and E.D. Humphreys (2012), Contrasting rupture processes during the April 11, 2010 deep-focus earthquake beneath Granada, Spain, Earth and Planetary Science Letters, 353–354, 38-46, doi: 10.1016/j.epsl.2012.08.001.
7. Bijwaard, H., W. Spakman, and E.R. Engdahl (1998), Closing the gap between regional and global travel time tomography. Journal of Geophysical Research, 103, 30, 055-78, doi: 0.1029/98JB02467.
8. Billi, A., C. Faccenna, O. Bellier, L. Minelli, G. Neri, C. Piromallo, D. Presti, D. Scrocca, and E. Serpelloni (2011), Recent tectonic reorganization of the Nubia-Eurasia convergent boundary heading for the closure of the western Mediterranean. Bulletin de la Société Géologique de France, 182, 279-303.
9. Burov, E.B. (2011), Rheology and strength of the lithosphere, Marine and Petroleum Geology, 28 (8), pp. 1402-144
10. Calvert, A., E. Sandvol, D, Seber, M. Barazangi S. Roecker, T. Mourabit, F. Vidal, G. Alguacil, and N. Jabour (2000), Geodynamic evolution of the lithosphere and upper mantle beneath the Alboran region of the western Mediterranean: constraints from travel time tomography, Journal of Geophysical Research, 105, B5, 10,871-10,898.
11. Capitanio, F. and A. Replumaz (2013), Subduction and slab breakoff controls on Asian Indentation tectonics and Himalayan Western Syntaxis formation, Geochem. Geophys. Geosyst., doi: 10.1002/ggge.20171
12. Carminati, E., M. Lustrino, and C. Doglioni (2012), Geodynamic evolution of the central and western Mediterranean: Tectonics vs. igneous petrology constraints, Tectonophysics, 579, 173-192, doi: 10.1016/j.tecto.2012.01.026
13. Chalouan, A., A. El Mrihi, K. El Kadiri, A. Bahmad, F. Salhi, and R. Hlila (2006), Mauretanian flysch nappe in the northwestern Rif Cordillera (Morocco): deformation chronology and evidence for a complex nappe emplacement, *in* Moratti, G., and Chalouan, A., eds., Tectonics of the Western Mediterranean and North Africa. Geological Society, London, Special Publications, 262, 161-175, doi: 10.1144/GSL.SP.2006.262.01.10.
14. Chertova, M., T. Geenen, A.P. van den Berg, and W. Spakman (2012), Using open sidewalls for modelling self-consistent lithosphere subduction dynamics, Solid Earth Discuss. 4, 707-744, doi: 10.5194/se-3-313-2012.
15. Cizkova, H., J. van Hunen, and A.P. van den Berg (2007), Stress distribution within subducting slabs and their deformation in the transition zone. Phys. Earth Planet. Int., 161, 202–214.

16. Čížková, H., J. van Hunen, A.P. van den Berg, and N.J. Vlaar (2002), The influence of rheological weakening and yield stress on the interaction of slabs with the 670-km discontinuity, Earth Planet. Sci. Lett., 199, 447-457, 2002
17. Čížková, H., A.P. van den Berg, W. Spakman, and C. Matyska (2012), The viscosity of Earth's lower mantle inferred from sinking speed of subducted lithosphere, Physics of the Earth and Planetary Interiors, 200–201, 56-62, doi: 10.1016/j.pepi.2012.02.010.
18. Coulon, C., M. Megartsi, S. Fourcade, R.C. Maury, H. Bellon, A. Louni-Hacini, J. Cotten, A. Coutelle, and D. Hermitte (2002), Post-collisional transition from calc-alkaline to alkaline volcanism during the Neogene in Oranie (Algeria): magmatic expression of a slab breakoff, Lithos, 62, 3–4, 87-110, doi: 10.1016/S0024-4937(02)00109-3.
19. Crespo-Blanc, A., and J. Campos (2001), Structure and kinematics of the South Iberian paleomargin and its relationship with the Flysch Trough units: extensional tectonics within the Gibraltar Arc fold-and-thrust belt (western Betics), Journal of Structural Geology, 23, 10, 1615-1630, doi: 10.1016/S0191-8141(01)00012-8.
20. Christensen, U.R. and D.A. Yuen (1984), The interaction of a subducting lithosphere slab with a chemical or phase boundary, Journal of Geophysical Research, 89, doi: 10.1029/0JGREA0000890000B6004389000001.
21. Dercourt J., L.P. Zonenshain, L.-E. Ricou, V.G. Kazmin, X. LE Pichon, A.L. Knipper, C. Grandjacquet, I.M. Sbortshikov, J. Geyssant, C. Lepvrier, D.H. Pechersky, J. Boulin, J.-C. Sibuet, L.A. Savostin, 0. Sorokhtin, M. WWestphal, M.L. Bazhenov, J.P. Lauer and B. Biju-Duval (1986), Geological evolution of the Tethys belt from the Atlantic to the Pamir since the Lias, Tectonophysics, 123, 241-315
22. Díaz, J., Gallart, J., 2014. Seismic anisotropy from the Variscan core of Iberia to the Western African Craton: New constrains on upper mantle flow at regional scales. Earth Planet. Sci. Lett., 394, 48-57.
23. Diaz, J., J. Gallart, A, Villaseñor, F. Mancilla, A. Pazos, D. Córdoba, J.A. Pulgar, P. Ibarra, and M. Harnafi (2010), Mantle dynamics beneath the Gibraltar Arc (western Mediterranean) from shear-wave splitting measurements on a dense seismic array. Geophys. Res. Lett., 37. doi:10.1029/2010GL044201.
24. Doubrovine, P. V., B. Steinberger, and T.H. Torsvik (2012), Absolute plate motions in a reference frame defined by moving hotspots in the Pacific,

Atlantic and Indian oceans. Journal of Geophysical Research, 117, B09101, doi: 10.1029/2011JB009072.

25. Duggen, S., K. Hoernle, P. van den Bogaard, and C. Harris (2004), Magmatic evolution of the Alboran region: The role of subduction in forming the western Mediterranean and causing the Messinian Salinity Crisis, Earth and Planetary Science Letters, 218, 91-108, doi: 10.1016/S0012-821X(03)00632-0.
26. Duggen, S., K. Hoernle, P. van den Bogaard, and D. Garbe-Schönberg (2005), Post-collisional transition from subduction-to intraplate-type magmatism in the westernmost Mediterranean: Evidence for continental-edge delamination of subcontinental lithosphere, Journal of Petrology, 46 (6), 1155-1201, doi: 10.1093/petrology/egi01.
27. Duretz, T., T.V. Gerya, and D.A. May, (2011), Numerical modeling of spontaneous slab breakoff and subsequent topographic response, Tectonophysics, 502, 44-256, doi: 10.1016/j.tecto.2010.05.024.
28. Duretz, T., and T.V. Gerya (2013), Slab detachment during continental collision: Influence of crustal rheology and interaction with lithospheric delamination, Tectonophysics, ISSN 0040-1951, doi: 10.1016/j.tecto.2012.12.024.
29. Faccenna, C.,T.W. Becker, F. Pio Lucente, L. Jolivet, and F. Rossetti (2001), History of subduction and back-arc extension in the Central Mediterranean. Geophysical Journal International, 145, 809–820, doi:10.1029/ 2007GL029629.
30. Faccenna C., F. Funiciello, D. Giardini, and F. Pio Lucente (2001), Episodic back-arc extension during restricted mantle convection in the Central Mediterranean, Earth and Planetary Science Letters, 187, 105-116, doi: 10.1016/S0012-821X(01)00280-1.
31. Faccenna C., C. Piromallo, A. Crespo-Blanc, L. Jolivet, and F. Rossetti (2004), Lateral slab deformation and the origin of the western Mediterranean arcs. Tectonics;23:TC1012. doi:10.1029/2002TC001488.
32. Frizon De Lamotte, D., P. Leturmy, Y. Missenard, and S. Khomsi, (2009), Mesozoic and Cenozoic vertical movements in the Atlas system (Algeria, Morocco, Tunisia): an overview. Tectonophysics, *475*, 9–28.
33. Funiciello, F., C. Faccenna, A. Heuret, S. Lallemand, E. Di Giuseppe, and T.W. Becker (2008)Trench migration, net rotation and slab–mantle couplingEarth and Planetary Science Letters, 271, 233–240

34. Garel, F., S. Goes, D.R. Davies, J.H. Davies, S.C. Kramer, and C.R. Wilson (2014), Interaction of subducted slabs with the mantle transition-zone: a regime diagram from 2-D thermo-mechanical models with a mobile trench and an overriding plate. Geochem. Geophys. Geosyst., doi:10.1002/2014GC005257
35. Gerya, T.V., D.A. Yuen, and W.V. Maresch (2004), Thermomechanical modelling of slab detachment, Earth and Planetary Science Letters, 226, 101-116, doi: 10.1016/j.epsl.2004.07.022.
36. Gueguen, E., C. Doglioni, and M. Fernandez (1998), On the post-25 Ma geodynamic evolution of the western Mediterranean, Tectonophysics, 298, 1–3, 259-269, doi: 10.1016/S0040-1951(98)00189-9.
37. Gutscher M.A., J. Malod, J.P. Rehault, I. Contrucci, F. Klingelhoefer, L. Mendes-Victor, and W. Spakman (2002), Evidence for active subduction beneath Gibraltar. Geology;30:1071-1074.
38. Gutscher, M.A., S. Dominguez, G.K. Westbrook, P. Le Roy, F. Rosas, J.C. Duarte, P. Terrinha, J.M. Miranda, D. Graindorge, A. Gailler, V. Sallares, and R. Bartolome (2012), The Gibraltar subduction: A decade of new geophysical data, Tectonophysics, 574–575, 72-91, doi: 10.1016/j.tecto.2012.08.038.
39. Koulali A., D. Quazar, A. Tahayt, R.W. King, P. Vernant, R.E. Reilinger, S. McClusky, T. Mourabit, J.M. Davila and N. Amraoui (2011), New GPS constraints on active deformation along the Africa-Iberia plate boundary, Earth and Planetary Science Letters, 308, 211-217, doi: 10.1016/j.epsl.2011.05.048.
40. Handy, M.R., S.M. Schmid, R. Bousquet, E. Kissling, and D. Bernoulli (2010), Reconciling plate-tectonic reconstructions of Alpine Tethys with the geological–geophysical record of spreading and subduction in the Alps, Earth-Science Reviews, 102, 3–4, 121-158, doi: 10.1016/j.earscirev.2010.06.002.
41. Iribarren, L., J. Vergés, J. Camurri, J. Fullea, and M. Fernandez (2007), The structure of the Atlantic-Mediterranean transition zone from the Alboran Sea to the Horseshoe Abyssal Plain (Iberia-Africa plate boundary): Marine Geology, v. 243, p. 97-119.
42. Ismail-Zadeh, A., S. Honda, and I. Tsepelev (2012). Linking mantle upwelling with the lithosphere decent and the Japan Sea evolution: A hypothesis. Scientific Reports, 3, art. no. 1137, doi:10.1038/srep01137.
43. Jolivet, L., and Faccenna, C. (2000). Mediterranean extension and the Africa-Eurasia collision. Tectonics 19: doi: 10.1029/2000TC900018. issn: 0278-

7407.

44. Jolivet, L., C. Faccenna, and C. Piromallo (2009), From mantle to crust: Stretching the Mediterranean, Earth and Planetary Science Letters, 285,1–2, Pages 198-209, doi: 10.1016/j.epsl.2009.06.017.
45. Jonge, M.R. de, M.J.R. Wortel, and W. Spakman (1994), Regional scale tectonic evolution and the seismic velocity structure of the lithosphere and upper mantle: the Mediterranean region. *J. Geoph. Res.*, 99, 12091-12108.
46. Karato, S., M. Riedel, and D.A. Yuen (2001), Rheological structure and deformation of subducted slabs in mantle transition zone: implications for mantle circulation and deep earthquakes, Phys. Earth Planet. Int., 127, 83-108.
47. Lallemand, S., Y. Font, H. Bijwaard, and H. Kao (2001), New insights on 3-D plates interaction near Taiwan from tomography and tectonic implications. Tectonophysics, 335, 229– 253.
48. Liu, L., and M. Gurnis (2008), Simultaneous inversion of mantle properties and initial conditions using an adjoint of mantle convection Journal of Geophysical Research B: Solid Earth, 113 (8), art. no. B08405, doi:10.1029/2008JB005594.
49. Lonergan, L., and N. White (1997), Origin of the Betic-Rif mountain belt, Tectonics, 16(3), 504–522, doi:10.1029/96TC03937.
50. Magni, V., J. van Hunen, F. Funiciello, and C. Faccenna (2012), Numerical models of slab migration in continental collision zones, Solid earth, 3, 293-306, doi:10.5194/se-3-293-2012
51. Mason, W.G., L. Moresi, P.G. Betts, and M.S. Miller (2010), Three-dimensional numerical models of the influence of a buoyant oceanic plateau on subduction zones, Tectonophysics, 483, 1–2, 71-79, doi: 10.1016/j.tecto.2009.08.021.
52. Mauffret, A., D. Frizon de Lamotte, S. Lallemant, C. Gorini, and A. Maillard (2004), E-W opening of the Algerian Basin (Western Mediterranean). Terra Nova 16(5), 257-264, DOI: 10.1111/j.1365-3121.2004.00559.x.
53. Melialdea, T., R. Vegas, L. Somoza, T. Vazquez, A. Maldonado, V. Diaz-del-Rio, A. Maestro, D. Cordoba, and M.C. Fernandez-Puga (2004), Structure and evolution of the ‘‘Olistostrome’’ complex of the Gibraltar Arc in the Gulf of Cadiz (eastern central Atlantic): Evidence from two long seismic cross-sections: Marine Geology, 209, 173-198.
54. OzBench, M., K. Regenauer-Lieb, D. Stegman, G. Morra, R. Farrington, A. Hale, D.A. May, J. Freeman, L. Bourgouin, H. Muhlhaus, and L. Moresi

(2008), A model comparison study of large-scale mantle-lithosphere dynamics driven by subduction. Phys. Earth Planet. Int., 171, 224–234.

55. Palomeras, I., S. Thurner, A. Levander, K. Liu, A. Villasenor, R. Carbonell, and M. Harnafi (2014), Finite-frequency Rayleigh wave tomography of the western Mediterranean: Mapping its lithospheric structure, Geochem. Geophys. Geosyst., 15, doi:10.1002/2013GC004861.
56. Piromallo, C., and A. Morelli (2003), *P* wave tomography of the mantle under the Alpine-Mediterranean area, J. Geophys. Res., 108, 2065, doi: 10.1029/2002JB001757, B2.
57. Rosenbaum, G., G.S. Lister, and C. Duboz (2002), Reconstruction of the tectonic evolution of the western Mediterranean since the Oligocene. *Journal of the Virtual Explorer*, *8*, 107–130.
58. Royden, L.H. (1993), Evolution of retreating subduction boundaries formed during continental collision. Tectonics 12, doi:10.1029/92TC02641.
59. Schellart, W. P., and L. Moresi (2013), A new driving mechanism for backarc extension and backarc shortening through slab sinking induced toroidal and poloidal mantle flow: Results from dynamic subduction models with an overriding plate, J. Geophys. Res. Solid Earth, 118, 3221–3248, doi:10.1002/jgrb.50173.
60. Schettino, A., and E. Turco (2006), Plate kinematics of the Western Mediterranean region during the Oligocene and Early Miocene. Geophysical Journal International, 166(3), 1398–1423. doi:10.1111/j.1365-246X.2006.02997.x
61. Spakman W., and M.J.R. Wortel (2004), A tomographic view on western Mediterranean geodynamics. In: Ziegler P., editor. The TRANSMED Atlas-The Mediterranean Region From Crust to Mantle. Berlin: Springer, pp. 31-52.
62. Spakman W., and R. Hall (2010), Surface deformation and slab-mantle interaction during Banda arc subduction rollback, Nature Geoscience, 3, 562-566, doi: 1038/ngeo917
63. Stegman, D. R., W. P. Schellart, and J. Freeman (2010), Competing influence of plate width and far-field boundary conditions on trench migration and morphology of subducted slabs in the upper mantle. Tectonophys., 483, 46–57.
64. Spasojević, S., L. Liu, and M. Gurnis (2009), Adjoint models of mantle convection with seismic, plate motion and stratigraphic constraints: North

America since the Late Cretaceous, *Geochem. Geophys. Geosyst., 10,* Q05W02, doi:10.1029/2008GC002345.

65. van Hunen, J. (2001), Shallow and buoyant lithospheric subduction: causes and implications from thermo-chemical numerical modeling, PhD thesis, Utrecht University, Utrecht
66. van Hunen, J., and M.B. Allen (2011), Continental collision and slab break-off: a comparison of 3-D numerical models with observations. Earth and Planetary Science Letters 302(1-2), 27-37,doi: 10.1016/j.epsl.2010.11.035
67. van Hinsbergen, D.J.J., R.L.M. Vissers, and W. Spakman (2014), Origin and consequences of western Mediterranean subduction, rollback, and slab segmentation, Tectonics
68. Vergés, J., and M. Fernàndez (2012), Tethys–Atlantic interaction along the Iberia–Africa plate boundary: The Betic–Rif orogenic system, Tectonophysics, 579, 144-172, doi:10.1016/j.tecto.2012.08.032.
69. Vernant P., A. Fadil, T. Mourabit, D. Quazar, A. Koulali, J.M. Davila, J. Garate, S. McClusky and R. Reilinger (2010), Geodetic constraints on active tectonics of the Western Mediterranean: Implications for the kinematics and dynamics of the Nubia-Eurasia plate boundary zone, Journal of Geodynamics, 49, 123-129, doi: 10.1016/j.jog.2009.10.007.
70. Vissers R.L.M., and P.Th. Meijer (2012), Iberian plate kinematics and Alpine collision in the Pyrenees, Earth-Science Reviews, 114, 1–2, 61-83, ISSN 0012-8252, doi:10.1016/j.earscirev.2012.05.001.
71. Vissers, R., D.J.J. van Hinsbergen, and P.T. Meijer (2013), Kinematics of Jurassic ultra-slow spreading in the Piemonte Ligurian ocean. *Earth and Planetary Science Letters*, *380*, 138–150. doi:10.1016/j.epsl.2013.08.033

Chapter 5

Absolute plate motions and regional subduction evolution [*]

Abstract

We investigate the influence of absolute plate motion on regional 3-D evolution of subduction using numerical thermo-mechanical modeling. Building on our previous work (Chertova et al. 2014), we explore the potential impact of four different absolute plate motion frames on subduction evolution in the western Mediterranean region during the last 35My. One frame is data-based and derived from the global moving hotspot reference frame (GMHRF) of Doubrovine et al. [2012] and three are invented frames: a motion frame in which the African plate motion is twice that in the GMHRF, and two frames in which either the African plate or the Iberian continent is assumed fixed to the mantle. The relative Africa-Iberia convergent is the same in all frames. All motion frames result in distinctly different 3-D subduction evolution showing a critical dependence of slab morphology evolution on absolute plate motion. We attribute this to slab dragging through the mantle forced by the absolute motion of the subducting plate, which causes additional viscous resistance affecting subduction evolution. We observed a strong correlation between increase in northward Africa motion and decrease in the speed of westward slab rollback along the African margin. We relate this to increased mantle resistance against slab dragging providing new insight into propagation and dynamics of subduction transform edge propagator (STEP) faults. Our results demonstrate a large sensitivity of 3-D slab evolution to the absolute motion of the subducting plate, which inversely suggests that detailed modeling of natural subduction may provide novel constraints on absolute plate motions.

[*] This chapter has been published as: Chertova, M.V., W. Spakman, T. Geenen, A. van den Berg, and D.J.J. van Hinsbergen (2014), Absolute plate motions and regional subduction evolution, Geochem. Geophys. Geosyst.

5.1 Introduction

The influence of global plate tectonics on the local style of subduction evolution may be prominent but is unexplored in subduction modeling [Billen, 2008; Gerya, 2010]. In recent studies [e.g. Heuret et al., 2007; OzBench et al., 2008; Funiciello et al., 2008; Stegman et al., 2010; Schellart and Moresi, 2013] the motions of subducting and overriding plates were investigated in more generic approaches using geometrically and rheologically simplified 2D, or 3D models implementing rectangular plate domains, straight trenches and trench perpendicular convergence. Many of these studies implemented a constant or linear rheology [e.g. Funiciello et al., 2008; Capitanio et al., 2010; Schellart and Moresi, 2013], and/or did not include the overriding plate [e.g. Funiciello et al. 2008; Stegman et al. 2010; OzBench et al. 2008]. The motions of the subducting and overriding plates were either restricted to trench-perpendicular direction [Heuret et al. 2007; Stegman et al., 2010; Duretz et al., 2011, Schellart and Moresi, 2013] or were left free in trench-perpendicular direction while subduction dynamics are driving plate motion [Funiciello et al., 2008; Schellart and Moresi, 2013; Capitanio et al., 2010; Garel et al. 2014; Magni et al. 2014]. It is generally observed that the motion of subducting and overriding plates and the viscous coupling between slab and mantle plays an important role in the evolution of regional subduction dynamics. By prescribing only stress boundary conditions on the subducting and overriding plates a strong influence of far-field forcing on regional slab evolution is also observed [Leng and Gurnis 2011; Chertova et al. 2012]. Depending on the far-field forces imposed this led to either slab rollback, stationary subduction, or subduction with an advancing trench relative to the mantle, all for the same initial configuration of the subducting lithosphere and overriding plate.

Because of the simplified plate geometries used in 3-D or the restriction to 2-D subduction modeling, the application of these studies to understanding natural subduction evolution mostly concerns the central parts of laterally extensive and relatively straight subduction zones. Natural subduction, however, usually involves oblique plate convergence along curved plate boundaries. Recent investigations have highlighted that along-trench lithosphere heterogeneity has an important effect on subduction evolution [Duretz et al. 2014; Magni et al. 2014; Chertova et al. 2014]. In addition, the regional motion of the two plates involved in a subduction process is also

coupled to the global interaction between tectonic plates and underlying mantle [e.g. Warners-Ruckstuhl et al. 2012].

Here, we make a next step contributing to the understanding of the interaction between regional subduction evolution and global plate tectonics by incorporating such first order complexities. In particular, we investigate the effect of different plate motions on subduction evolution for which we use the natural geodynamic setting of western Mediterranean subduction of the last 35 My [Chertova et al. 2014]. This comprises oblique plate-convergence of the African (Nubia) and Eurasian (Iberian) plates involving strongly curved plate boundaries with laterally varying rheology. Within this oblique convergent setting the subduction trench rotated by >180° from plate-boundary parallel, to plate-boundary perpendicular, to again plate boundary parallel leading to the present-day Rif-Gibraltar-Betic slab [Rosenbaum et al., 2002; Spakman and Wortel 2004; van Hinsbergen et al., 2014; Chertova et al. 2014].

In Chertova et al. [2014], hereafter called Chert14, we modeled various subduction evolution scenarios for the region with a focus on optimizing the rheology of slab and mantle while the oblique plate convergent setting of subduction was the same in all experiments. Here, we adopt the preferred subduction scenario from Chert14 and focus on varying the absolute motions of the two major plates involved to investigate their effect on subduction evolution.

Absolute plate motions are the ideal kinematic boundary conditions for incorporating far-field forcing into regional modeling of *natural* subduction. These are the motions of lithosphere plates relative to the underlying mantle as defined in a mantle reference frame [e.g. Torsvik et al. 2008; van der Meer et al., 2010; Doubrovine et al. 2012]. Absolute plate motions result from all forcing of plate motion and are therefore consistent with the far-field forcing of global plate tectonics and global plate-mantle interaction, and are as well consistent with the regional forcing of subduction, e.g. slab buoyancy and local slab-mantle coupling. So far, absolute plate motion models are determined from a global collection of data and assumptions that unavoidably lead to uncertainty in their estimation [e.g. Doubrovine et al. 2012]. At best an estimate of the local plate motion can be obtained that results from the global interaction of plates and underlying mantle, i.e. representing far-field forcing.

In Chert14, the influence of far field forcing was represented by means of kinematic side-boundary conditions for continental northern Africa and Iberia,

determined from the global moving hot spot reference frame (GMHRF) of Doubrovine et al. [2012]. Here, we examine the effect of using three other absolute plate motion frames on the subduction evolution in the western Mediterranean region from 35 Ma until present. We use the relative motions between Iberia and Africa as detailed in van Hinsbergen et al. [2014] to implicitly define the following frames that implements (1) the motion of African plate defined by the GMHRF used for our reference model; (2) the African plate fixed to the deep mantle; (3) the Iberian continent fixed to the deep mantle; (4) the motion of the African plate taken two-times that of the GMHRF. Apart from the reference motion frame determined from Doubrovine et al. [2012], the three other are invented frames. The second and third motion frames were inspired by the observation that so far all tectonic and numerical studies of the regional tectonic evolution utilize a relative plate motion frame defined either relative to the African plate or to European plate [e.g. Rosenbaum et al. 2002, Handy et al. 2010; Jimenez-Munt and Negredo 2003, Perouse et al. 2011, Cunha et al. 2012]. The fourth motion frame we use is motivated by the fact that large uncertainty exists in estimated absolute plate motions [Doubrovine et al. 2012].

5.2 Model description

In Chert14, we investigated subduction evolution of the western Mediterranean region since ~ 35 Ma by varying initial conditions, initial subduction configurations, and by varying rheological settings of diffusion, dislocation creep, and yield stress of the lithosphere and the continental margins, and of the slab and ambient mantle. Here, we adopt the particular initial conditions and the rheological settings that were determined for the subduction evolution that successfully predicts first-order features of present-day slab morphology in the upper mantle. This model is used here as the reference subduction model and is introduced in section 5.2.3. In section 5.2.1 and 5.2.2, we will first briefly review our 3-D modeling approach and the initial model set up and conditions. We refer to Chert14 for the analysis that has led to determining these model conditions and features. Here, we experiment with varying the kinematic boundary conditions for the African and Iberian lithosphere, which are described in detail in section 5.2.2.

5.2.1 Initial numerical setup

We perform our experiments in 3-D space using the finite element package SEPRAN. The equations of mass, momentum and energy conservation and the transport equation for advection of non-diffusive material properties are solved in the extended Boussinesq approximation [Christensen and Yuen, 1984; van Hunen, 2001; Chert14]. Our models include two major phase transitions at 410 km and at 660 km in the unperturbed mantle [Cizkova et al. 2007; Chertova et al., 2012; Garel et al. 2014]. For the detailed description of these equations we refer to Christensen and Yuen [1984]. We use the same 3-D model setup as in Chert14, illustrated here in Figure 5.1a. The size of the modeling domain is 1650×1300×1000 km. On the vertical sides, we use open boundary conditions, which have much less influence on the flow in the modeling domain than the more common free-slip boundary conditions [Chertova et al., 2012, Chert14]. For the top boundary we use free-slip conditions and no-slip for the bottom boundary. To allow slab decoupling from the top surface and from the overriding plate, a crustal layer with a viscosity of 9×10^{19} Pa s and with a thickness of 30 km is initially placed on the top of the subducted slab. We implement kinematic boundary conditions for the top 150 km of the southern and northern side boundaries. These boundary conditions are used to prescribe various absolute motions of the African (Nubian) and Eurasian (Iberian) plates in our experiments (section 5.2.2).

Composite rheology is implemented in our models, which combines temperature and pressure dependent diffusion creep and dislocation creep, with a third term limiting the viscosity by prescribing the maximum yield stress. Used parameters for diffusion, dislocation creep and for yield stress values used here were determined in our previous work [Chert14]. Lagrangian particles are used for implementing the maximum yield stress separately for the oceanic and continental lithosphere, and for the continental margins. These particles are also used to define the weak crustal layer on the top of the subducted plate.

5.2.2 Initial model configuration and kinematic boundary conditions

We briefly summarize the initial continent-ocean configuration corresponding to the paleogeography at ~35 Ma and the particular constraints on rheology.

These were determined from an analysis of many subduction models in which the rheological strength of lithosphere, margins, and mantle were tuning parameters in modeling subduction evolution of the region [Chert14]. Figure 5.1a shows the configuration of five different lithosphere domains: two continental domains, Africa and Iberia, shown in brown, a continuous domain of oceanic lithosphere shown in blue, and two narrow zones corresponding to the continental margins. A yield strength of 800 MPa is used for the oceanic and continental lithosphere. A weak African margin is implemented with a yield strength of 100 MPa, while the European margin is as strong as the oceanic subducted lithosphere (800 MPa). The European margin was gradually thickened from 0 to 30 km from Gibraltar to western Baleares. This results in a lowered geotherm and consequently in a stronger margin rheology through the temperature control on rheology.

The initial temperature distribution for the 100 My oceanic lithosphere is computed from the equation of a cooling of semi-infinite half space [Turcotte and Schubert, 2002]. For the continental lithosphere we use a constant temperature gradient of 10 K/km to a depth of 150 km and for the sublithospheric mantle a constant temperature gradient of 0.3 K/km is taken similar to other studies [e.g. Ghazian and Buiter 2013]. The different geotherms in the oceanic and continental lithosphere (being cooler and thicker) lead to a more negatively buoyant continental lithosphere but also to a stronger rheology for the continental lithosphere. The double dashed line in Figure 5.1a indicates a weak lithosphere-decoupling zone which separates the future Rif-Gibraltar-Betic slab in the west from the subduction that developed to the east of this zone [Spakman and Wortel, 2004; Chert14].

The weak lithosphere-decoupling zone was given a width of 70 km and was made rheological weak by filling it with young (20 Ma) oceanic lithosphere. The initial subduction zone at ~35 Ma is shown in dark red in Figure 5.1a and is located SE from the Baleares. The initial length of the slab is ~200 km measured from the surface with a dip of ~40°. A maximum strength of 300 MPa was prescribed for the oceanic lithosphere in the Atlantic region to accommodate the relative NW-SE convergence between the African and Eurasian plates. In the numerical models this effectively results in focusing plate boundary deformation to a ~150 km wide zone that occurs to the west of Gibraltar.

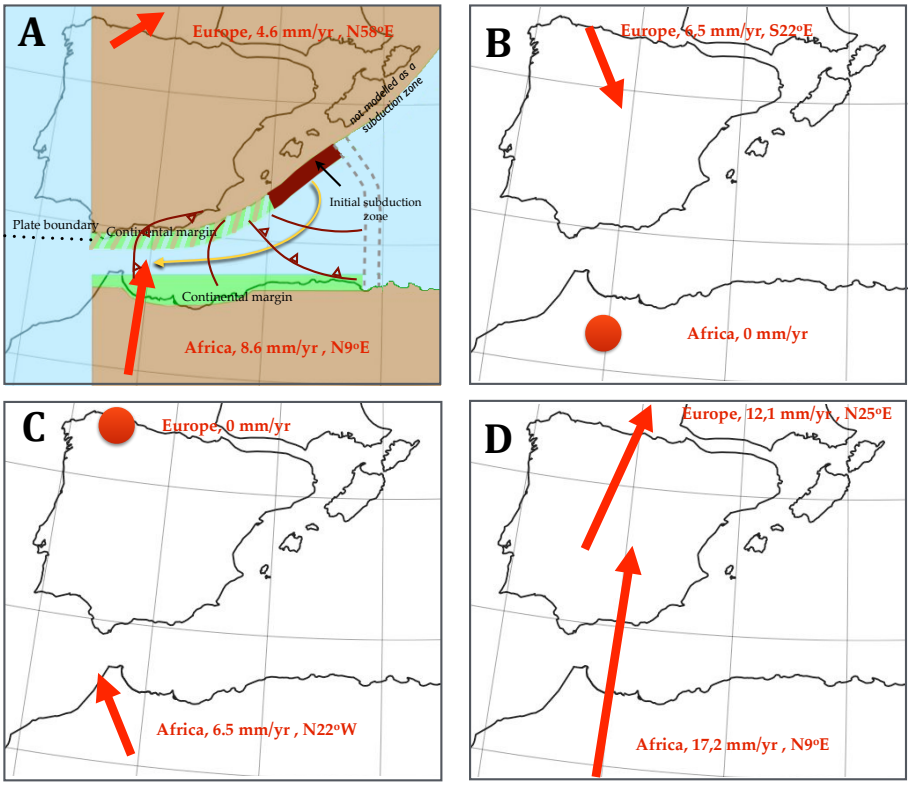

Figure 5.1. A: Initial subdivision of the model domain in continental lithosphere (brown), oceanic lithosphere (blue) and continental margins (green and green dashed). The thick dark red line indicates the initial subduction zone (see text for details) Trench positions through time are depicted with barbed lines while the yellow arrow indicates the direction of the slab rollback. The four panels show the absolute plate motion vectors (red arrows) for Africa and Iberia for four models A) 35My-average based on Doubrovine et al. [2012]; B) Iberia fixed to the mantle; C) Africa fixed (dot) to the mantle; D) 2 times faster Africa motion than in A while the absolute motion of Iberia is constrained by the relative motion between the two plates as in model B.

Figures 5.1a-d depict the applied kinematic boundary conditions for the four different absolute plate motion models used in our experiments. Figure 5.1a shows the average absolute plate motions for the last ~35 Ma as used in Chert14, based on the GMHRF of Doubrovine et al. [2012] with Africa moving N9°E with 8.6 mm/yr and Europe moving N58°E with 4.6 mm/yr.

The two plate motion vectors are consistent with the average relative motion between Iberia and Africa using the intra-African and intra-Iberian deformation-corrected plate circuit as detailed in van Hinsbergen et al. [2014]. The second absolute plate motion frame fixes the African plate to the mantle and thus requires the Iberian continent to move in the direction S22°E at a speed of with 6.5 mm/yr (Figure 5.1b). The third absolute plate motion frame with Iberia fixed to the mantle requires Africa moving in N22°W direction at 6.5 mm/yr (Figure 5.1c). Finally, we defined a two-times-faster velocity for Africa than predicted by the average values of the GMHRF, i.e. 17.2 mm/yr in N9°E, and an absolute Iberian motion of 12.1 mm/yr to N25°E to keep the relative Africa-Iberia velocity the same as in the other models (Figure 5.1d).
The last three frames are not intended to simulate real absolute plate motions but rather define variants of absolute plate motion frames that incorporate *the same* relative Africa-Iberia convergent motion vector averaged over the last 35 My. Therefore, modeled slab evolution is sensitive to changes in the global plate motion frame rather than to changes in the local relative plate motion. Note that the difference between any two of the motion models can be described by just one uniform Euler rotation defining a different interaction between the evolving subduction system and the ambient mantle.

5.2.3 Reference subduction model

The initial and boundary conditions (Figure 5.1a; section 5.2.2) constrain a subduction evolution model of the Rif-Gibraltar-Betic slab starting at 35 Ma, which is shown in Figure 5.2 and in Supplementary Materials 5.1 as a 3-D movie. This will be our reference subduction model, which is called model S1.3-2 in Chert14 and successfully predicts the tomographically observed slab morphology [Spakman and Wortel, 2004; Bezada et al., 2013; Chert14].
The initial configuration of Figure 5.1a corresponds to the paleo-geographic situation at ~35 Ma in which initial subduction is confined to the Baleares margin [e.g., Lonergan and White, 1997; Rosenbaum et al., 2002; Spakman and Wortel, 2004; van Hinsbergen et al., 2014]. The initial slab buoyancy is small and during the first 5 My subduction develops slowly at the Baleares trench, which is stationary relative to Iberia, leading to a slab length increase of only ~30 km. From ~30 Ma onwards, the trench rotates to a southwestward direction and fast rollback develops over the next 5 My. When the trench reaches the African margin, its western portion has rotated into a ~N-S strike.

This western segment subsequently rolls back westward, accommodated by lithosphere tearing along the African margin. After 23-25 My, the slab reaches the Gibraltar region and only slow trench retreat in northwestward direction is observed until the present. In the predicted present-day slab morphology, the slab edge is located under the Rif (Northern Morocco), extends northward to Iberia and curves to the NE under the south Iberian Betic range towards the Baleares. The deeper part of the slab is located under the Alboran Sea and southern Iberia. These are the first-order features that are in a good agreement with imaged slab morphology.

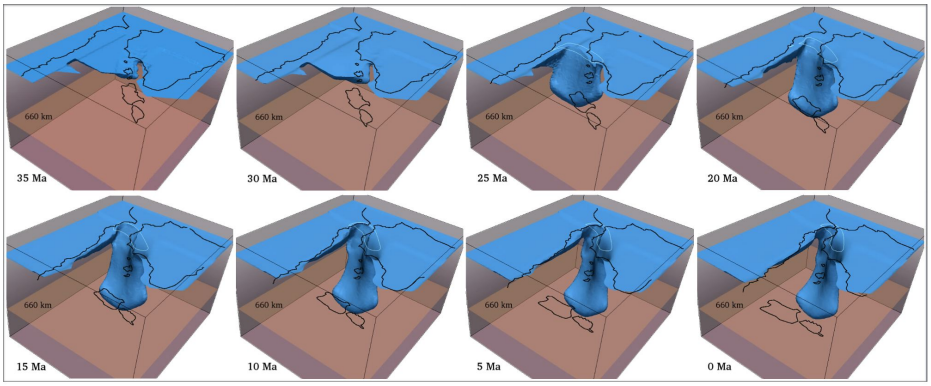

Figure 5.2. Evolution of the reference model in 5My steps and viewed from the northeast. The 1400 K isotherm is shown. Blue contour shows the surface projection of the slab outline at a depth 200km. The reference model is model S1.3-2 of Chert14.

5.3 Testing different absolute plate motion frames for modeling 3-D slab evolution of the western Mediterranean region

In all modeling experiments the initial configuration and rheological settings described above are maintained, while we impose three different kinematic boundary conditions (Figures 5.1b-d) on the top 150 km of the southern and northern sidewalls. As a result, the only differences between the model experiments are the imposed absolute plate velocities of Africa and Iberia, dragging the subduction system differently through the mantle, while the relative plate motion remains the same.

5.3.1 Africa fixed to the mantle and Iberia moving SSE

The absolute plate motion constraints for this model are given in Figure 5.1b. Figure 5.3 shows the evolution of Africa-fixed model (green) in comparison with the reference model (blue). Here we portray a top view, which better reveals the differences between these two models and shows the effect of an Africa-fixed frame on slab evolution. To make this comparison, the position of the slab for the Africa-fixed model in Figure 5.3 is shifted by lining up the African coastline with that of the reference model (in which the African plate is moving north; Figure 5.1a). Similar model shifts are done for the Iberia-fixed (Figure 5.4) and two-times faster Africa models (Figure 5.5). A movie illustrating slab evolution in which Africa is fixed, as in the numerical model, using a viewpoint in the NE is presented in Supplementary Materials 5.2.

Differences between models start to develop after the trench reaches the African margin and westward lithosphere tearing develops. Tearing propagates faster than in the reference model. The slab reaches the Gibraltar Strait already at ~16 Ma, which is ~6 My earlier than for the reference slab. Next, the slab starts to rotate clockwise and shows slight rollback toward the south Iberian margin without further westward retreat and without further lithosphere tearing. At shallow levels, the present-day morphology of the slab is comparable to that of the reference slab, although it is located more to the north in the Rif-Gibraltar region (Figure 5.3).

Deeper in the upper mantle the slab starts to differ more and is located farther to the north. This results from slab being overridden by the Iberian continent in a SSE direction during the slab stalling phase since ~16 Ma (Supplementary Movie 5.2). This is also the cause of a slightly more rotated trench and slab. Although differences in the final slab morphology between this model and the reference model are relatively small, the temporal development of the subduction process, which may link to a particular geological/tectonic surface response, is significantly different for these two models.

5.3.2 Iberia fixed to the mantle and Africa moving NNW

The plate motion constraints for this model are given in Figure 5.1c. The slab evolution is shown in Figure 5.4 (green slab) together with the evolution of the reference subduction model. A movie illustrating the evolution of this model with Iberia fixed to the mantle, as in the numerical model, is given in Supplementary Material 5.3.

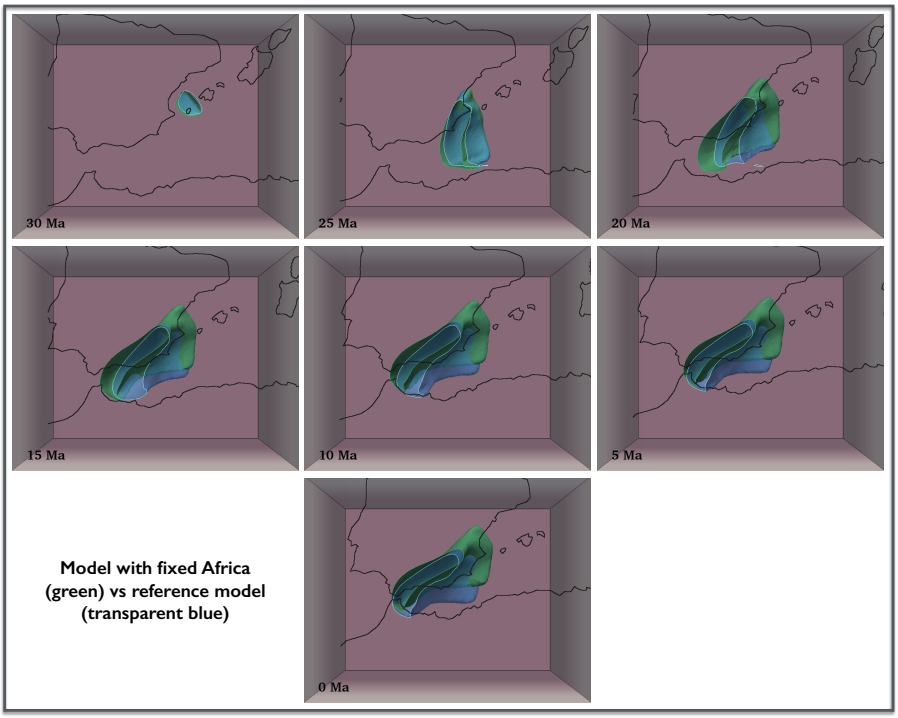

Figure 5.3. Slab evolution in the reference model (blue) and model in the Africa-fixed model (green). The slab contour is shown from the depth of 200 km downward indicated with blue and green line contours, partly looking inside the (hollow) slab contour. The bottom of the slabs reaches 660 km. The initial 35Ma slab morphology is skipped, as then the slab is shallower than 200 km. The coastlines are shown in absolute plate motion frame of the reference model (Figure 5.1a). The slab of the Africa-fixed model has been shifted such that the Africa coastline in both models coincides. The Supplementary movie 5.2 shows the 3-D evolution in which the African plate is fixed to the mantle (as in the numerical model).

The initial phase of stationary subduction is similar for both models. During initial southward rollback between 30-25 Ma the slab in the Iberia-fixed model assumes already a slightly more northerly position. After the trench reaches the African margin at ~25 Ma, lithosphere tearing along the African margin develops slower than in the Africa-fixed model but still faster than in the reference model. At ~14 Ma, 2 Ma after the Africa-fixed model and 4 My before the reference model, the slab reaches the Gibraltar region while

lithosphere tearing under Africa and slab rollback continue. In contrast to both the Africa-fixed model and the reference model, the trench retreats more and more to the northwest under the Iberian plate and eventually also a part of the continental lithospheric mantle becomes involved in subduction as a result of its negative buoyancy and despite its larger strength as compared to the subducting slab. The NW-directed slab retreat is a clear effect of the prescribed kinematic boundary (absolute motion) conditions of the Iberia-fixed frame.

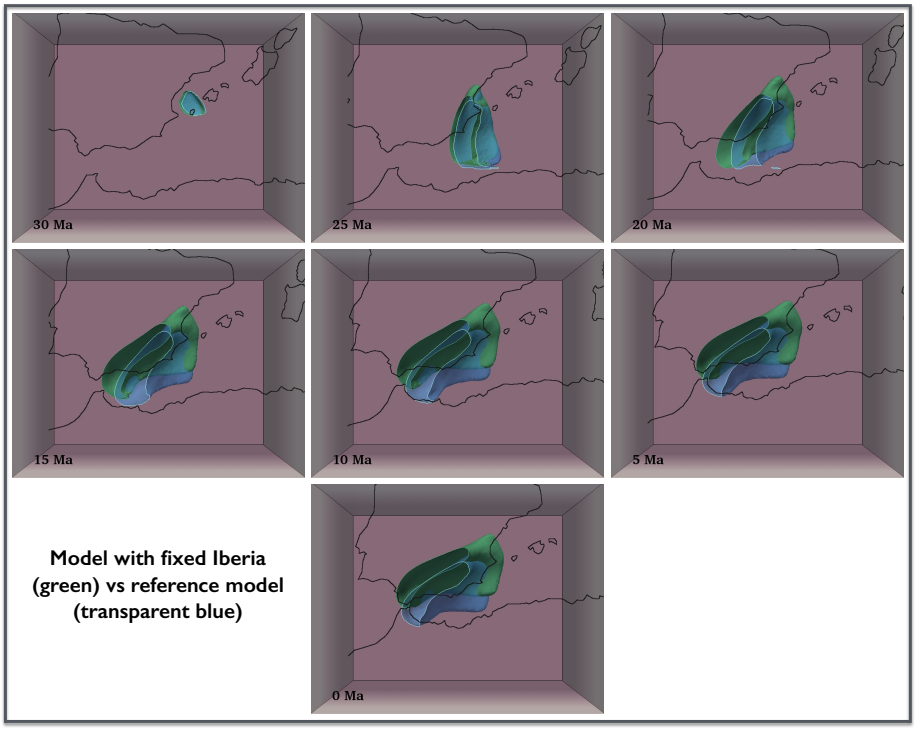

Figure 5.4. Slab evolution in the reference model (blue) and in the Iberia-fixed model (green). The slab contour is shown from the depth of 200 km downward. The initial, 35Ma slab morphology is skipped, as the slab is shallower than 200 km. The coastlines are shown in absolute plate motion frame of the reference model (Figure5. 1a; also see caption of Figure 5.3). The Supplementary movie 5.3 shows the 3-D slab evolution with Iberia fixed to the mantle (as in the numerical model).

During its evolution the slab is connected to both the African and Iberian plates. In the reference model the slab is dragged by Africa and Iberia towards

N-NE (Figure 5.1a) while in the Iberia-fixed model the slab is pushed under Iberia by the African plate advancing to the NW (Figure 5.1c). This African plate push is visible in the Supplementary movie 2 from ~15 Ma onward.
The final slab morphology of the Iberia-fixed model shows a significant difference with the reference model slab. The slab is located much more to the north at all depths from 100 to 660 km and the trench is rotated more clockwise than for the reference model. Relative to the African coastline, the more northwestern position owing to advancing Africa is accommodated by tearing along the African margin, which also propagates further to the west and to the north, even where no lithosphere weakening was prescribed, as compared to the reference model.

5.3.3 Model with two-times faster Africa motion

Next, we test the plate motion model as depicted in Figure 5.1d. The evolution of this model in comparison with the reference model is shown in Figure 5.5. Until 25 Ma the subduction process in these models develops similarly. Next, in the reference model fast westward rollback and lithosphere tearing along the African margin develops. However, in the model with larger absolute plate motion velocities, lithosphere tearing develops much slower. Since arrival of the slab at the African margin at 25 Ma only about 100 km of westward margin tearing occurs due to steepening of the slab. As a consequence, slab rollback is very slow. The final slab position is clearly different from the previous models, as the slab stalls with a N-S strike and is in a position far east of Gibraltar stretching from the SE Betics to Africa.

5.3.4 Trench-normal lithosphere tearing during trench-parallel absolute plate motion

The experiments described above demonstrate significant differences in subduction evolution depending on the adopted absolute plate motions. We infer three phases of subduction rollback: 1) the initial phase of slow roll back between 30-25 Ma which shows comparable slab behavior in all 4 models; 2) an intermediate rollback phase which culminates into margin/slab tearing and westward rollback at different speeds along the African margin; and 3) the final phase that starts when the slab has arrived in the Gibraltar region (in three models) and in which the slab is being deformed, rotated and dragged

NW or NE depending on the absolute motion of the two plates to which the slab is still attached.

A most conspicuous observation we can make for phase 2 is that westward slab tearing and slab rollback seems dependent on the northward absolute plate velocity of the African plate. In Figure 5.6 a comparison between the 4 models is shown for a snapshot at 20 Ma. The models are arranged such that from left to right the absolute motion of Africa is increasing. The Africa-fixed model (left) shows the fastest rollback arriving earliest at the Gibraltar Strait. The rollback of the slab is parallel to the margin and there is no significant north component of rollback i.e. margin/slab rupture occurs in response to shear stresses oriented predominantly vertically and parallel to the margin.

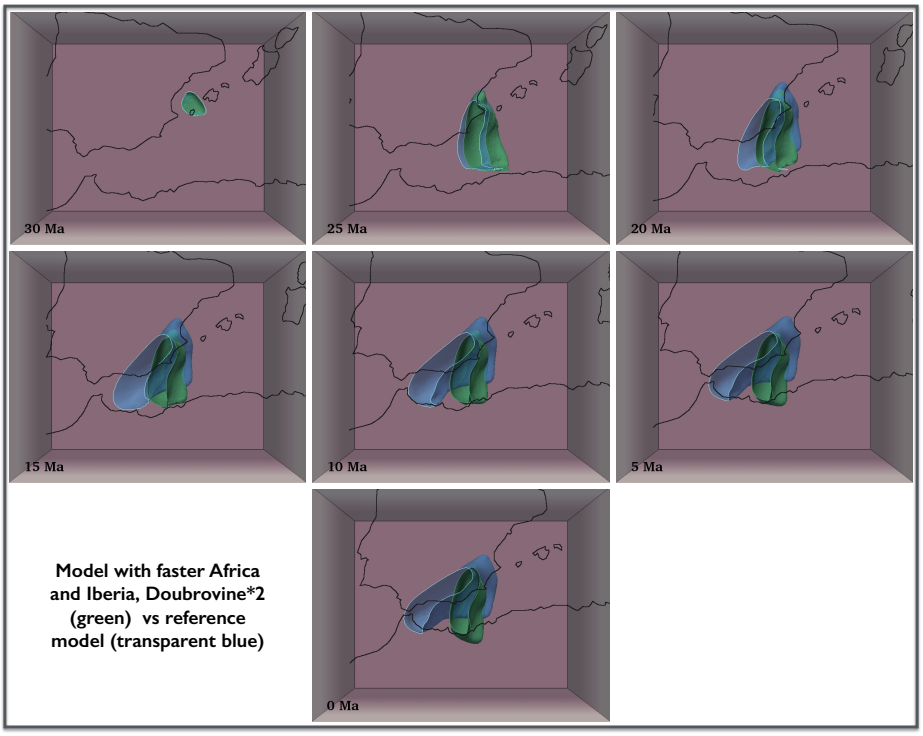

Figure 5.5. Subduction evolution in the reference model (blue) and in the model with two times faster Africa (green). The slab contour is shown from the depth of 200 km downward. The initial, 35Ma slab morphology is skipped as slab is shallower than 200 km. The coastlines are shown in absolute plate motion frame of the reference model (Figure 5.1A; also see caption of Figure 5.3).

The Iberia-fixed model (middle) has a northward component of African motion of ~6 mm/yr in which the tear propagates slower than in the Africa-fixed model. In both models, tearing and rollback are faster than in the reference model, which has a northward African motion of nearly 8.6 mm/yr. In the right panel of Figure 5.6, the African plate is moving north at ~17.2 mm/yr and tearing and rollback prove to be strongly inhibited from the moment the trench has rotated perpendicular to the advancing African margin. The differences between these models are primarily caused by the different absolute plate motion frames, as the relative motion between Africa and Iberia is the same in all experiments (Figure 5.1). The subducting plate is attached to both moving continents and as a result the slab is dragged through the mantle, which is visible in all models (Figures 5.4-6, 5.9; Supplementary Movies). Slab dragging is governed by absolute plate motion and leads to increase of mantle resistance against slab motion in case of absolute motion increase.

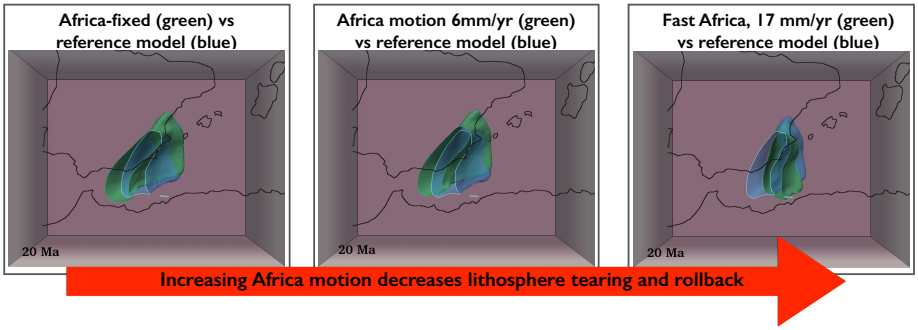

Figure 5.6. Slab morphology in the four subduction models at 20 Ma. The reference model is shown in blue in all panels and belongs to a northward Africa motion of 8 mm/yr. The first figure shows the Africa-fixed model; the second the Iberia-fixed model; the third figure shows the model with two-times faster Africa. The 1400K isotherm is shown from 200km downward. The coastlines are shown in absolute plate motion frame of the reference model (Figure 5.1a; Doubrovine et al. 2012).

We suggest that the decrease in tearing and rollback speed along the African margin is caused by the combination of resistive viscous flow of mantle material being pushed away by the slab-edge in the north and by increasing lateral slab-mantle shear friction forced by northward African plate-push. These couplings exist in addition to the viscous coupling between slab and mantle related to slab rollback as observed in analogue and numerical

experiments based on trench-perpendicular plate motions [e.g. Funiciello et al., 2006; Schellart and Moresi, 2013; Capitanio and Replumaz, 2013].

Figure 5.7 illustrates the coupling between plates, slab, and mantle in a N-S cross-section through the fast moving Africa model, showing in colors the N-component of the velocity field for two plates, mantle and the slab. The largest northward velocities are observed for the African plate. For the Iberian plate the northward component of plate motion is smallest. For the slab these values are intermediate and the slab, while sinking, is being pushed by the African plate and experiences viscous resistance from the upper mantle. This can also be seen from the wide area of large northward velocities in the mantle near the slab edge. For this model, indicated by the difference in northward speed, the African plate is overriding the slab, which prevents extension of the continental margin. This keeps the African margin thick and suppresses further lithosphere tearing.

After the slab has rolled back to the African margin and the trench and slab reoriented nearly perpendicular to that margin, the geometry becomes favorable for the development of a STEP fault [Govers and Wortel, 2005]. This slab geometry, however, is also almost parallel to absolute Africa motion and thus maximizes lateral mantle shear resistance resulting from slab dragging, increasing N-S compression at the margin.

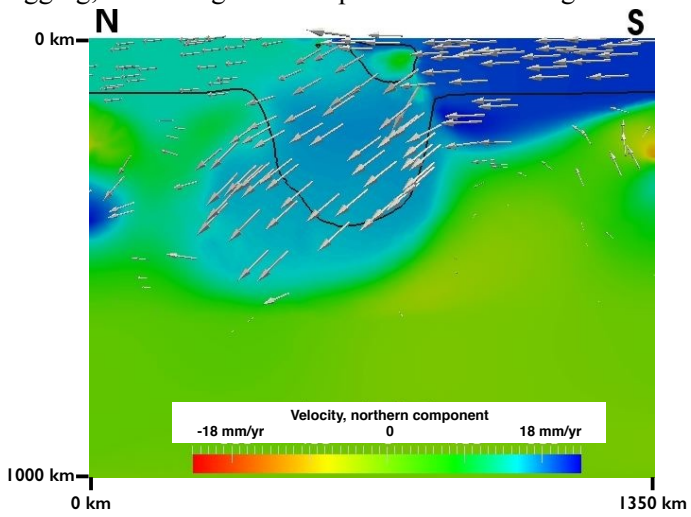

Figure 5.7. The NS cross-section of the model with fast Africa after 15My of subduction evolution. The northward component of the velocity is shown in colors. Arrows indicate the direction and magnitude of the total velocity field. Black contour shows the 1400°-isotherm.

Although the relative convergence between Iberia and Africa is the same in all experiments, the absolute motion of Iberian lithosphere may also be of influence on the inferred dependence of westward slab rollback on African plate motion. The subducting basin is connected to both continents and Africa-Iberia convergence (Figure 5.1) may put this margin continuously under compression.

To investigate this further we perform a few additional experiments with a simplified geometry of two westward propagating STEPS in which the northern plate ("Iberia") is now free to move (Figure 5.8a). The slab has a rectangular shape with a width of 700 km. The initial depth reached by the slab is 200 km and the dip angle is 45°. The southern continental plate ("Africa") is moving in northward direction with a constant velocity. The northern plate also has a rectangular shape and is free to move, as the northern boundary in these experiments is now completely open. Continental plates and the subducting oceanic slab have maximum strength of 800 MPa as in previous experiments. We did not prescribe a weakness zone between the oceanic plate and the northern continent. Instead we assume a thinned continental plate with a thickness of 60 km. Due to the pressure-dependence of the non-linear rheology, this results in a weaker asthenosphere decreasing shear resistance at the base of the lithosphere. The margin between the southern continent and the oceanic domain has a maximum strength of 100 MPa as in our previous models.

Models were run under different absolute northward motions for the southern boundary, ranging from 8 mm/yr to 30 mm/yr. Our experiments show a similar dependence of westward rollback rates and associated lithosphere tearing on increasing absolute plate motion parallel to the slab as was observed in Figure 5.6. An example is given in Figure 5.8b. However, now this dependence is observed for a free "Iberian" plate, moving with a slightly lower northward velocity than "Africa". The slowdown of tearing speed can now be *completely* attributed to the increasing northward motion of "Africa".

The maximum speed we have tested is 30mm/yr, which already leads to a strong reduction in tearing rate (Figure 5.8b). Within the plate-motion range investigated, we do not observe the stage when tearing and rollback stalls. The northern plate could in all experiments assume a motion similar to the southern plate. We therefore conclude that the relative Iberia-Africa convergence used in our earlier experiments also has a strongly restricting

effect on westward STEP propagation along the North African margin. Figure 5.9 schematically summarizes our findings of the influence of mantle resistance due to forced slab motion perpendicular to the rollback direction on the evolution of a STEP, lithosphere tearing and rollback.

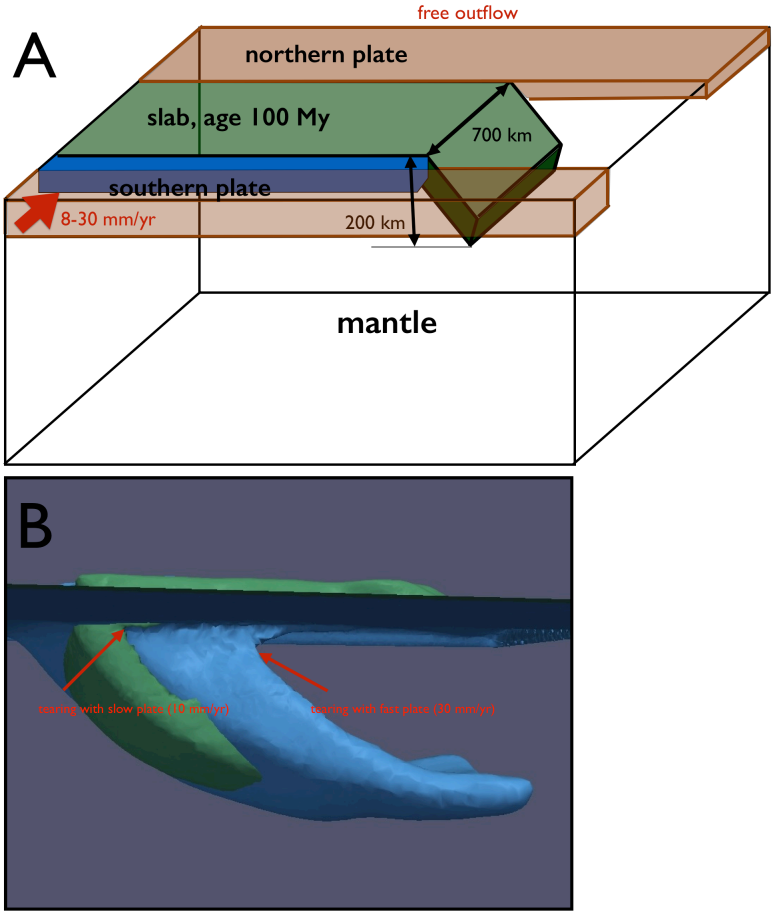

Figure 5.8. a: Initial configuration of a subduction model with two STEPS. The slab is shown in green, continental lithosphere is shown in brown. Note the different thickness of the southern and northern continental plates (150 and 60 km respectively). Red arrow shows the north-directed motion of the southern plate. In blue the weak continental margin is depicted. Initial slab depth is 200 km and slab dip 45°. b: The slab shape after 12 My of subduction and STEP evolution for 10mm/yr (green) and 30 mm/yr (blue) motion of the southern plate.

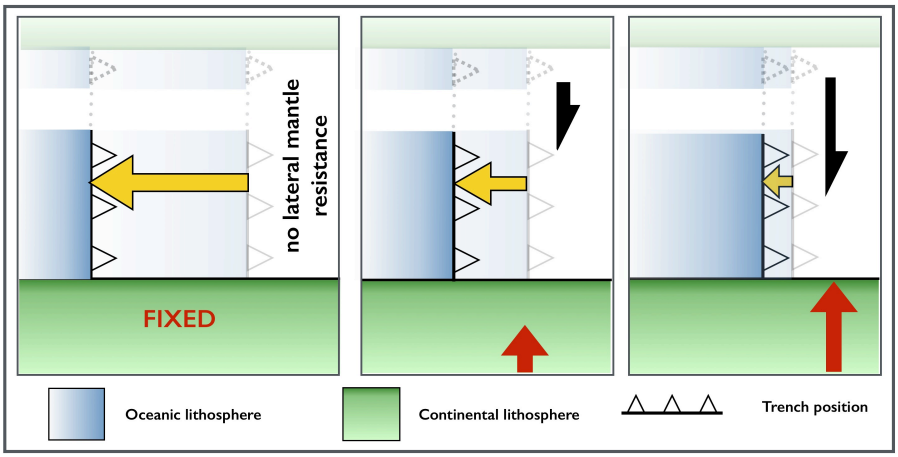

Figure 5.9. Schematic representation of our results on the dependency of the speed of rollback (yellow vector) and the associated STEP on the absolute motion of the overriding plate (red vector) parallel to the slab. The black vector denotes the overall mantle resistance resulting from slab push by the advancing continent which comprises slab-lateral mantle shear as well as resistance to mantle flow in front of the pushed slab.

5.4 Discussion

We can relate the strong differences in subduction evolution directly to the particular regional absolute plate motion frame used in each experiment. In each absolute plate motion frame the subduction system is dragged differently through the mantle. The resulting resistance defines a particular viscous coupling between slab and mantle that significantly affects subduction evolution and the present-day slab position and morphology. The forced coupling between slab and mantle may prove of wider importance for understanding slab dynamics in relation to tectonic/surface evolution. Although these differences with the reference model in slab position and morphology are relatively small on the scale of the overall slab evolution model, they are systematic. Such differences may impact quite differently when trying to couple the slab's dynamic evolution to the detailed makeup of crust and lithosphere structure, and the tectonic evolution of the Betic-Alboran-Rif region.

A similar setting of rollback at high angles to absolute plate motion exists for the Banda Arc subduction (southeast Asia) where mantle shear resistance

against Banda slab motion provides an explanation for the enigmatic strongly folded slab morphology and for the tectonic evolution of the overlying crust [Spakman and Hall, 2010]. Another example is the "slab-edge-push" of van Benthem et al. [2014], which is a slab-edge effect of slab motion forced by absolute plate motion.

Here we varied absolute plate motions and adopted those rheological settings that belong to the slab evolution model (the reference model) that provided a good prediction with observed slab morphology. Investigation of trade-offs between faster/slower Africa motion and weaker/stronger rheology of the mantle is necessary for making a closer connection with the particular tectonic evolution of the region and to further constrain absolute plate motions. This is preferably done with models using a more detailed process-based rheology for lithosphere tearing and using a free surface [e.g. Duretz et al. 2011], as well as including the eastern subduction system of the Western Mediterranean region that led to subducted slab under the Apennines and Calabria [Spakman and Wortel, 2004; Faccenna et al. 2004; Rosenbaum et al., 2002].

Other STEP settings in a similar geometry with a subduction trench at high angles with an advancing continental plate are the Calabria slab interacting with the African plate in the Central Mediterranean [Spakman and Wortel, 2004; Govers and Wortel, 2005; Wortel et al. 2009], or the Lesser Antilles slab interacting with the South American plate [VanDecar et al. 2003; Govers and Wortel, 2005; van Benthem et al. 2013, Boschman et al., 2014]. For all these STEP settings the absolute plate motion of the advancing continent, forcing additional slab-mantle resistance, may prove crucial for STEP evolution in determining the dynamics of rollback as well as the dynamic evolution of the plate boundary.

5.5 Conclusions

We tested the effect of using four different absolute plate motion frames, one data-based and three invented, on the evolution of slab morphology which we investigated in the natural setting of subduction evolution in the western Mediterranean region since ~35 Ma. We inferred strong absolute plate motion effects on slab morphology, rollback evolution, and present-day slab position. Particularly, we showed that the rate of lithosphere tearing and rollback along a continental margin decreases with the increasing component of absolute velocity oriented normal to the rollback direction, i.e. oriented parallel to the

trench. This strongly affects the motion and dynamics of the STEP and the crustal evolution of the deforming plate boundary region, we predict.

We conclude that absolute plate motion of the subducting plate can have large influence on the regional evolution and dynamics of subduction by forcing slab dragging through the mantle that locally results in an additional viscous coupling between the subducting lithosphere and the ambient mantle. As this will also affect the mantle flow field surrounding the evolving slab this opens new research avenues for linking absolute plate motion to observations of seismic anisotropy through 3-D modeling of natural subduction evolution. In general, we conclude that detailed modeling of natural subduction systems may also provide novel constraints on absolute plate motions, such that they can help reducing the uncertainties in the current absolute plate motion models independent of the observations on which such models are based.

Our results demonstrate that regional absolute plate motion, which represents here the far-field global plate-tectonic forcing, is critical for a correct simulation of subduction evolution in natural laboratories. For the western Mediterranean region we showed that even relatively small changes in absolute plate motions on the order of a few mm/yr have significant effects on slab morphology evolution due to resistance against slab dragging.

As an outlook, we anticipate that the crustal evolution associated with subduction evolution involving slab drag by absolute plate motions will be distinctly different in different absolute plate motion settings as this may have large influence on the local dynamics of subduction through its coupling with the ambient mantle. Detecting such coupling may also lead to new perspectives on the interpretation of geological observations and may eventually lead to new diagnostics for linking surface deformation to deep processes in convergent plate-boundary regions.

References:

1. Bezada M.J., E.D. Humphreys, D.R. Toomey, M.Harnafi, J.M. Davila, and J. Gallart (2013), Evidence for slab rollback in westernmost Mediterranean from improved upper mantle imaging, Spain, Earth and Planetary Science Letters, 368, 51-60.
2. Billen, M.I. (2008), Modeling the dynamics of subducting slabs, Annual Review of Earth and Planetary Sciences, 36, pp. 325-356.

3. Boschman, L.M., van Hinsbergen, D.J.J.**,** Torsvik, T.H., Spakman, W., and Pindell, J.L., accepted pending revision, Kinematic reconstruction of the Caribbean region since the early Jurassic, *Earth-Science Review.*

4. Capitanio, F.A., D.R. Stegman, L.N. Moresi, and W. Sharples (2010), Upper plate controls on deep subduction, trench migrations and deformations at convergent margins, Tectonophysics, 483 (1-2), pp. 80-92.
5. Capitanio, F.A. and A. Replumaz (2013), Subduction and slab breakoff controls on Asian indentation tectonics and Himalayan western syntaxis formation, Geochem. Geophys. Geosyst., 14, 3515-3551
6. Chertova, M., T. Geenen, A.P. van den Berg, and W. Spakman (2012), Using open sidewalls for modelling self-consistent lithosphere subduction dynamics, Solid Earth 3, 313-326.
7. Chertova, M., W. Spakman, T. Geenen, A.P. van den Berg, and D.J.J. van Hinsbergen (2014), Underpinning tectonic reconstructions of the western Mediterranean region with dynamic slab evolution from 3-D numerical modeling, Journal of Geophysical Research, doi: 10.1002/2014JB011150
8. Christensen, U.R. and Yuen, D.A. (1984), The interaction of a subducting lithosphere slab with a chemical or phase boundary. Journal of Geophysical Research 89.
9. Cizkova, H., J. van Hunen, and A. van den Berg (2007), Stress distribution within subduction slabs and their deformation in the transition zone, Physics of Earth and Planetary Interiors, 161, 202-214, doi:10.1016/j.pepi.2007.02.002
10. Cunha, T.A., L.M. Matias, P. Terrinha, A.M. Negredo, F. Rosas, F. Fernandes, and L.M. Pinheiro (2012), Neotectonics of the SW Iberia margin, Gulf of Cadiz and Alboran Sea: a reassessment including recent structural, seismic and geodetic data, Geophys. J. Int., 188, 850-872, doi:10.1111/j.1365-246X.2011.05328.x
11. Doubrovine, P. V., B. Steinberger, and T.H. Torsvik (2012), Absolute plate motions in a reference frame defined by moving hotspots in the Pacific, Atlantic and Indian oceans. Journal of Geophysical Research, 117, B09101, doi: 10.1029/2011JB009072.
12. Duretz, T., T.V. Gerya, and D.A. May (2011), Numerical modelling of spontaneous slab breakoff and subsequent topographic response, Tectonophysics, 502 (1-2), pp. 244-256.
13. Duretz, T., T. Gerya, and W. Spakman (2014), Slab detachment in laterally

varying subduction zones: 3D numerical modeling. Geophys. Res. Lett., 41, 1951-1956.

14. Funiciello, F., M. Moroni, C. Piromallo, C. Faccenna, A. Cenedese, and H.A. Bui (2006), Mapping mantle flow during retreating subduction: Laboratory models analyzed by feature tracking, J. Geophys. Res., 111, B03402, doi:1029/2005JB003792.
15. Funiciello, F., C. Faccenna, A. Heuret, S. Lallemand, E. Di Giuseppe, and T.W. Becker (2008), Trench migration, net rotation, and slab-mantle coupling, Earth and Planetary Science Letters, 271, 233-240.
16. Garel, F., S. Goes, D.R. Davies, J.H. Davies, S.C. Kramer, and C.R. Wilson (2014), Interaction of subducted slabs with the mantle transition-zone: a regime diagram from 2-D thermo-mechanical models with a mobile trench and an overriding plate. Geochem. Geophys. Geosyst., doi:10.1002/2014GC005257
17. Gerya T. (2010), Future directions in subduction modeling, Journal of Geodynamics, doi:10.1016/j.jog.2011.06.005
18. Ghazian, R.K. and S. Buiter (2013), A numerical investigation of continental collision styles, Geophys. J. Int., 193, 1133-1152
19. Govers, R. and M.J.R. Wortel (2005), Lithosphere tearing at STEP faults: Response to edges of subduction zones, Earth and Planetary Science Letters, 236 (1-2), pp. 505-523.
20. Handy, M.R., S.M. Schmid, R. Bousquet, E. Kissling, and D. Bernoulli (2010), Reconciling plate-tectonic reconstructions of Alpine Tethys with the geological–geophysical record of spreading and subduction in the Alps, Earth-Science Reviews, 102, 3–4, 121-158, doi: 10.1016/j.earscirev.2010.06.002.
21. Heuret, A., F. Funiciello, C. Faccenna, and S. Lallemand (2007), Plate kinematics, slab shape and back-arc stress: A comparison between laboratory models and current subduction zones, Earth and Planetary Science Letters, 256, 473-483.
22. Jimenez-Munt, I. and A.M. Negredo (2003), Neotectonic modeling of the western part of the Africa-Eurasia plate boundary: from the Mid-Atlantic ridge to Algeria, Earth and Planetary Science Letters, 205, 257-271.
23. Leng, W. and M. Gurnis (2011), Dynamics of subduction initiation with different evolutionary pathways, Geochem. Geophys. Geosyst., 12, Q12012, doi:10.1029/2011GC003877

24. Lonergan, L., and N. White (1997), Origin of the Betic-Rif mountain belt, Tectonics, 16(3), 504–522, doi:10.1029/96TC03937.
25. Magni, V., C. Faccenna, J. van Hunen, and F. Funiciello (2014), How collision triggers backarc extension: Insight into Mediterranean style of extension from 3-d numerical models, Geology, 42 (6), 511-514.
26. OzBench, M., K. Regenauer-Lieb, D. Stegman, G. Morra, R. Farrington, A. Hale, D.A. May, J. Freeman, L. Bourgouin, H. Muhlhaus, and L. Moresi (2008), A model comparison study of large-scale mantle-lithosphere dynamics driven by subduction. Phys. Earth Planet. Int., 171, 224–234.
27. Perouse, E., P. Vernant, J. Chery, R. Reilinger, and S. McClusky (2011), Active surface deformation and sub-lithospheric processes in the western Mediterranean constrained by numerical models, Geology, 38, 823-826, doi:10.1130/G30963.1
28. Rosenbaum, G., G.S. Lister, and C. Duboz (2002), Reconstruction of the tectonic evolution of the western Mediterranean since the Oligocene. *Journal of the Virtual Explorer*, *8*, 107–130.
29. Schellart, W. P., and L. Moresi (2013), A new driving mechanism for backarc extension and backarc shortening through slab sinking induced toroidal and poloidal mantle flow: Results from dynamic subduction models with an overriding plate, J. Geophys. Res. Solid Earth, 118, 3221–3248, doi:10.1002/jgrb.50173.
30. Spakman W., and M.J.R. Wortel (2004), A tomographic view on western Mediterranean geodynamics. In: Ziegler P., editor. The TRANSMED Atlas-The Mediterranean Region From Crust to Mantle. Berlin: Springer, pp. 31-52.
31. Spakman W., and R. Hall (2010), Surface deformation and slab-mantle interaction during Banda arc subduction rollback, Nature Geoscience, 3, 562-566, doi: 1038/ngeo917
32. Stegman, D.R., W.P. Schellart, and J. Freeman (2010), Competing influences of plate width and far-field boundary conditions on trench migration and morphology of subducted slabs in the upper mantle, Tectonophysics, Volume 483, Issues 1–2, Pages 46-57, ISSN 0040-1951, doi: 10.1016/j.tecto.2009.08.026.
33. Torsvik, T. H., R. D. Müller, R. Van der Voo, B. Steinberger, and C. Gaina (2008), Global plate motion frames: Toward a unified model. Rev. Geophys., 46, RG3004, doi:10.1029/2007RG000227.
34. Turcotte, D.L., Schubert, G. (2002), Geodynamics, Cambridge University

Press.

35. Van Benthem S., R. Govers, W. Spakman, and R. Wortel (2013), Tectonic evolution and mantle structure of the Carribean, J. Geophys. Res., 118, 3019-3036.
36. Van Benthem, S., R. Govers, and R. Wortel (2014), What drives microplate motion and deformation in the northeastern Caribbean plate boundary region? Tectonics, 33, 850-873.
37. VanDecar, J.C., R.M. Russo, D.E. James, W.B. Ambeh, and M. Franke (2003), Aseismic continuation of the Lesser Antilles slab beneath continental South America, J. Geophys. Res., (Solid Earth) 108.
38. Van der Meer, D.G., W. Spakman, D.J.J. van Hinsbergen, M.L. Amaru, and T.H. Torsvik (2010), Towards absolute plate motions constrained by lower mantle slab remnants, Nature Geoscience, 3, 36-40.
39. van Hinsbergen, D.J.J., R.L.M. Vissers, and W. Spakman (2014), Origin and consequences of western Mediterranean subduction, rollback, and slab segmentation, *Tectonics,*. 33, 393-419
40. van Hunen, J. (2001), Shallow and buoyant lithospheric subduction: causes and implications from thermo-chemical numerical modeling. PhD thesis, Utrecht University, Utrecht.
41. Warners-Ruckstuhl, K.N., R. Govers, and R. Wortel (2012), Lithosphere-mantle coupling and the dynamics of the Eurasian Plate, Geophys. J. Int., 189 (3), 1253-1276.

Chapter 6

Summary and outlook

In this thesis my overall goal was to model the 3-D subduction evolution of the Rif-Gibraltar-Betic slab in the western Mediterranean region by means of 3D thermo-mechanical modeling. I have started this research with 2D numerical experiments of the evolution of the subduction process. This was discussed in the third chapter. The main research goals were: investigation of basic numerical and rheological settings, which allows for the development of a free rollback process and investigation of the influence on its evolution by side boundary conditions. The use of open side boundaries proved extremely important for reaching our overall goal with 3D numerical experiments. We have demonstrated that using open side boundary conditions we can significantly reduce lateral domain size while the flow pattern inside the modeling domain is largely unaffected. Furthermore a wide range of parameters for composite rheology was tested, which was later used for the 3D numerical modeling.

I continued my research with 3D experiments on the modeling of the evolution of the subduction process in western Mediterranean since 35Ma till present. Three distinctly different kinematic reconstructions were tested, which all claimed to reproduce the present day mantle structure as imaged by tomography studies. It was shown that these tectonic reconstructions after 35My of subduction evolution led to completely different slab position and shape and, as a result, different mantle structure. For obtaining the most successful model in terms of fitting present day mantle structure and timing of the evolution of the subduction process including a second small subduction system to the east proved key and resulted in predicting the observed cold anomaly in this region interpreted as the Kabylides slab. By including this Kabylides slab we managed to improve the fit with and geological/geochemical inferences of two major temporal constraints: slab arrival to the African margin in Middle Miocene and slab stalling under the Gibraltar region since the Tortonian.

On the basis of a successful model for the evolution of the western Mediterranean region, which only involves the Rif-Gibraltar-Betic slab, the

influence of different absolute plate motion reference frames on the dynamics of the subduction process was investigated. Three different absolute plate motion reference frames were developed on the basis of the relative Africa-Iberia convergence [van Hinsbergen et al., 2014] and by varying on the global plate motion model of Doubrovine et al., [2012] and tested against prescribed absolute plate motions based on Doubrovine et al. [2012] as used for our slab modeling in Chapter 4. The main conclusion was that for modeling of the evolution of complex *real-earth* subduction, on scales and style comparable to the western Mediterranean subduction, is crucial to constrain numerical models by absolute plate motions. In our case this was made possible by the development of open side boundaries.

In this thesis a large step was made from 2D and 3D generic modeling of the evolution of the subduction process toward real-earth numerical simulations, which aim to describe the subduction evolution of single or multiple slabs. Although this research combines a lot of advances of 3D numerical modeling including temperature dependency, composite rheology and active viscous necking process resulting in lithosphere tearing there are still plenty of parameters and settings which could be implemented or tested for the subduction modeling of the western Mediterranean region or any of Earth subduction zones.

Here we concentrated on the evolution of the western Mediterranean region, which includes two slabs: the RGB and Kabylides slabs. Extending this research with including modeling the eastern subduction system leading to slab under the Apennines and Calabria is a next step, would provide a quantitative assessment of the geodynamic evolution of the entire Western Mediterranean.

In this thesis we included only lithospheric plate motions on the sidewalls and do not account for actual mantle flow during slab evolution. This requires additional generic modeling on the investigation of influence of arbitrary mantle flow or temperature (chemical) mantle anomalies on the dynamics of the subducted slab, which has not been done before. Then this might be applied to the region of the interest by prescribing global mantle flow, e.g. obtained from back-advecting the present-day density distribution as inferred from seismic tomography, in terms of kinematic side boundary conditions, as was done for absolute plate motions in our models.

Another important avenue of investigation of the western Mediterranean is the present day upper mantle anisotropy, which is a result of past lithosphere and mantle motions and their interaction. The observations of the anisotropy are derived from S-wave propagation and SKS splitting direction for the RGB region, which were widely investigated (Bokelmann et al. 2011, Schmid et al. 2004). In recent studies, anisotropy around the subducted slab was calculated using the software D-Rex, Kaminski [2004], which was implemented and tested in 3D by Faccenda and Capitanio [2013], Capitanio and Faccenda [2012]. This code enables calculation of the mantle anisotropy and SKS splitting directions from past to present from our successful models of the evolution of western Mediterranean that can be compared to observations seismic anisotropy.

Another research challenge for real-Earth subduction evolution is predicting the evolution of overlying topography and how the evolving slab affects the topography of surrounding plates. Some generic studies model the surface response of the overriding plate to the sinking slab by using a free top surface (e.g. Duretz et al. 2012). Implementing this free surface to our models allows us to model and investigate topography evolution of the region, which might be important for better understanding the mechanisms, e.g. the dynamic role of the RGB slab, which cause the Messinian salinity crisis and its development in terms of stress and strain-rate fields and resulting topography changes in the region.

This leads us to the last challenging research question we can address when modeling the evolution of western Mediterranean region, particularly the evolution of the stress field from past to present. Predicting stress and strain-rate fields opens new links to geological observations. This will require more detailed implementation of absolute plate motions and model geometry than currently implemented in our models.

References

1. Bokelmann, G., E. Maufroy, L. Buontempo, J. Morales, G. Barruol (2011), Testing oceanic subduction and convective removal models for the Gibraltar arc: Seismological constraints from dispersion and anisotropy. Tectonophysics, 502, 28-37, doi: 10.1016/j.tecto.2010.08.004
2. Capitanio, F.A., M. Faccenda (2012), Complex mantle flow around

heterogeneous subducting oceanic plates, Earth and Planetary Science Letters, 353-354, 29-37, doi: 10.1016/j.epsl.2012.07.042

3. Doubrovine, P. V., B. Steinberger, and T.H. Torsvik (2012), Absolute plate motions in a reference frame defined by moving hotspots in the Pacific, Atlantic and Indian oceans. Journal of Geophysical Research, 117, B09101, doi: 10.1029/2011JB009072.
4. Duretz, T., T.V. Gerya, B.J.P. Kaus, and T.B. Andersen (2012), Thermomechanical modeling of slab eduction. J. Geophys. Res., vol. 177, B08411. doi:10.1029/2012JB009137
5. Faccenda, M., F.A. Capitanio (2013), Seismic anisotropy around subduction zones: Insights from three-dimensional modeling of upper mantle deformation and SKS splitting calculations. Geochemistry, Geophysics, Geosystems, 14 (1), 243-262.
6. Kaminski, E., N. M. Ribe and J. T. Browaeys (2004), D-Rex, a program for calculation of seismic anisotropy due to crystal lattice preferred orientation in the convective upper mantle. Geophys. J. Int., 158 - pp. 744-752, 2004.
7. Schmid, C., S. Van der Lee, and D. Giardini (2004), Delay times and shear wave splitting in the Mediterranean region. Geophys. J. Int. 159, 275–290.
8. van Hinsbergen, D.J.J., R.L.M. Vissers, and W. Spakman (2014), Origin and consequences of western Mediterranean subduction, rollback, and slab segmentation, Tectonics.

Samenvatting

Deze thesis heeft als hoofddoel het modelleren van de ontwikkeling van de subductie van de Rif-Gibraltar-Betische slab in het westen van het Middellandse Zeegebied door middel van 3D thermo-mechanische modellen. Ik ben echter begonnen met 2D numerieke experimenten van de evolutie van het subductie proces, zoals beschreven in Hoofdstuk 3. Met deze 2D modellen heb ik de numerieke en rheologische parameters onderzocht die het vrij terugrollen van de subducerende plaat mogelijk maken, alsmede het effect van verschillende verticale randvoorwaarden op dit proces. Het gebruik van open verticale randen blijkt erg belangrijk voor 3D modellen: we hebben laten zien dat hiermee de laterale domeingrootte sterk verminderd kan worden zonder dat het algemene stromingspatroon in de mantel veranderd.

Vervolgens heb ik de resultaten van het 2D onderzoek gebruikt voor 3D experimenten van de subductie evolutie in het westelijke Middellandse Zeegebied vanaf 35 Ma tot op heden. Hierbij heb ik drie verschillende kinematische reconstructies getest, welke allen claimen de huidige mantel structuur als gezien door tomografische studies te reproduceren. Het blijkt dat na 35 My van subductie de drie reconstructies tot compleet verschillende slab posities en geometrieën leidden, en dus tot een andere mantel structuur. Voor een optimale fit tussen onze modellen en de huidige mantel structuur en timing van subductie, heb ik een tweede, kleiner, subductie systeem toegevoegd in het oosten van het onderzoeksgebied. Mét dit systeem reproduceren we de koude anomalie die geïnterpreteerd wordt als de Kabylies slab en verbeteren we de overeenkomsten met, en de geologische en geochemische gevolgen van, twee belangrijke temporele voorwaarden: het bereiken van de Afrikaanse marge door de slab gedurende het Midden Mioceen en het vertragen van de slab onder de Gibraltar regio sinds het Tortoon.

Gebaseerd op een succesvol model van de ontwikkeling van het westelijke Middellandse Zeegebied met slechts de Rif-Gibraltar-Betische slab, hebben we het effect van verschillende absolute plaatbeweging referentie frames op de dynamiek van het subductie proces onderzocht. Hiervoor hebben we drie verschillende referentie frames ontwikkeld op basis van de convergentie tussen Afrika en het Iberische Schiereiland [van Hinsbergen et al., 2014] en variaties op het globale plaatbeweging model van Doubrovine et al. [2012].

Deze zijn vervolgens getest met behulp van de absolute plaatbewegingen afgeleid van Doubrovine et al. [2012], welke ook zijn gebruikt voor de modellen in Hoofdstuk 4. De belangrijkste conclusie is dat voor het modelleren van de evolutie van complexe *real-Earth* subductie, op schaal van en in stijl van de subductie in het Middellandse Zeegebied, cruciaal is om numerieke modellen te begrenzen met absolute plaatbewegingen. In het geval van deze thesis was dit mogelijk door de ontwikkeling van open verticale domeinranden.

Acknowledgements

Completion of the work presented in this thesis would not be possible without contribution of my colleagues, who I would like to mention here.
First, I would like to thank my promotor Wim Spakman for accepting my application for PhD position in his group – the starting point of this work! I really appreciate his guidance, especially in preparing my manuscripts and conference presentations. Wim has been always full of ideas, either in how to continue existing research or in proposing new challenging directions.
I would like to thank my co-promotor Arie van den Berg for giving useful advice on technical content of the thesis and for sharing his expertise in numerical modeling with me.
Thomas Geenen, who has been my daily supervisor for some time, has enormously contributed in the setting up of my research work. I would like to thank him for introducing me to the world of numerical modeling and in usage of SEPRAN code in particular.
Other senior member of our group, Douwe van Hinsbergen helped me during developing the initial geometrical settings of the 3D experiments and we have had fruitful scientific discussions.
This research would not be possible without technical support of Theo van Zessen. Thank you, Theo, for your fast reaction on any problems with "gaia" which saved for all of us many days for additional experiments.
I would also like to mention Shalaleh, Jellie and Anne, my room neighbors for creating nice atmosphere in our office.
Vladimir Suvorov, who was the supervisor of my Master thesis in Novosibirsk State University, requires special acknowledgement for inspiring me to continue my scientific career.
My parents, Olga and Vladimir, and my brother Sergey have been continuously supporting me. We had nice time together during their stays here in the Netherlands and during our joint trips to Belgium, Italy and France. I would like to also mention the family of my husband: his parents and his brother Dmitry for their constant support.
Finally, I would like to thank my husband, Alexey for all his love, care, and support during my PhD and for his agreement to stay with our dogs alone when I was going for conferences that, I know, was very hard for him.

Curriculum Vitae

23 September 1986	**born in Novosibirsk**
2001-2003	**Pre-university education** Specialized Educational Scientific Centre (SESC), NSU Novosibirsk, Russia
2003-2007	**Bachelor in geology** Novosibirsk State University (NSU) Novosibirsk, Russia
2007-2009	**Master in geophysics** Novosibirsk State University Novosibirsk, Russia
2009-2013	**PhD-candidate** Mantle dynamics group, Utrecht University Utrecht, the Netherlands
Since 2014	**post-doctoral researcher** Mantle dynamics group, Utrecht University Utrecht, the Netherlands